ISSN 2432-8375

BULLETIN OF THE

LABORATORY FOR ADVANCED NUCLEAR ENERGY

VOL. 2 2017

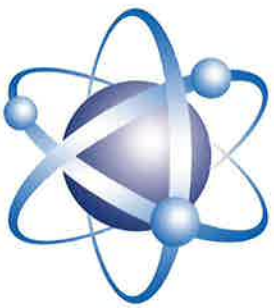

LANE

LABORATORY FOR ADVANCED NUCLEAR ENERGY
INSTITUTE OF INNOVATIVE RESEARCH
TOKYO INSTITUTE OF TECHNOLOGY

BULLETIN OF THE LABORATORY FOR ADVANCED NUCLEAR ENERGY

(Formerly, BULLETIN OF THE RESEARCH LABORATORY FOR NUCLEAR REACTORS)

Abbreviation of the "**BULLETIN OF THE LABORATORY FOR ADVANCED NUCLEAR ENERGY**" is BULL. LAB. ADV. NUCL. ENERGY

All communications should be addressed to the editor, Laboratory for Advanced Nuclear Energy, Institute of Innovative Research, Tokyo Institute of Technology (Tokyo Kogyo Daigaku),
2-12-1-N1-16, O-okayama, Meguro-ku, Tokyo 152-8550, Japan.

TEL. +81-3-5734-3052, FAX. +81-3-5734-2959, E-mail bulletin@lane.iir.titech.ac.jp

http://www.lane.iir.titech.ac.jp/

BULLETIN OF THE LABORATORY FOR ADVANCED NUCLEAR ENERGY
BULL. LAB. ADV. NUCL. ENERGY, Vol.2, 2017

CONTENTS

Research staffs of
THE LABORATORY FOR ADVANCED NUCLEAR ENERGY,
TOKYO INSTITUTE OF TECHONOGY
AS OF 2017 JAPANESE FISCAL YEAR

Director

Toyohiko YANO	Professor

Innovative Nuclear Energy System Division

Toru OBARA	Professor
Yukitaka KATO	Professor
Yoshinao KOBAYASHI	Professor
Minoru TAKAHASHI	Professor
Tatsuya KATABUCHI	Associate Professor
Hiroshige KIKURA	Associate Professor
Masatoshi KONDO	Assistant Professor
Jun NISHIYAMA	Assistant Professor

Actinide Management Division

Kenji TAKESHITA	Professor
Koichiro TAKAO	Associate Professor
Takehiko TSUKAHARA	Associate Professor

Global Nuclear Security Division

Toshihiko OHNUKI	Professor
Toyohiko YANO	Professor
Hiroshi SAGARA	Associate Professor
Katsumi YOSHIDA	Associate Professor
Tetsuo SAWADA	Assistant Professor
Anna GUBAREVICH	Assistant Professor

Advanced Medical Application Division

Yoshiyuki OGURI	Professor
Noriyosu HAYASHIZAKI	Associate Professor
Yoshihisa MATSUMOTO	Associate Professor
Jun HASEGAWA	Associate Professor
Mikio SHIMADA	Assistant Professor

Fundamental Research Division

Shunji IIO	Professor
Satoshi CHIBA	Professor
Hiroshi AKATSUKA	Associate Professor
Hiroaki TSUTSUI	Associate Professor
Chikako ISHIZUKA	Assistant Professor

Advanced Research and Education Program

Akira NISHIMURA	Specially Appointed Professor

Common Staffs

Kazutoshi FURUKAWA	Specially Appointed Professor
Hiroyasu MOCHIZUKI	Specially Appointed Professor
Hiroshi UETSUKA	Specially Appointed Professor
Satoru TSUSHIMA	Specially Appointed Associate Professor
Eiichi ASANO	Visiting Professor
Takatoshi TAKEMOTO	Visiting Associate Professor
Maletaskic JELENA	Specially Appointed Assistant Professor
Hideharu TAKAHASHI	Specially Appointed Assistant Professor

Technical Staffs

Hitoshi FUKUDA	Senior Technical Specialist
Masamitsu IMAI	Senior Technical Specialist
Mitsuo MATSUZAKI	Senior Technical Specialist
Atsushi NEZU	Senior Technical Specialist
Ken-ichi TOSAKA	Senior Technical Specialist

I. Special Articles in Commemoration of Retiring Professors

I.1 Neutron-Irradiation-Induced Crystalline Defects of Ceramics

Toyohiko YANO

1. Introduction

Nuclear power plants need various kinds of materials, including ceramics, to complete their mission such as electric power generation and high temperature heat supply. From nuclear fuels to high-level nuclear waste confinements, various kinds of ceramic materials are necessary components of fission nuclear fuel cycle. In fusion reactors, wide variety of ceramics will be required to sustain fusion nuclear fuel cycle. Many kinds of non-oxide ceramics are applied or required for nuclear energy components, such as silicon carbide for fuels of high-temperature gas-cooled reactors, SiC_f/SiC composites for blanket structure materials for fusion reactors and advanced fuel cladding for water-cooled fission reactors. Graphite is main structure components of high-temperature gas-cooled reactors, and B_4C is important neutron absorber materials for control rods. Other non-oxides such as AlN and Si_3N_4 or SiAlON are also expected to be applied for fusion reactors [1].

Inside nuclear reactors, materials are irradiated with high-energy neutrons, and then their properties will degrade because of the formation of irradiation-induced lattice defects. Therefore, it is very important not only to identify and characterize their crystalline defects but also to understand stability of induced defects.

In this report, advances on characterization of high-energy-neutron-induced crystalline defects into mainly non-oxide ceramics studied by our group are reviewed. Recovery behavior of ceramics is also mentioned shortly.

2. Radiation Damage of Advanced Ceramics

2.1. General feature

Due to accumulation of crystalline defects, such as Frenkel pairs (pair of vacancy and self interstitial atom), dislocation loops, voids and bubbles containing transmuted gaseous atoms, several properties of almost all ceramics are degraded beyond some doses, depending mainly irradiation temperature.

Table 1 and **2** are examples of property changes of typical advanced ceramics caused by severe fast neutron irradiation, corresponding to the fluence of core materials inside fast reactors for relatively long operation period [2]. Amount of linear swelling of Al_2O_3 and AlN ceramics are relatively bigger than these of SiC and Si_3N_4 ceramics. Linear swelling more than 1% is indication of microcrack formation or void swelling, so that mechanical integrity of these materials degrades severely. Covalent-bonded SiC and Si_3N_4 show excellent tolerance as compared with the compounds with more ionic bonding nature. Table 2 indicates change in thermal diffusivity of the same materials. It is observed that degradation of thermal diffusivity is more severe in ceramics with high thermal diffusivity before irradiation, and final values are almost the same range, but slightly higher values in the case of SiC or Si_3N_4 ceramics. It is known that the effect of neutron irradiation on thermal conductivity of ceramics appears from very low neutron doses, so that quick degradation of thermal conductivity should be carefully monitored.

Table 1. Linear swelling of typical engineering ceramics irradiated concurrently by fast neutrons [2].

Neutron fluence (n/m^2) (E_n>0.1 MeV)	Irradiation temperature (°C)	Linear swelling (%)			
		β-Si_3N_4	β-SiC	AlN	Al_2O_3
3.9 x 10^{26}	590	0.36	0.4	1.92	1.77
4.2 x 10^{26}	730	0.23	0.45	2.0	2.26
6.9 x 10^{26}	770	0.30	0.54	2.3	2.3

Table 2. Thermal diffusivity of typical engineering ceramics irradiated concurrently by fast neutrons [2].

Neutron fluence (n/m^2) (E_n>0.1 MeV)	Irradiation temperature (°C)	Thermal diffusivity (10^{-6} m^2/s)			
		β-Si_3N_4	β-SiC	AlN	Al_2O_3
Unirradiated	-	25.0	41.0	99.1	11.8
0.5 x 10^{26}	370	4.00	4.76	3.11	-
1.4 x 10^{26}	400	4.78	4.87	2.23	3.09
0.4 x 10^{26}	580	7.17	5.54	4.17	4.14

2.2. Silicon Carbide

Dimensional change due to neutron irradiation of SiC can be categorized into 3 regimes depending on irradiation temperatures if the fast neutron dose is rather high more than $1x10^{24}$ n/m^2. At low irradiation temperature (T_{irr} < ~100ºC), crystalline SiC can be amorphized by neutron irradiation greater than a few dpa (~$2x10^{25}$ n/m^2). In the intermediate temperature range (100~1050ºC), swelling induced by the strain due to irradiation-induced point defects and their small complexes saturates less than one dpa. Saturated amount of swelling is inversely related with irradiation temperature. In this temperature range, the formation speed of displaced atoms by knock-on should be balanced by recombination speed of defects. Recombination of point defects is mainly caused by the migration of interstitial atoms. At the highest temperature range studied (1050~1500ºC), migration of both irradiation-induced interstitials and vacancies is possible and to form defects clusters, such as voids, and leading to swelling that progresses with both temperature and irradiation fluence. Clusters of interstitial atoms also formed in SiC in the intermediate and highest temperature ranges. The size of such defect clusters depends on both fluence and irradiation temperature, higher fluence and increase in temperature promote formation of extended defect clusters [1].

We first observed the structure of these clusters in β-SiC (cubic), and clarified that it is an interstitial dislocation loop using high-resolution electron microscopy [3]. One tetrahedral unit sheet is inserted into {111} planes, as shown with a high-resolution electron micrograph in **Fig. 1**. Precise analysis clarified that one rotated SiC_4 tetrahedral layer was inserted into {111} planes, and Burger's vector is 1/3<111>. Structural model of defected part is shown in **Fig. 2**. Two structure models are possible candidates. The left hand model contains one insert layer, and the right hand model contains double insert layers. In both cases, direction of adjusting layer is also modified. The left hand model represents atomic arrangement of the interstitial dislocation loops.

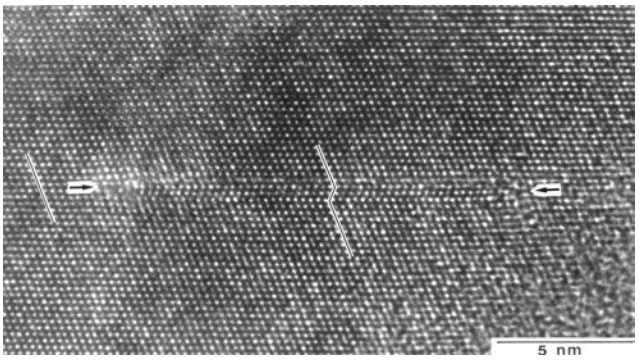

Fig. 1. A high-resolution electron micrograph of an interstitial dislocation loop formed in β-SiC crystal by neutron irradiation up to $1.0x10^{27}$ n/m^2. An extra layer is inserted into (111) planes. [3]

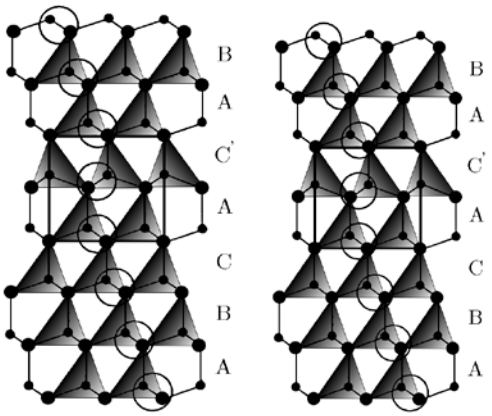

Fig. 2. Defect models for the interstitial dislocation loop formed in β-SiC crystal shown in Fig. 1. The left hand side model is most possible one [3].

Two kinds of high purity cubic (β) SiC polycrystals, PureBeta-SiC and CVD-SiC, were irradiated in the BR2 reactor (Belgium) up to a fluence of $2.0\text{-}2.5\times10^{24}$ (E>0.1 MeV) at 333-363 K. Changes in macroscopic lengths were examined by post-irradiation thermal annealing using a precision dilatometer up to 1673 K with step-heating method. The specimen was hold each temperature step for 6 h and the length change of the specimen was recorded during each isothermal annealing step from 373 K to 1673 K with 50 K increment [4].

Recovery behaviors due to isochronal annealing for 6 h from room temperature up to 1673 K of PureBeta-SiC and CVD-SiC are shown in **Fig. 3**. From the figure, we can notice that recovery behavior were mostly identical, and were started at 333-363 K which was similar with irradiation temperature, and the recombination rate was relatively high until ~573 K. After that, the recombination rate was seemed to become lower followed by saturation of recovery at elevated temperature (~1573 K). It was supposed that the both specimens contained primarily point defects or point-like small clusters due to medium neutron fluence at low irradiation temperature. Therefore, we assumed that mechanism of defects annihilation should be mainly occurred by recombination of vacancies and interstitial atoms.

The recovery curves were analyzed with first order model, and rate constants at each annealing step were obtained. **Fig. 4** shows an Arrhenius's plots using the rate coefficient that obtained from the slope of the volume change during isothermal annealing at each step of the 50 K increment. From this figure, the activation energies, E_a of the volume recovery can be determine using the slope of the straight line. Recovery of defects induced by neutron irradiation in high purity β-SiC has four stages with different activation energies. At 373-573 K, the activation energy of PureBeta-SiC and CVD-SiC were in the range of 0.17-0.24 eV and 0.12-0.14 eV, 0.002-0.04 eV and 0.006-0.04 eV at 723-923 K, 0.20-0.27 eV and 0.26-0.31 eV at 923-1223 K, and 1.37-1.38 eV and 1.26-1.29 eV at 1323-1523 K, respectively. Below ~1223

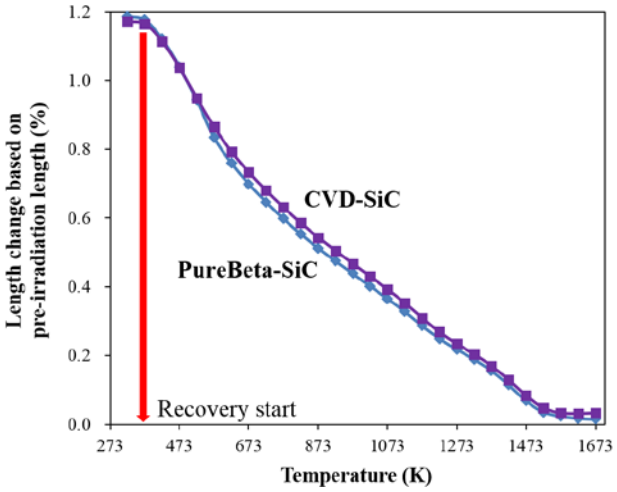

Fig. 3. Recovery behavior by isochronal annealing from room temperature up to 1673 K for PureBeta-SiC and CVD-SiC [4].

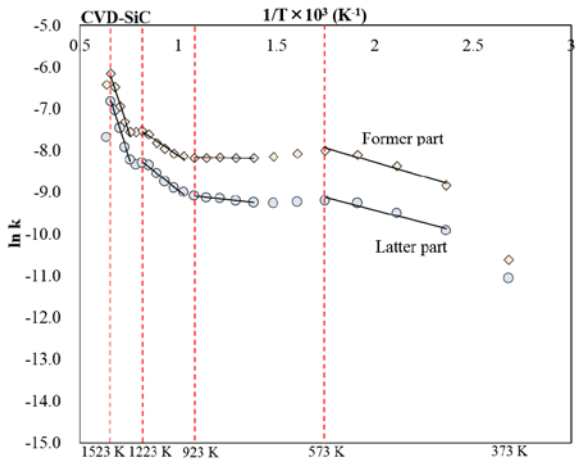

Fig. 4. The Arrhenius plot of volume recovery of CVD-SiC according to the rate coefficient, k value which obtained by first order reaction [4].

K the recombination possibly occurred for closely positioned C and Si Frenkel pairs and no long range migration is essential. Nearly three fourths of recovery induced by neutron irradiation occurs by this mechanism. In addition, at 1323-1523 K, recombination of slightly separated C Frenkel pairs and more long-range migration of Si interstitials may have occurred for PureBeta-SiC and CVD-SiC specimen. Migration of both vacancies may be restricted up to ~1523 K. Comparing to hexagonal α-SiC, high purity β-SiC recovered more quickly in the lower annealing temperature range less than 873 K, particularly less than 573 K.

2.3. Silicon Nitride and SiAlON

Research on neutron irradiation effects on Si_3N_4 is limited. Superior retention of flexural strength and thermal diffusivity to oxide ceramics such as alumina or spinel is reported for Si_3N_4 and SiAlON ceramics irradiated up to $1.0x10^{24}$ n/m^2 at 150ºC. Small swelling and relatively large drop of thermal diffusivity after irradiation up to $2.8x10^{25}$ n/m^2 (E>0.1MeV) at 740ºC are also reported. Dimensional stability of silicon nitride after concurrent neutron irradiation up to the order of 10^{26} n/m^2 was superior than that of SiC, and was kept relatively higher thermal diffusivity as same as that of SiC, as shown in Table 1 and 2, respectively [2, 5, 6].

After high dose neutron irradiation on Si_3N_4, dislocation loops are densely formed mostly parallel to the [0001] axis. From electron micrographs of the as-irradiated specimens, three different microstructures are observed [7]. In the specimen irradiated up to $0.5x10^{26}$ n/m^2 at 380ºC, no clear loop formation was identified, but small strain contrasts were densely observed throughout grains. If the irradiation temperature increased to 540ºC, tiny loop-like contrasts with distorted strain contrast were observed. After higher fluence at higher irradiation temperature, extended defect are induced. Typical dislocation loops lie on the $\{10\bar{1}0\}$ or $\{11\bar{2}0\}$ planes are named as Type-I and Type-II dislocation loops, respectively. Each configuration can be created by rearrangement of SiN_4 tetrahedra. In the Type-I dislocation, one SiN_4 tetrahedral layer is inserted into $\{10\bar{1}0\}$ planes, as shown in **Fig. 5** [7]. The defect lies horizontally at the centre of this image and is indicated by a large white arrow. From the high-resolution image, and the measured excess thickness of the planar defects of about one third of the normal unit cell spacing, it is indicated that single SiN_4 layer should be inserted between $\{10\bar{1}0\}$ planes, resulting interstitial loop formation. There is an offset of about 0.3a at the defect layer in the [1120] direction, but almost no corresponding offset in the other direction parallel to the b axis in this plane, as shown using slanted lines. The inset is the simulated image based on the structural model of Type-I dislocation, as shown in **Fig. 6**.

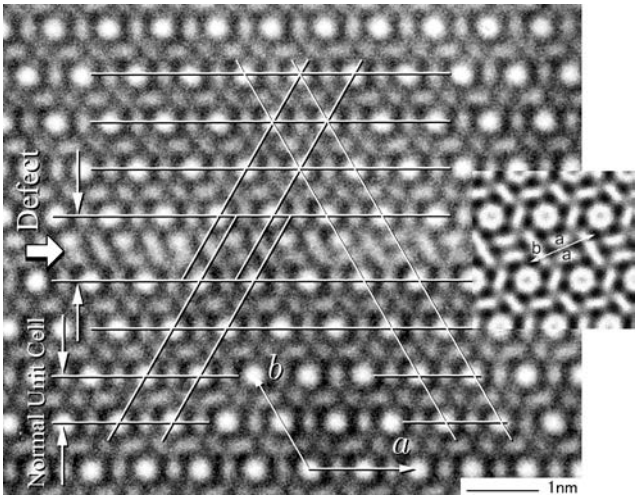

Fig. 5. A high-resolution electron micrograph of an interstitial dislocation loop (Type-I) induced by neutron irradiation up to $2.8x10^{26}$ n/m^2 at 520ºC [7].

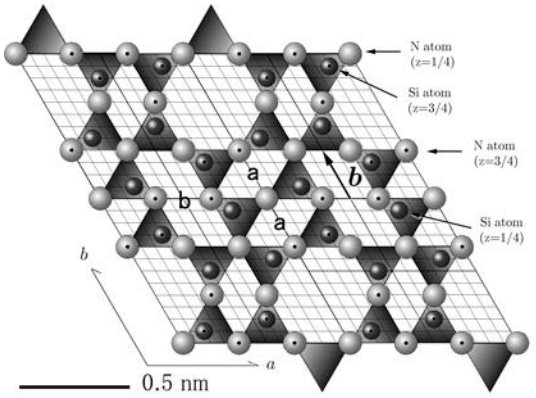

Fig. 6. Defect model for the interstitial dislocation loop formed in β-Si_3N_4 crystal shown in Fig. 5 [7].

Macroscopic length recovery of α and β-SiAlON, and α- and β-Si_3N_4 by isochronal and isothermal annealing was measured to clarify defect-recovery behavior during thermal annealing. All specimens were concurrently irradiated up to a fluence of $8.5x10^{24}$ n/m^2 (E > 0.1 MeV) at 563 K. The macroscopic length changes in term of ΔL/L, of α- and β-Si_3N_4 and α- and β-SiAlON were 0.11%, 0.06%, 0.12% and 0.14%, respectively [8]. Specimen length changes were continuously isothermally and isochronally annealed up to 1473 K using a precision dilatometer. The specimen temperature was kept constant for 3 h of each temperature step.

Recovery tendencies of the irradiated α- and β-Si_3N_4 and α- and β-SiAlON after isochronal thermal annealing for 3 h up to 1473 K are shown in **Fig. 7**. The measured recovery rates of α-Si_3N_4 and α-SiAlON were similar in shape. Both lengths began to decrease starting at the annealing temperature of slightly above the irradiation temperature, and gradually decreased with increasing annealing temperature. However, length changes of α phases of both compounds from 1123 K to 1273 K were very small compared to those of lower and higher temperatures, as indicated in Fig. 7.

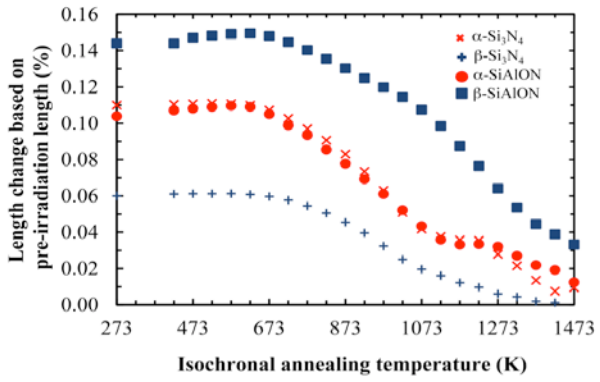

Fig. 7. Length change of irradiated Si_3N_4 and SiAlON by isochronal annealing for 3 h up to 1473 K [8].

In the case of β-Si_3N_4 and β-SiAlON, decreases in length were continuous and relatively monotonic up to the Beyond this temperature range, the length decreased again with increasing annealing temperature up to1473 K, although the absolute values were different, so that the recovery tendencies were also similar. From the Arrhenius plots as shown in **Fig. 8**(a) and (b) for α and β-Si_3N_4 respectively, it was revealed that rate constant plots could be fitted by two straight lines, one line at a lower temperature range and one at a higher temperature range. The same features were observed in the Arrhenius plots for α- and β-SiAlON [8].

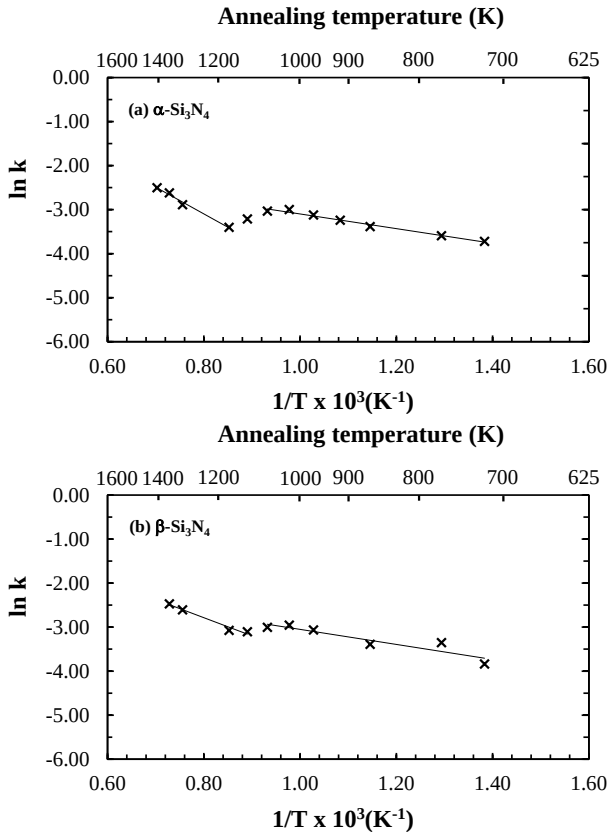

Fig.8. Arrhenius plots of volume recovery for α- and β-Si_3N_4 [8].

Table 3. Activation energy of length recovery during annealing process [8].

Specimens	Temperature range (K)	Activation Energy (eV)
α-Si_3N_4	723-1073	0.35
	1273-1473	0.97
β-Si_3N_4	723-1073	0.39
	1273-1473	0.70
α-SiAlON	723-1073	0.09
	1273-1373	0.26
β-SiAlON	723-1073	0.06
	1273-1473	0.13

At the lower temperatures, the recovery occurs easily by the annihilation of closely spaced Frenkel pairs. On the other hand, at the higher temperatures, the recovery could be governed by the recombination of Frenkel pairs separated by slightly longer distances, which would include migration of interstitials or vacancies.

Activation energies for recovery of α-Si_3N_4 are almost the same at lower temperatures, but slightly higher for higher temperatures compared to corresponding value for β-Si_3N_4, as listed in **Table 3** [8]. It is suggested that interstitial atoms in α-Si_3N_4 migrate with more difficulty at higher temperatures. The activation energies for length recovery of both Si_3N_4 polymorphs were higher than those of corresponding SiAlON polymorphs at lower and higher temperatures. The reason for this may be attributed to the difference in atomic bonding nature. Covalent Si–N bonding strength in Si_3N_4 crystals is higher than covalent/ionic bonding strengths in SiAlON crystals. During annealing process, point defects induce distortion of surrounding lattice to dissociate or to migrate, and then atomic bonding strength of surrounding lattice should affect these processes.

2.4. Aluminum Nitride

Aluminum nitride (AlN) ceramics with very high thermal conductivity and high electrical resistivity have been developed recently, therefore, neutron irradiation data on AlN are very limited compared with those of alumina, particularly at high fluence. The crystalline phase of AlN is 2H-type, hexagonal wurtzite structure. The structure is presented as a sequential stacking of AlN_4 tetrahedral sheets, parallel to the (0001) plane. From limited data, it appears that the anisotropic feature of the irradiation response is similar to that of alumina, except for voids formation only in alumina [1].

According to the increase of fast neutron fluence roughly more than $5x10^{24}$ n/m^2, length of the a-axis and c-axis crystalline lattice due to the irradiation are swelled isotropic to anisotropic in manner. Beyond $5x10^{24}$ n/m^2, the ratio of the *c*-axis length/*a*-axis length increases markedly. In anisotropically changed specimens, dense tiny interstitial dislocation loops are observed on the (0001) basal plane [9], as shown next. Further increase in fluence and/or higher irradiation temperature, finally strain caused by anisotropic swelling of grains induces microcracks along grain boundary. It is also clearly indicated from the departure of macroscopic volume change and unit cell volume change, as shown in **Fig. 9** [10].

A high-resolution electron micrograph taken along the [$11\bar{2}0$] incident beam direction of AlN specimen neutron-irradiated to $2.4x10^{24}$ n/m^2 is shown in **Fig. 10** [9]. This projection shows both the (0001) basal plane and the {1100} prism planes edge on view. A two-layer repeat of 0.25 nm-spaced fringes along the [0001] is clearly observed. One array of black dots contrast parallel to the (0001) plane corresponds to one tetrahedral layer. The array of dot parallel to the (0001) planes is waved at the center part labeled X or Y. In this case, single extra layer parallel to the (0001) plane is inserted between the original stacking layers. The stacking sequence perpendicular

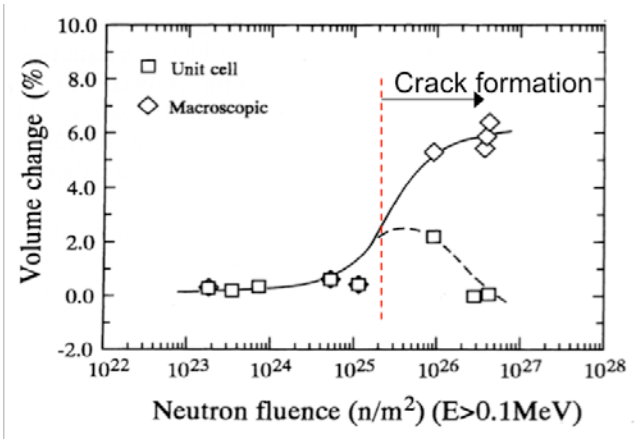

Fig. 9. Effect of fluence on the macroscopic and unit cell volume changes in AlN. [10]

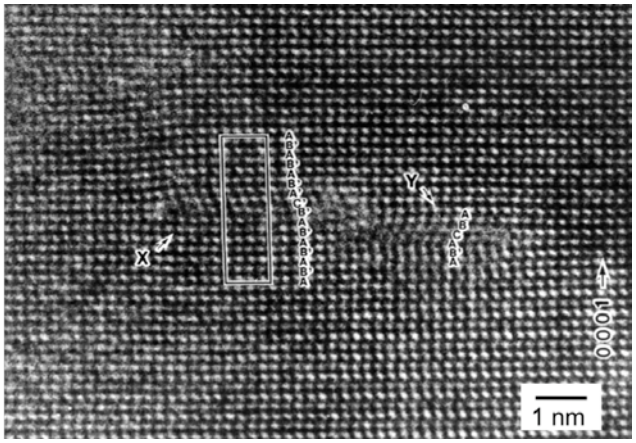

Fig. 10. A high-resolution electron micrograph taken along the [$11\bar{2}0$] incident beam direction of the specimen neutron-irradiated to 2.4 x 10^{24} n/m^2. [9]

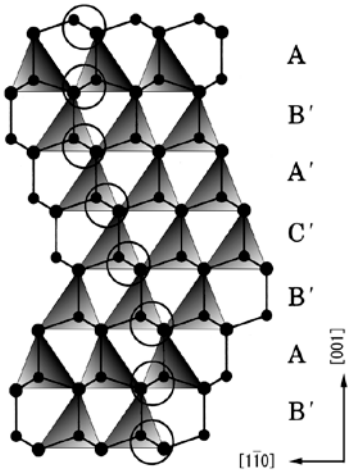

Fig. 11. Atomic arrangement of interstitial dislocation loop formed in AlN [9].

to the loop plane is estimated to be AB'/A'C'/B'A as a result of an A layer plus an inserted layer creating A'C' layers. The atomic arrangement of this stacking sequence is modeled in **Fig. 11**. Another possible variant of the stacking sequence is AB'A/BC/AB' as a result of B' layer plus an inserted layer creating BC layers. This model gives the opposite stacking direction of sphelerite layers. The loop labeled Y in Fig. 10 coincides with this stacking sequence model. The Burgers vector of the loops is (1/2)[0001].

The AlN specimens were neutron-irradiated in the Japan Materials Testing Reactor with two different conditions, 89F5U were irradiated up to 4.4 x 10^{23} n/m^2 (E > 0.1 MeV) at 573 K (capsule irradiation in helium atmosphere), and U702 were irradiated up to 8.3 x 10^{22} n/m^2 (E > 0.1 MeV) at 373 K (Hydro rabbit irradiation) [11]. The results show a major effect of irradiation on materials length swelling which the higher neutron fluence and irradiated temperature of 89F5U showed a higher percentage of swelling for 0.140% while the lower neutron fluence and irradiated temperature of U704 showed the lower percentage of 0.108%. The lattice parameter change showed the expansion of the irradiated specimens 89F5U and U704 for 0.20% and 0.13% in a-axis and 0.24% and 0.14% in c-axis, respectively. The expansion is mostly isotropic. Recovery behavior of irradiated specimens by thermal annealing for 6 h are shown in length change percentage in **Figure 12** [11]. The recovery pattern and isothermal result indicate the starting of recovery at 423 K followed by the rapid shrinkage in change until 523 K. Then, the length was slightly decreasing until reach to the maximum recovery temperature at 1573 K. Moreover, at the above maximum recovered temperature of 89F5U, the length has begun to increase. It is thought that the expansion occurred by the effect of surface oxidation or He bubble generation.

Rate constants of length recovery of the irradiated specimens at each isochronal annealing step was analyzed by the first order reaction model and plotted against inverse of absolute temperature of annealing in **Fig. 13**.

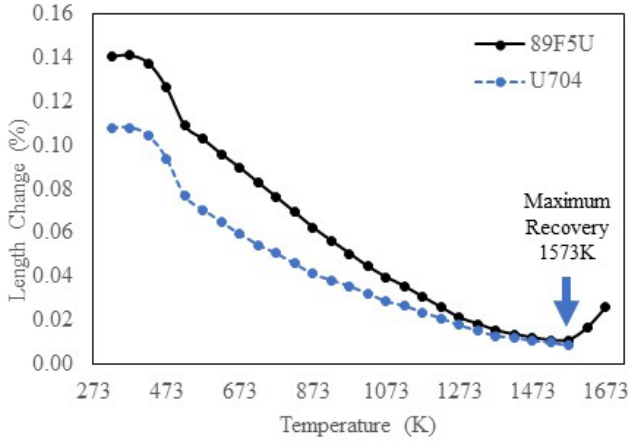

Fig. 12 Recovery behavior in length of 89F5U and U704 AlN specimens [11].

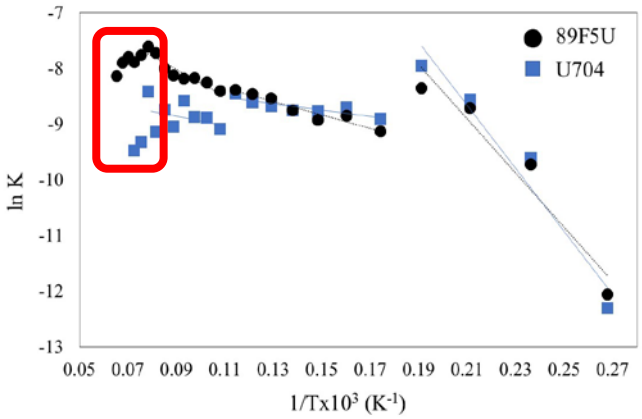

Fig. 13 Arrhenius plots of length recovery for 89F5U and U704 AlN specimens [11].

Table 4. Activation energy of length recovery for the irradiated AlN specimens [11].

Specimen	Temperature Range (K)	Activation Energy (eV)
89F5U	373 – 523	4.19
	523 – 873	1.05
	873 – 1273	2.08
U704	373 – 523	4.86
	523 – 873	0.49
	873 – 1073	2.61

Obtained activation energies from Arrhenius' plots are listed in **Table 4**. The Arrhenius' plots suggested the separation in reaction into three temperature regions. The first region at low temperature range from 373 K to 523 K corresponds to the quick recovery region from the starting temperature of the length recovery. The next regions are curing 523 K to the maximum recovered temperature which can be divided into two sub-ranges of from 573 K to 873 K and from 873 K to 1273 K. At the temperature beyond 1273 K, the rate constants scatter or decrease, that should be the indication of oxidation of specimens or He bubbles formation. Obtained activation energies in the lowest temperature range were ~4.5 eV. These values are one order of magnitude greater than that of high-purity SiC. From 523 K to 873 K, activation energies of 0.5~1.0 eV were obtained. These values roughly corresponded with reported Al-interstitial migration energy in Al_2O_3. More than 873 K, little greater activation energies were obtained. Total tendencies of change in activation energies with increasing annealing temperature of the present neutron-irradiated AlN was resemble with those of SiC [4] and different from that of Al_2O_3 [12]. This incident may be related with the structure feature of AlN, which is similar with that of SiC and possess half-covalent bonding nature.

Acknowledgments

The author wish to express my gratitude to many graduate students in my laboratory, listed below, for their essential study on the neutron irradiation damage of ceramics. Their continuous researches contribute the progress of this basic but interesting area. Due to the page limitation, only small parts of results are included into this review.

Special thanks to: Tetsuya Suzuki, Hisayuki Suematsu, Yasumasa Fukushima, Mitsuharu Tezuka, Chang Sam Kim, Hiroshi Sawada, Masanori Ikari, Andon Insani, Masakatsu Suzuki, Masafumi Akiyoshi, Kohki Ichikawa, Yoshiro Yamamoto, Yudi Pramono, Khoichi Inokuchi, Kunio Fukuda, Saishun Yamazaki, Kousuke Yamaya, Hiroko Kawano, Takashi Sawabe, Tomoyuki Yamagami, Hiroshi Konishi, Yusuke Futamura, Areerak Rueanngoen, Koumei Kanazawa, Mohd Idzat Idris, Yan You, Yuhao Jin, Thanataon Pornphatdetaudom.

Most of the irradiation experiments were performed using Japan Materials Testing Reactor with support from the staff of the International Research Center for Nuclear Materials Science, Institute for Materials Research, Tohoku University. I gratefully acknowledge their cooperation.

Reference

1. T. Yano and B. Matovic, “Advanced Ceramics for Nuclear Applications”, Chap. 4.3, in Handbook of Advanced Ceramics, 2nd Edition, Ed. by Shigeyuki Somiya, Academic Press (Elsevier), (2013). pp.353-68, ISBN:9780123854698

2. M. Akiyoshi and T. Yano, “Neutron-irradiation effect in ceramics evaluated from macroscopic property changes in as-irradiated and annealed specimens”, Prog. Nucl. Energy, **50**, 567-574 (2008).

3. T. Yano and T. Iseki, "High-Resolution Electron Microscopy of Neutron-Irradiation-Induced Dislocations in SiC", Phil. Mag., **A62**, 421-430 (1990).

4. M. I. Idris, S. Yamazaki, K. Yoshida, and T. Yano, “Recovery behavior of high purity cubic SiC polycrystals by post-irradiation annealing up to 1673K after low temperature neutron irradiation”, J. Nucl. Mater., **465**, 814-819 (2015).

5. T. Yano, M. Akiyoshi, K. Ichikawa, Y. Tachi, and T. Iseki, "Physical Property Change of Heavily-Neutron-Irradiated Si_3N_4 and SiC by Thermal Annealing", J. Nucl. Mater., **289**, 102-109 (2001).

6. M. Akiyoshi, K. Ichikawa, T. Donomae, and T. Yano, "Macroscopic Properties and Microstructure Changes of Heavily Neutron-Irradiated β□Si_3N_4 by Annealing", J. Nucl. Mater., **307-311**, 1305-1309 (2002).

7. M. Akiyoshi, T. Yano, and M. L. Jenkins, "A Structural Model of Defects in β□Si_3N_4 Produced by Neutron-Irradiation", Phlos. Mag. **A81**, 683-697 (2001).

8. A. Rueanngoen, K. Kanazawa, M. Imai, K..Yoshida, and T. Yano, “Analysis of recovery process of low dose neutron irradiation-induced defects in silicon nitride-based ceramics by thermal annealing”, J. Nucl. Mater., **455**, 464-469 (2014).

9. T. Yano and T. Iseki,"A HREM Study on Neutron-Irradiation-Induced Dislocations in Aluminum Nitride", Phil. Mag. Lett., **62**, 83-87 (1990).

10. T. Yano, K. Ichikawa, M. Akiyoshi, and Y. Tachi, "Neutron Irradiation Damage in Aluminum Oxide and Nitride Ceramics up to a Fluence of $4.2x10^{26}$ n/m²", J. Nucl. Mater., **283-287**, 947-951 (2000).

11. T. Pornphatdetaudom, T. Yano, and K. Yoshida, “Physical Property changes of neutron-irradiated aluminum nitride and their recovery behavior by annealing using a step-heating dilatometer”, J. Mater. Energy (submitted)

12. T. Yano, H. Konishi, S. Yamazaki, M. I. Idris, and K. Yoshida, “Recovery of neutron-irradiation-induced defects of Al_2O_3, Y_2O_3, and yttrium-aluminum garnet”, J. Nucl. Sci. Technol., **54**, 891-898 (2017).

I.2 Retrospection of My 43-Years' Researches

Minoru TAKAHASHI

1. Introduction

I was deeply impressed by the first research for my Bachelor's degree thesis in 1974: "How exciting research works are!" Since then, I challenged various research topics. Through the works, I had wonderful time with a lot of people including students. In retirement in March of 2018, I would retrospect my 43-years' researches.

2. Researches for degree theses and dissertation

2.1. Abnormal elongation "Super-plasticity"

I succeed in realizing super-plasticity of Al-Zn alloy in the beginning of 1975. The super-plasticity is a special type of creep deformation phenomena. Material elongates under tensile stress, and the strain reaches several hundreds percent. The good specimens (Fig.1) could be fabricated by trial-and-error. According to metallurgical observation, the superplasticity was caused by fine crystal grains. This experience of material study motivated my following researches.

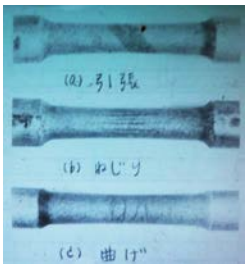

Fig.1 Specimens for super-plasticity test

2.2. Circulation of lead alloy

I circulated a heavy liquid metal with water in 1974. It was the start of my next interesting research that continued for Master's degree thesis and Doctoral dissertation till 1979. The heavy metal (48Bi-26Pb-13Sn-13Cd) was called "Wood's metal" with low melting point.

I conducted this experiment to simulate the direct contact of core melt with a coolant. The heavy liquid metal at high temperature was circulated simultaneously with low temperature water in a dual loop (Fig.2), and directly contacted with the water as a cocurrent stratified flow in a horizontal channel. I found that interfacial heat transfer coefficient between two liquids was remarkably high compared with normal heat transfer coefficients on solid surfaces [1]. It was considered that liquid-liquid interfacial turbulence was much stronger than the turbulence close to a solid surface, and as a result the laminar sublayer was much thinner. I incorporated a special turbulence damping model into the two-equation model of turbulence to simulate the flows and interfacial heat transfer of the water-liquid metal concurrent stratified flow in 1979 [2].

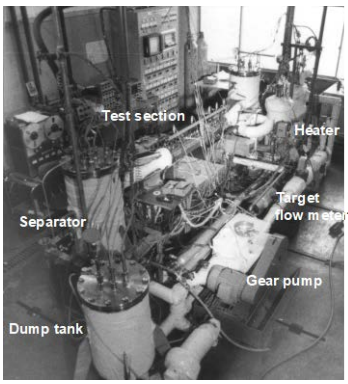

Fig.2 Heavy metal-water loop

I also found that direct contact boiling heat transfer was very high in the water-liquid metal concurrent flow in 1979..

3. Researches on thermal-hydraulic phenomena related to nuclear reactors

3.1. Direct contact condensation in ECCS

Emergency core cooling system (ECCS) works at the loss of coolant accident (LOCA) in light water reactors (LWR). Cold water is injected into the reactor pressure vessel through a down-comer. This thermal-hydraulic phenomenon is dominated by interfacial condensation heat transfer. I investigate the characteristics of direct contact condensation heat transfer in a steam-water concurrent stratified flow in 1884-1885; on cold water jet in 1988; and on a water spray in 1997. The heat transfer was dominated by turbulence in the vicinity of the interface on liquid water side. I incorporated a special turbulence damping model into the two-equation model of turbulence to simulate condensation heat transfer of the steam-water concurrent stratified flow.

3.2. Air-water two-phase flow

As mentioned above, interfacial turbulence has an influence on interfacial heat transfer. Thus, the turbulence characteristics of an air-water turbulent stratified flow in an inclined duct were studied experimentally and analytically in 1994-1996. Turbulence properties in the water side was measured using a laser-Doppler velocimeter, and analytical simulation was performed using the two-equation model of turbulence with the interfacial turbulence damping model.

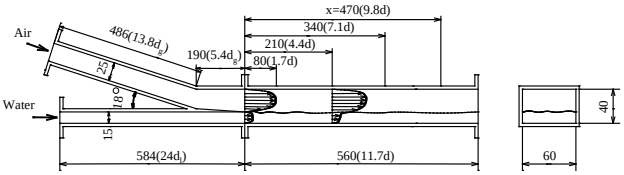

Fig.3 Steam-water and air-water stratified flows

3.3. Liquid flow falling along wall

By simulating the liquid lithium target of the international fusion irradiation facility (IFMIF), the characteristics of water and mercury flows falling along a vertical wall were investigated in 1998-2000. The liquid surfaces were free from shear stress. We measured turbulence in the water flow using a laser-Doppler velocimeter and measured turbulence in the mercury flow under a weak magnetic field using an electromagnetic potential probe. The results were compared with calculated results. We could simulate the damping of turbulence in the flow direction analytically using the two-equation model of

turbulence with the turbulence damping model close to the free surface.

3.4. Water hammer and Chugging

I focused on unstable steam condensation phenomena accompanied by very high pressure pulses in direct contact of steam with a cold water. Structure is mechanically damaged by the high pressure pulses. One of them is called "water hammer" that occurs in a steam pipe, and another is "Chugging" that occurs in the suppression pool of light water reactor. We investigated the onset conditions of the water hammer in 2002 and of the Chugging in 2014-15 [3].

3.4. Burnout and decay heat cooling phenomena

If the neutron spectrum in light water reactor (LWR) core is made harder by reducing the volume ratio of moderator-to-fuel, i.e., a tight lattice core, the conversion ratio can be nearly equal to unity even in LWRs. Such reactor is called "reduced-moderation water reactor (RMWR)". We recommended a triangular fuel rod arrangement with wire spacers as the tight fuel bundle. One of the most crucial issues was fuel rod cooling. We investigated the characteristics of burnout heat flux or critical heat flux (CHF) in the tight fuel bundle experimentally in 2013-2015. We found that the existence of a wire spacer increased the CHF compared with no spacer [4].

At the accidents of Fukushima Daiichi Nuclear Power Plants, decay heat removal in the core was failed due to the descending of water level. We performed a simulation experiment to investigate the behavior using a single heater pin in 2011. We found that repeated sudden boiling of water followed by splash from below could wet the upper part of the heater pin exposed to a steam flow.

3.5. Extraordinary behaviors of magnetic fluids

Special fluids attracted by a magnet are called "magnetic fluid" or "ferrofluid". They are the liquids in which particles of ferromagnetic material with nanometer size are dispersed stably and uniformly. We investigated the extraordinary behaviors of enhancement and deterioration of boiling heat transfer and the flow characteristics of a gas-magnetic fluid two-phase flow in a field gradient experimentally in 1901-1909 [5]. As an application of the magnetic fluids, we proposed a magnetic fluid thermosiphon that worked under a magnetic field gradient even without gravity force in 2000 [6].

4. Research and development for sodium-cooled fast reactor (SFR)

4.1. Sodium cavitation in fast reactor "Monju"

Vaporization of coolant sodium is possible in the primary circuits of prototype fast reactor "Monju" operated at low system pressure. Such vaporization occurs at the local acceleration region where the static pressure reaches the saturation pressure. The vapor bubbles collapse in decelerated region downstream due to the recovery of pressure. This phenomenon is called "cavitation". The collapse of bubbles generates high pressure pulses that damage structural materials. This damage is called "cavitation erosion". For the integrity of the structural materials in "Monju" reactor, the cavitation and erosion should be avoided by means of hydrodynamic design measure.

I conducted simulation experiment for the entrance nozzles of core fuel assemblies, and found that cavitation easily occurred in the centers of tiny vortices like bath-tub vortices detaching from inner wall of a connecting tube in 1985. Based on the result of the cavitation experiment, I proposed the modified designs of the entrance nozzles and the connecting tubes in 1986. Fig. 4 shows an example of cavitation where bubbles can be seen above a horizontal support rod of a neutron shield in core fuel assembly.

Later again, I investigated the characteristics of water and sodium cavitation and erosion in a venture tube in 2007-2011 [7].

Fig.4 Water cavitation

4.2. Decay heat removal in fast reactor "Joyo"

One of the most crucial issues for the safety of sodium-cooled fast reactors is decay heat removal after a pump trip and reactor shutdown. The performance of auxiliary cooling systems for the decay heat removal was demonstrated experimentally in the experimental fast reactor Joyo.

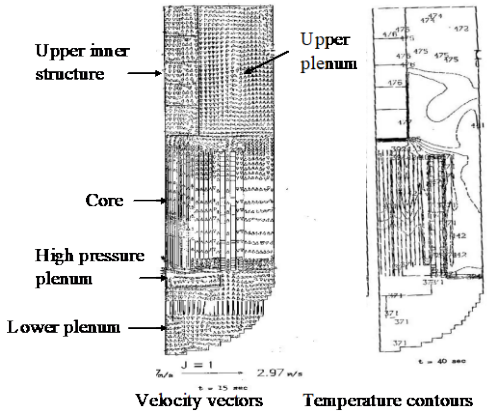

Fig.5 Analysis of Joyo in-vessel convection

I evaluated a computational simulation method for decay heat removal by using thermal-hydraulic numerical codes. A set of the codes consists of a system analysis code, an in-vessel multi-dimensional CFD code and a sub-channel analysis code. By using the CFD code, I performed whole in-vessel thermal-hydraulic analysis using the CFD code in 1988 (Fig.5). It was the first whole in-vessel analysis in Japan.

4.3. Gas entrainment from liquid free surface

In the design of demonstration fast reactor in Japan,

reactor vessel and components were compact for economical reason. Therefore, velocity was high in the primary coolant system. The high velocity induces gas entrainment from argon cover gas into primary coolant sodium. As void reactivity is positive, the gas entrainment should be prevented so that bubbles did not enter the core. We investigated the onset condition of gas entrainment and gas entrainment rate experimentally as shown in Fig.6. We found that even a thin bath-tub vortex caused high gas entrainment rate in 1985-1986 [8].

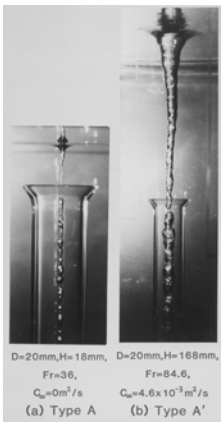

Fig.6 Gas entrainment

5. Safety study for high temperature gas-cooled reactor (HTGR)

Helium coolant depressurization accident is one of the crucial safety issues for high temperature gas-cooled reactor (HTGR). In this accident scenario, it is necessary to consider air ingress accident where chemical reaction of air with graphite produces explosive and toxic CO gas at high temperature. We investigated the burn-off and production of CO and CO_2 in oxidation of nuclear reactor-grade graphite experimentally at high temperature [9].

6. Research and development for lead alloy-cooled fast reactor (LFR)

6.1. Compatibility of materials with liquid lead alloys

Lead alloy-cooled fast reactors (LFR) have advantages in reactor performance and inherent safety. However, these coolants are corrosive to structural materials in high temperature range of fast reactors. Thus, we conducted material corrosion experiment extensively using static pot apparatuses and the corrosion test loop (Fig.7).

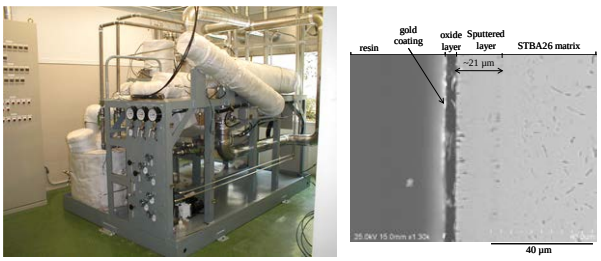

Fig. 7 Corrosion test loop and Al-Fe alloy-coated steel

We found that ferritic-martensitic steels with high chromium content had better corrosion resistance than austenitic stainless steels, and the addition of aluminum and silicon into the steels could improve the corrosion resistance in 2000-2005 [10]. We also found that aluminum-iron alloy-coated steels were not corroded at higher temperature in 2006-2008 [11]. Various corrosion phenomena in high temperature lead-bismuth were investigated for materials of refractory metals, ceramics, ceramics-coated steels, cold-worked and welded steels, and bended steels in 2006-2011.

6.2. Oxygen sensor for liquid lead alloys

Reliable oxygen sensor is required to monitor the oxygen potential in lead alloy coolants during reactor operation. That is because the oxygen potential must be kept low enough so that solid lead oxide is not formed in the coolant, and the oxygen potential must be high enough so that corrosion protection layers of oxides are self-healed on structural material surfaces. We investigated the performance and characteristics of zirconia solid electrolyte oxygen sensors in 2005 and in 2013-2017 [12].

6.3. Thermal-hydraulics of liquid lead alloys

Steam generator (SG) pipe break accident is one of important safety issues in lead alloy-cooled fast reactors because the SGs are located inside the reactor vessel. At the pipe break accident, high pressure water and steam will be discharged from the broken pipes into the primary coolant, and thermal interaction occurs in contact with high temperature liquid lead alloy. We investigated violent boiling behaviors when a lead alloy droplet fell into water pool, and when steam was injected into a pool of liquid lead alloy in 2007-2011 [13].

6.4. Transport properties of liquid lead alloys

As a coolant technology, metallic and non-metallic impurities dissolved in the coolant of liquid lead alloy should be well controlled in the operation of lead alloy-cooled fast reactors. The transport of the impurities can be calculated analytically using mass conservation equations containing diffusion terms. Diffusion coefficients of impurities are required in the calculation as the transport properties of liquid lead alloys. We measured the diffusion coefficients of iron, nickel and oxygen in lead alloys in 2009-2011 and in 2012-2017 [14]. The molecular dynamics simulation was applied to the calculation of the properties in comparison with measured results in 2015.

6.5. Innovative lead-bismuth-cooled fast reactor concepts

We proposed the development of lead alloy-cooled fast reactor because it has good nuclear, thermal, and chemical properties for inherent safety. We also recommended to decrease the contacting area of structural material with lead alloy as much as possible because lead alloy was corrosive to structural materials and caused material erosion easily at high velocity. It is possible to decrease the contacting area by eliminating primary mechanical pumps and steam generators.

The elimination can be done by feeding water directly into lead-bismuth above the reactor core as shown in Fig.8(a). Steam is generated by the direct contact of the feed water with high temperature lead-bismuth, and the buoyancy force acting to steam bubbles can circulate the primary coolant. Thus, we proposed the innovative fast reactor concept called "*Pb-Bi-cooled boiling water small fast reactor (PBWFR)*" (Fig.8) in 2002-2004 [15]. PBWFR consists of lead-bismuth-cooled fast reactor core and the balance of plant (BOP) of boiling water reactor (BWR). The PBWFR can be called "*Simplified Lead- bismuth-cooled fast reactor-boiling water type, SLFR-B*", or

"*Boiling water lead-bismuth-cooled fast reactor, BLFR*".

Polonium-210 (alpha-ray emitter) produced in primary coolant contaminates the steam turbine system in PBWFR. In order to prevent the contamination in the steam system, I proposed another innovative reactor concept in 2014-2015. This reactor concept is the combination of lead-bismuth-cooled fast reactor core and the balance of plant (BOP) of pressurized water reactor system. By the isolation of SG, polonium-210 does not contaminate the steam system. This reactor was named "*Simplified Lead-bismuth-cooled fast reactor-pressurized water type, SLFR-P*", or "*Pressurized water lead-bismuth-cooled fast reactor , PLFR*".

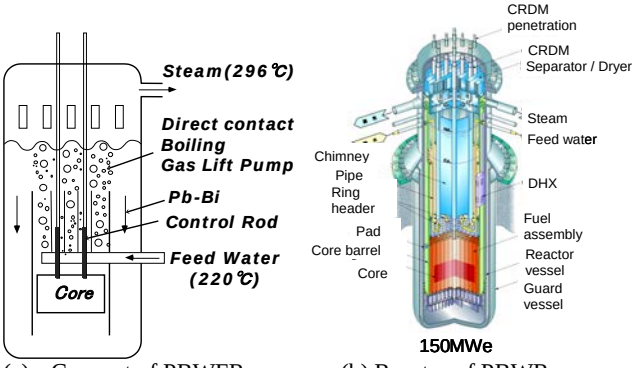

(a) Concept of PBWFR (b) Reactor of PBWR

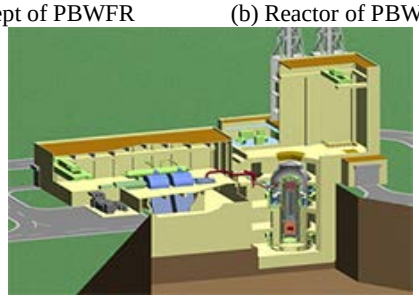

(c) Layout of PBWR system

Fig.8 Innovative lead-bismuth-cooled fast reactor PBWFR

6.6. Studies to support innovative fast reactor concepts

The feasibility of the PBWFR concept was studied by using Pb-Bi-water direct contact boiling water test loop (Fig.10) with 4-pin heater pin bundle that was set up in 2003. The rated flow and steam generation condition of the practical PBWFR was experimentally demonstrated using the test loop in 2004-2006 [16].

Safety analysis was performed, and it was found that the severe core damage could be prevented for the events of the unprotected loss of heat sink (ULOHS) and the unprotected loss of flow (ULOF), *i.e.*, the tolerance characteristics of the anticipated transient without scram (ATWS) was confirmed in 2006 [17].

Liquid droplets are entrained from lead alloy free surface, conveyed to a steam turbine and damage turbine blades. To prevent the droplet problem, we proposed the equipment of electrostatic precipitators for droplet removal. We investigate the removal performance of the precipitator in 2003-2006.

The boiling flow in direct contact of feed water and lead alloy in a chimney of PBWFR was simulated using the multi-fluid model in 2005-2008 [18].

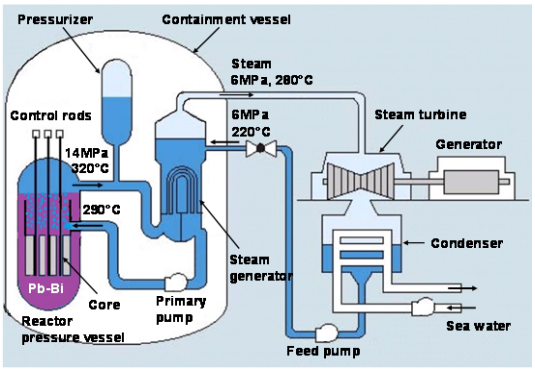

Fig.9 Innovative lead-bismuth-cooled fast reactor PLFR

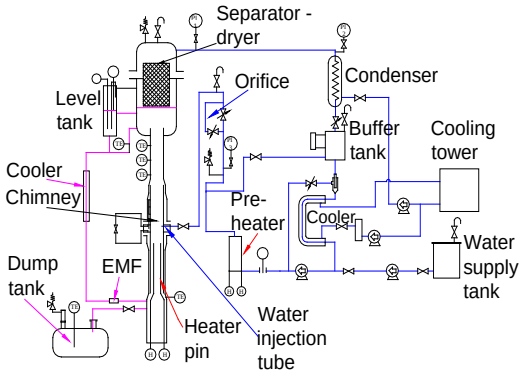

Fig.10 Pb-Bi-water direct contact boiling water test loop

7. Lithium-cooled blanket of fusion reactor

7.1. Concept of innovative liquid lithium-cooled blanket

Lithium cooling of the first walls and blankets of magnetically confined fusion reactors has excellent features of high heat transfer performance and good tritium breeding capability as well as simple and light blanket. However, it has too high magneto-hydrodynamic (MHD) pressure drop under a strong magnetic field. One of critical issues of the lithium cooling is how to reduce the MHD pressure drop. Injection of helium gas into the lithium coolant is one of the solutions. We proposed the innovative concept of helium-lithium two-phase flow cooling for the fusion reactors in 1989 [19].

7.2. Lithium experiment for fusion blanket study

In order to demonstrate the feasibility of the helium-lithium two-phase flow cooling, the characteristics of MHD flow and heat transfer of the helium-lithium two-phase flow were studied under a transverse magnetic field extensively [20]. A special helium-lithium two-phase flow loop was setup for the experimental studies (Fig.11).

7.3. Mercury experiment for support of fusion blanket study

We used mercury as a simulant liquid of lithium for fundamental MHD experiments. The effect of magnetic field on mercury thermal-hydraulics was investigated for pool boiling [21], a single-phase flow, falling film flow, and air-mercury two-phase flows. MHD turbulence damping and enhancement were observed through velocity

fluctuation measurement using potential probe.

7.4. MHD turbulence in analytical model

I made special MHD models for liquid metal *k-ε* turbulence model and for liquid metal boiling under a magnetic field. The models were incorporated into analytical program to simulate the liquid metal MHD phenomena [22]

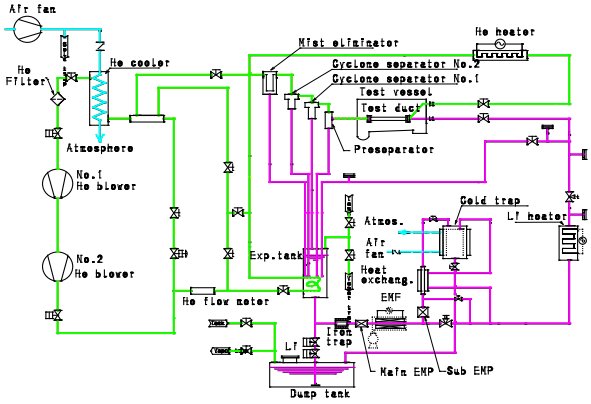

Fig.11 Helium-lithium two-phase flow loop

8. Liquid lithium target for neutron source of BNCT

A compact medical system for boron neutron capture therapy (BNCT) is expected to be facilitated near hospitals. The compact BNC system can be made by developing a neutron source with a flowing lithium target and a proton beam accelerator. We proposed a liquid lithium target system with a thin liquid lithium sheet jet (Fig.12).

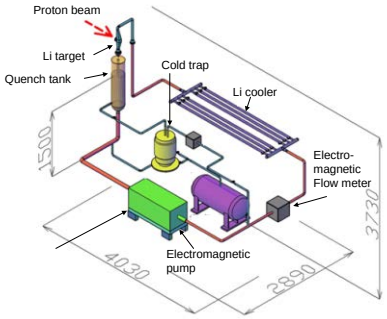

Fig.12 Liquid lithium target system for BNCT

In order to develop the liquid lithium target system, we conducted a water and lithium experiment in 2008-2010 [23]. It was found that disturbances produced at a nozzle inlet had a large influence on the stability of the lithium sheet jet. We proposed a long nozzle in which disturbance generated at the nozzle inlet damped at the nozzle outlet. Furthermore, we found through CFD simulation that round chamfers or tiny projections at the nozzle inlet could effectively prevented disturbances from traveling to the nozzle outlet even in shorter nozzles, and as a result lithium sheet jet became stable in 2016.

9. Summary

My research fields were over various areas. However, most of the researches were related to liquid metals. In addition, my interest was mainly directed to the safety of light water reactors, and development of sustainable energy systems such as fast reactors and fusion reactors. Anyway, my motive of the researches was always for safe, effective and sustainable utilization of nuclear energy for the welfare of future society.

References

1. M. Takahashi, et al.; Bulletin of the JSME, Vol.23, No.177, pp.376-384 (1980).
2. M. Takahashi, et al.; Bulletin of the JSME, Vol.24, No.192, pp.1002-1010 (1981).
3. G. Gregu, et al.; International Journal of Multiphase Flow, Vol.88, pp.87-98 (2017).
4. T. Le, et al.; Journal of Energy and Power Engineering, Vol.10, No. 2, pp.109-115 (2016).
5. M. Takahashi, et al.; International Journal of Multiphase Flow, Vol.20, No.6, pp.1095-1107 (1994).
6. T. Hongo, et al.; JSME International Journal, Vol.43, No.4, (2000) pp.686-693.
7. T. Ardiansyah, et al.; Journal of Power and Energy System, Vol. 5, No.1, pp.33-44 (2011).
8. M. Takahashi, et al.; Journal of Nuclear Science and Technology, Vol.25, No.2, pp.131-142 (1988).
9. M. Takahashi, et al.; Journal of Nuclear Science and Technology, Vol.31, No.12, pp.1275-1286 (1994).
10. M. Kondo, et al.; Journal of Nuclear Science Technology, Vol.43, No.2, pp.107-116 (2006).
11. A. Rivai, et al.; Progress in Nuclear Energy, Vol. 50, pp.560-566 (2008).
12. P. M. Adhi, et al.; Sensors & Actuators: B. Chemical, Vol. 241, pp. 1261–1269 (2017).
13. R. Sa, et al.; Journal of Energy and Power Engineering, Vol. 5, No.7, pp.579-589 (2011).
14. Y. Gao, et al.; Mechanical Eng. J., Vol. 2, No.6, (2015), [DOI: 10.1299/mej.15-00149].
15. M. Takahashi, et al.; Progress in Nuclear Energy, Vol. 50, pp.197-205 (2008).
16. M. Takahashi, et al.; Progress in Nuclear Energy, 47/1-4, pp. 569-576 (2005).
17. M. Takahashi, et al.; Progress in Nuclear Energy, Vol. 50 pp.269-275 (2008).
18. Y. Yamada, et al.; Journal of Power and Energy Systems, Vol. 2, No. 2, Special Issue on 15th International Conference on Nuclear Engineering, pp..479-491 (2008).
19. M. Aritomi, et al.; Fusion Engineering and Design, Vol.8, pp.289-295 (1989).
20. M. Takahashi, et al.; Fusion Engineering and Design, Vol.39-40, pp.799-809 (1998).
21. M. Takahashi, et al.; Experimental Thermal and Fluid Science, Vol.8, pp.67-78 (1994).
22. M. Takahashi, et al.; Fusion Engineering and Design, Vol.8, pp.249-256 (1989).
23. M. Takahashi, et al.; Journal of Power and Energy Systems, Vol.6, No.2, pp.324-338 (2012).

II. Research Reports

A. Innovative Nuclear Energy System Division

A.1 Progress in Study of Innovative Nuclear Energy System Concepts and Criticality Safety for Fuel Debris and Fuel Solutions

Toru OBARA

Several studies on innovative nuclear reactor concepts and criticality safety have been performed. The studies were focused on the concept of pebble bed high-temperature gas-cooled reactors, CANDLE burning reactor, and criticality safety issues in fuel debris and fuel solutions.

1. Study on passive decay-heat removal in pebble bed high temperature gas-cooled reactor

Conditions for design parameters of above-ground and underground, prismatic high temperature gas-cooled reactor (HTGR)s for passive decay heat removal based on fundamental heat transfer mechanisms were obtained in the previous works. In the present study, analogous conditions were obtained for pebble bed reactors by performing the same procedure using the model for heat transfer in porous media of COMSOL 4.3a software, and the results were compared. For the power density profile, several approximated distributions together with original one throughout the 10-MWt high-temperature gas-cooled reactor-test module (HTR-10) were used, and it was found that an HTR-10 with a uniform power density profile has the higher safety margin than those with other profiles. In other words, the safety features of a PBR can be enhanced by flattening the power density profile. We also found that a prismatic HTGR with a uniform power density profile throughout the core has a greater safety margin than a PBR with the same design characteristics. However, when the power density profile is not flattened during the operation, the PBR with the linear power density profile has more safety margin than the prismatic HTGR with the same design parameters and with the power density profile by cosine and Bessel functions [1].

2. Study on small pebble bed reactor with accumulative fuel loading scheme

Innovative nuclear power plant designs and high-efficiency utilization of nuclear fuel are important issues in the field of nuclear power. Pebble bed reactors with an accumulative fuel loading scheme have been introduced to obtain high burnup and efficient uranium utilization. Monte Carlo codes, MVP/MVP-BURN, were used to perform the neutron transport and burnup calculation. Optimum fuel composition was obtained in the finite geometry using 6-g HM of uranium per pebble ball with 20% ^{235}U enrichment. The results show that the maximum burnup was 223 GWd/t with 10.2 years of operation. However, a large amount of excess reactivity occurred in the initial condition. One of the options for minimizing this was to reduce the enrichment of ^{235}U from 20% to 3.42%, only for the initial condition. The result showed a relatively small amount of excess reactivity during the operation period. However, the maximum burnup decreased to 199 GWd/t with 8 years of operation [2].

3. Study on pebble bed high temperature gas-cooled reactor with ROX fuel

The conceptual design of a small rock-like oxide fuel pebble bed reactor with once-though-then-out (OTTO) cycle is proposed here. TRISO-coated particles based on AGR-1 design were used to achieve a target burnup larger than 100 GWd/t-HM without any failure of spent fuel. In the first step, optimization of fuel composition was implemented by cell calculations. After that, whole core calculations were performed with and without movement of the fuel pebbles. With a heavy metal amount of 2 g per pebble and 20% uranium enrichment, the pebble bed reactor with OTTO cycle could achieve maximum burnup of about 145 GWd/t-HM and fissions per initial fissile atom (FIFA) of 75%. The results show that the core height can be reduced due to the fact that the impact of bottom core on burnup performance is insignificant. Also, the peak power density of the reactor exceeded the limit of that for the PBMR design. Therefore, subsequent optimizations of the core design were carried out by decreasing the core height and reactor power to reduce the construction cost as well as the peak power density. A reactor with 6-m core height and 120-MWth reactor power was ultimately determined as the optimal design for a pebble bed reactor with ROX fuel. This optimal design also has a negative temperature coefficient, and the peak power density was less than the limit of 10 W/cm^3 [3].

4. Study on CANDLE burning reactor with melt-refining process

The application of melt and refining procedures has demonstrated great potential to solve the fuel integrity problem in the high-burnup condition of CANDLE reactors. However, if the melt and refining procedures are applied during operation, the reactor might lose all the nuclide distribution in the fuel pins and CANDLE burning becomes impossible to achieve. In this study, the application of melt and refining was simulated in two cases to overcome the cladding limitation at 200 dpa. It became clear that if the number of axial regions for the melt and refining procedure is chosen properly, CANDLE burning is possible to achieve even if each region is homogenized by the procedure. In addition, the fission products released by the melt and refining procedure increase the burnup performance of the CANDLE core remarkably. It is also possible to improve the engineering design by reducing the

fuel volume fraction to a minimum at 48% [4].

5. Study on supercritical kinetic analysis with integral kinetic model for fuel debris

Preliminary prompt supercritical kinetic analyses in a simplified coupled system of fuel debris designed to roughly resemble a melted core of a nuclear reactor were performed using an integral kinetic model. The integral kinetic model, which can describe region- and time-dependent fission rate in a coupled system of arbitrary geometry, was used because the fuel debris system is weakly coupled in terms of neutronics. The results revealed some important characteristics of coupled systems, such as the coupling between debris regions and the effect of the coupling on the fission rate and released energy in each debris region during the simulated criticality accident. In brief, this study showed that the integral kinetic model can be applied to supercritical kinetic analysis in fuel debris systems and also that it can be a useful tool for investigating the effect of the coupling on consequences of a supercritical accident [5].

6. Measure to prevent criticality accidents in fuel debris removal

The drilling or cutting of resolidified fuel debris required to defuel the Fukushima Daiichi nuclear power station is certain to generate debris dust. This study focused on drilling resolidified fuel debris in water and conservatively confirmed by criticality calculations that neutron multiplication effect is higher if debris dust is suspended separately from the debris rather than if it is suspended closely around the debris. No use of vacuuming of debris dust, borated water, and active components was assumed in this study. Also, this study confirmed that the use of a debris dust guide effectively and passively limited the increase in neutron multiplication by debris dust because the guide distributes dust particles so flatly that sufficient neutron leakage limits neutron multiplication even if the volume fraction of the particles in water reaches the optimum condition. In the actual defueling operation at the nuclear power station, the use of a flatter debris dust guide will be more effective to prevent local recriticality concurrently with the careful control of the mass of debris dust. The physics and ideas in this paper should be applicable to other defueling technologies such as laser cutting as long as debris dust is generated and suspended in water [6].

7. Study on transient behavior in criticality accident of fuel solutions

A calculation code was developed for transient analysis of the total released energy in a criticality accident with two fuel-solution tanks. The calculation method was confirmed to be effective for transient analysis in a fuel-solution-tank system. The verification of the code was performed by comparing the calculation results with those of TRACY experiments. In the code, neutronic coupling between the tanks is treated. Using this code, transient analyses were performed for a two-tank system using different feedback models. The analyses confirmed that the total energy released in criticality accident with two fuel-solution tanks can be estimated using the knowledge of the total energy released in a single-fuel-solution-tank system [7].

Reference

1. Odmaa Sambuu, Toru Obara: Possible design of PBR for passive decay-heat removal; Journal of Nuclear Science and Technology; Vol. 53, No. 9, pp. 1296-1309 (2016).
2. Irwan Liapto Simanullang, Toru Obara: Improvement of core design of small pebble bed reactor with accumulative fuel loading scheme; Annals of Nuclear Energy, Vol. 94, pp. 87-92 (2016).
3. Hai Quan Ho, Toru Obara: Design concept for a small pebble bed reactor with ROX fuel; Annals of Nuclear Energy, Vol. 86, pp. 471-478 (2016).
4. Julia Abudul Karim, Jun Nishiyama,, Toru Obara: Application of melt and refining procedures in the CANDLE reactor concept; Annals of Nuclear Energy, Vol. 90, pp. 275-283 (2016).
5. Delgersaikhan Tuya, Toru Obara: Supercritical kinetic analysis in simplified system of fuel debris using integral kinetic model; Annals of Nuclear Energy, Vol. 91, pp. 59-64 (2016).
6. Hiroki Takezawa, Toru Obara: Passive measure for preventing recriticality of fuel debris dust for defueling at Fukushima Daiichi nuclear power station; Journal of Nuclear Science and Technology, Vol 53, No. 12, pp. 1960-1967 (2016).
7. Haruka Kikuchi, Toru Obara: Development of Transient Analysis Code for Estimation of Total Released Energy in a Two-Fuel-Solution-Tank System; Annals of Nuclear Energy, Vol. 87, pp. 486-493 (2016).

A.2 THERMAL CONDUCTIVITY ENHANCEMENT OF THERMOCHEMICAL ENERGY STORAGE MATERIAL FOR NUCLEAR ENERGY UTILIZATION

Yukitaka KATO

1. INTRODUCTION

For safety design of nuclear reactors for preventing severe accident, thermal energy management of the reactors is important. High-temperature waste heats are emitted from high-temperature industrial processes, internal combustion engines and co-generation systems. Solar heat systems generate high-temperature heats. Waste heats at over 200°C of 1.25×10^{18} J/y is emitted in Japan, that is, 40 % of total Industrial heat demand of 2.87×10^{18} J/y in it in 2004 [1]. Chemical heat pump (CHP) has potential to ease severe accident by temporal heat storage under lower pressure, and to utilize waste heats.

Waste heat recoveries from high-temperature processes are well developed for heat at over 400°C by steam and gas turbines, and also at less 100°C by sensible and latent heat storage technologies. On the other hand, medium-temperature heat at 200 ~ 400°C has not been utilized well. Efficient utilization of the medium-temperature heat would be one of important way for an improvement of energy efficiency of high-temperature processes. Amount of exhaust gas emission is quite large, and needed to utilize well for energy efficiency improvement of energy processes. For heat process in practical use, an influence of instable thermal operations on a reduction of total energy efficiency is not negligible. For solar heat system, cogeneration engine and so forth in practical use, a mismatch between heat output from heat source and heat demand generates plenty amount of waste heat. Then, waste heat storage function for medium-temperature heat becomes important. Thermochemical energy storage (TCES) has possibility to store medium-temperature heats. Magnesium oxide /water /magnesium hydroxide ($MgO/H_2O/Mg(OH)_2$) thermochemical energy storage is one of candidates [2].

$$MgO(s) + H_2O(g) \leftrightarrow Mg(OH)_2(s), \quad \Delta H° = -81.0\ \text{kJ mol}^{-1} \qquad (1)$$

TCES based on a MgO/H_2O reaction system are expected to find applications in waste heat utilization for cogeneration systems comprising gas and diesel engines, solar heat panels, and fuel cells. Although MgO material has high reactivity, thermal conductivity enhancement of the material is important for efficient heat exchange and thermal performance of the heat storage system because of low effective thermal conductivity of it. Expanded graphite (EG) is good candidate for thermal conductivity enhancer. $Mg(OH)_2$ composite material mixed with EG as named as EM was developed. Reaction performance enhancement of EM methodology was discussed in this study.

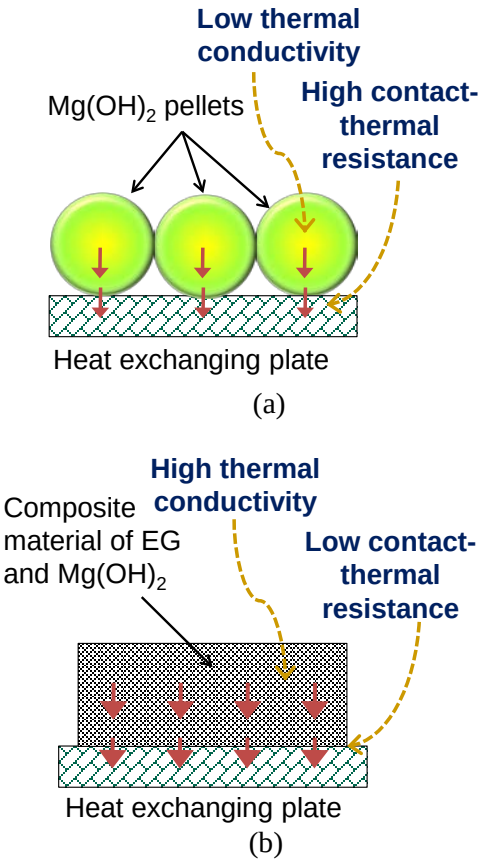

Fig. 1 Concept of thermal conductivity enhancement of a packed bed reactor for thermochemical energy storage performance: (a) Conventional heat exchange model between $Mg(OH)_2$ pellet and heat exchanging plate, (b) Improved heat exchange model between composite material of EG and $Mg(OH)_2$, and heat exchanging plate.

2. THERMAL CONDUCTIVITY ENHANCEMENT FOR TCES MATERIAL

Thermochemical heat storage material pellet using a pure-$Mg(OH)_2$ (MH-V05G, Ube Material, Japan, which was developed by Kato *et al.* [3]). In practical use of TCES system, the TCES material will be charged between heating fins in a heat exchanger type reactor. Fig. 1(a) shows heat exchange models of TCES for $Mg(OH)_2$ pellet. $Mg(OH)_2$ pellet has low-thermal conductivity around 0.2 W m^{-1} K^{-1},

and because the pellet has weak contact between heat exchanging plate surface because of cylindrical form, thermal conduct resistance at the surface is relatively high. Then the pellet is thought to have relatively lower thermal performance which is induced by the low-thermal conductivity.

Thermal conductivity enhancement of material and mold-ability for tight contact with heating fin are important for efficient heat exchange and thermal performance of the heat storage system. Then, expanded graphite (EG) as shown in Fig. 2(a) is good candidate for thermal conductivity enhancer. EG has high thermal conductivity, chemical stability and large void fraction. $Mg(OH)_2$ composite material mixed with EG as named as EM was developed as shown in Fig. 2(b) which is tablet figure. It was demonstrated that the EM composite had higher effective thermal conductivity and reactivity than pure-$Mg(OH)_2$ pellet [4]. EM has higher mold-ability, which means capability of forming easily random figure, in comparison with pure-$Mg(OH)_2$. Mold-ability is important character

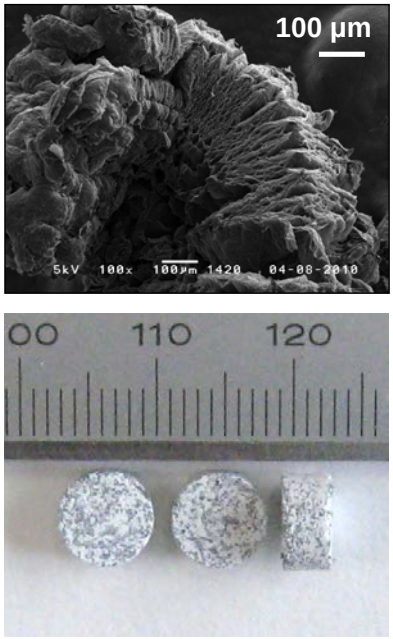

Fig. 2 Composite material of expanded graphite and $Mg(OH)_2$: (a) SEM image of expanded graphite (EG), (b) tablet form (ϕ 7 mm × h 3.5 mm) of the composite material (EM8).

for the thermochemical energy storage material, because the ability helps to have tight contact between material and heat exchanging surface and enhances thermal conduction between both, then was effective for practical reactor for the energy storage as shown in Fig. 1(b).

Apparent thermal conductivity of the packed bed, λ_{bed} [W $m^{-1} K^{-1}$] were measured using a quick thermal conductivity meter (QTM500, Kyoto Electronics). The pellets were arranged so that they completely covered the hot wire sensor of the meter. The thickness of the sample bed was 2 cm, which was the same as the thickness of the samples used for calibrating instrument. The density of the samples was the same as that in packed bed reactor experiment. Because the contact between the pellets and the hot wire sensor was random and not optimal, a single measurement would not give an accurate result. After the completion of each measurement, the hot wire sensor was lifted from the sample, and the pellets were rearranged to change the contact condition for the following measurement. Measurements were repeated 30 times, and the average of the 30 values was calculated. The averaged apparent thermal conductivities lbed are plotted in Fig. 3. This figure shows that lbed increased gradually with rmix from 16:1 (EM16), 8:1 (EM8) to 4:1(EM4). Compared with the original $Mg(OH)_2$ pellets, the λbed of EM4 was two times greater.

As shown in Fig. 1 (b), EM has low-thermal conduct resistance between plate and material because EM can form flat surface, and have enough contact with the plate surface, and high thermal conductivity of EM itself, then, the EM reactor is expected to have higher thermal performance than pellet bed [5].

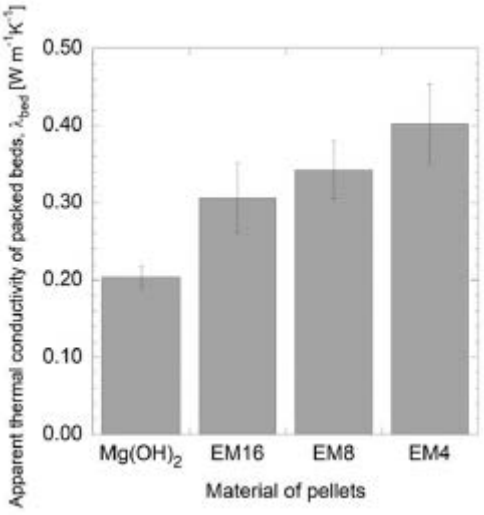

Fig. 3 Comparison of apparent thermal conductivities, λ_{bed}, of packed beds..

3. Conclusion

EM materials had higher thermal conductivity than pure-$Mg(OH)_2$ material. EM packed reactor bed indicated that heat could be transported rapidly. The temperature of the inner part of the bed rose faster because of the higher effective thermal conductivity of the EM bed. It was understood that the EM material was more practical material for a packed bed reactor having heat exchanger functions for thermochemical energy storage than $Mg(OH)_2$ pellets because of its high thermal conductivity and mold-ability. It was expected that material developments for thermochemical energy storage was key technology for efficient energy utilization of nuclear powers and waste heat recoveries.

References

[1] Energy Conservation Center of Japan (ECCJ), Nation wide waste gas heat at industrial sectors at temperature ranges in Japan, 2004, (2006) http://www.eccj.or.jp/diffusion/04/diff_07_09.html

[2] Kato, Y., Yamashita, N., Yoshizawa, Y., "Study of chemical heat pump with reaction system of magnesium oxide/water", *Kagaku Kogaku Ronbunshu*, 19, pp. 1213-1216, (1993).

[3] Kato, Y., Saito, T., Soga, T., Ryu, J., Yoshizawa, Y., "Durable Reaction Material Development for Magnesium Oxide/Water Chemical Heat Pump", *J. Chem. Eng. Japan*, 40(13), pp. 1264-1269 (2007).

[4] M. Zamengo, J. Ryu, Y. Kato," Numerical Analysis of Chemical Heat Storage Units for Waste Heat Recovery in Steel Making Processes", *ISIJ Int'l*, 55(2),pp. 473-482 (2015)

[5] M. Zamengom, Y. Kato, "Comparison of magnesium hydroxide/expanded Graphite composites for thermal energy storage in cogeneration nuclear power plants", *Energy Procedia*, 131, 119–126 (2017).

A.3 Dissolution behavior of core structure materials by molten corium in boiling water reactor plants during severe accidents

Yoshinao KOBAYASHI, Takehiro SUMITA

1. Introduction

A severe accident (SA) occurred at Fukushima Daiichi Nuclear Power Plant due to a great earthquake and subsequent tsunami which happened on March 11, 2011 in Japan. During the accident, the temperature of the reactor core rose up through the radioactive decay due to the loss of coolant in unit 1, 2 and 3. At such high temperature, the liquefaction occurs between core construction materials, such as B_4C (control rod) and stainless steel (SUS; control rod cladding) at 1477 K, and UO_2 (fuel rod) and Zircaloy (fuel clad) at 2170 K; it then forms liquid phases [1-3]. This liquid is called corium. The formed corium flows down to the bottom of the pressure vessel, and some portion reaches the bottom of the reactor container while dissolving the core support structure.

The collapse behavior of stainless steel which is the core supporting material should be well known to propose the access root for the debris removal because the residual core supporting material would be an obstacle when considering the access from upward. Two types of collapse behaviors can be considered regarding the attack by corium, one type of which might be formed by sequential melting of control rod and fuel rod and the other type of which might be formed by co-melting of control rod and fuel rod.

In this study, the former type has been taken up and the corium originated from control rod, which is molten metal of Fe-Cr-Ni-B-C system was considered in viewpoint of reaction with stainless steel. By immersion experiment of stainless rod into molten Fe-Cr-Ni-B-C alloy, the dissolution mechanism of stainless steel into this molten alloy has been discussed.

2. Experimental procedure

The alloy was prepared in a mullite crucible by melting a mixture of SUS 304 powder (18-20 % Cr, 8-11 % Ni, Mn < 2 %, Si < 1 %, Fe balance) and reagent grade of B4C powder at 1723 K for 90 min in Ar-3%H2 atmosphere, followed by water quenching. This mock corium was synthesized to have the B concentration of 3.71 mass percent; this is similar to the Fe – B eutectic composition[7] having 5 mass percent of B concentration. Samples simulating structural material of SUS 304 were prepared by machining SUS 304 rods designed to have the shape of immersion parts with the length of 50 mm and diameter of 7 mm. About 14 g of mock corium sample (Fe-Cr-Ni-B-C alloy) was placed in a mullite crucible of and was placed in an electric furnace. Figure 1 shows the schematic illustration of the experimental apparatus. The sample was pre-melted at 1573 K in an Ar atmosphere for 45 min. After that, the rod sample was charged into the furnace just above the crucible, and preheated for 2 min. Thereafter, the rod sample was immersed in molten metal for the intended time ranging from 22 to 660 s. The rod was taken out of the furnace together with the crucible, and was water quenched immediately. The sample was cut to observe the cross section, followed by grounding with abrasive SiC papers (#100 - #2000) and polishing with diamond paste (2 μm). Digital microscope and Scanning Electron Microscope (SEM) were used to observe the morphology, and Energy Dispersive X-ray Spectroscopy (EDS) and Wavelength Dispersive X-ray Spectroscopy (WDS) were used to perform element analysis to characterize the reaction zone.

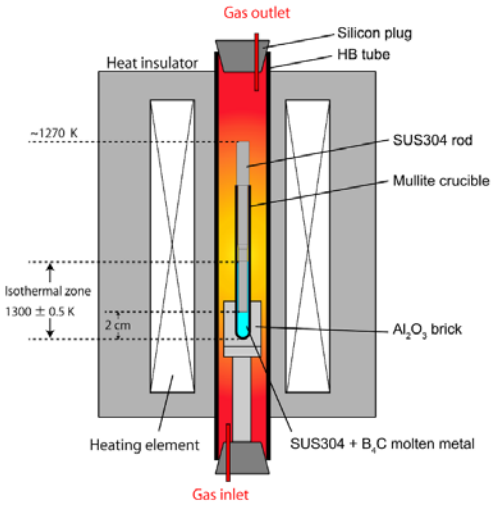

Figure 1. Schematic illustration of experimental apparatus.

3. Results and discussion

Figure 2 shows the schematic illustration, Optical Microscopic Images (OMI), and Backscattering Electron Images (BEI) of the sample after 4 min immersion experiment. Figure 3 shows the results of high magnification BEI and EDS point analysis with high magnification near the solid and liquid interface after 2 min immersion experiment. It was confirmed that molten metal infiltrated into the austenitic grain boundaries in BEI. This suggests that grains may fall off from the rod due to infiltration. Thus, it is predicted that, besides chemical dissolution reaction between Fe and B, physical dissolution is caused by the grains falling off from rod due to infiltration of molten metal. Among the two kinds of the dissolution modes, chemical dissolution rate of liquid phase formation reaction between Fe and B was taken up and examined. The apparent diffusion coefficient of B was estimated and evaluated with assumption that the diffusion of B in liquid phase is the rate-determining step of chemical dissolution. Concentration gradient from the liquid phase saturated with the solid phase element to the liquid phase bulk is considered. In this experiment,

however, it is found that the liquid phase infiltrates the grain boundary and causes the physical dissolution, and the detached grains are further dissolved and diffused in the liquid. In order to predict which dissolution mode is faster, kinetic analysis based on general unsteady diffusion equation was performed, leading to the apparent diffusion coefficient. On the basis of the solution of Fick's second law, the apparent diffusivity of B has been evaluated according to the concentration profile of B as shown in Fig.4 which was converted into the relationship between two parameters described in the axis in Fig.5 where the slope of this linearity corresponds to diffusivity. Figure 6 shows the relationship between diffusivity and holding time. Theoretically, diffusivity should not have the time dependency; however, through the mechanism stated above, the diffusivity appears to change along with time which should be called "apparent diffusivity". As proved by this time dependency, physical dissolution is predominant in this collapse phenomenon through the mechanism that B containing alloy infiltrates into the grain boundary inducing the eutectic melting and the grain detaches from the surface of the stainless steel. Further investigation would be necessary for the clarification of the effect of various factors to this physical dissolution phenomenon.

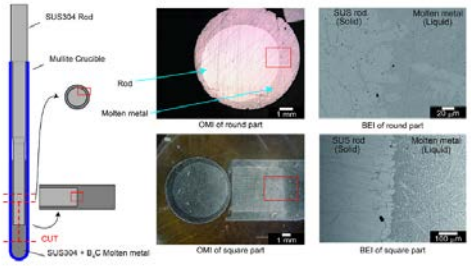

Figure 2. Schematic illustration, OMI, and BEI of sample after 4 min experiment.

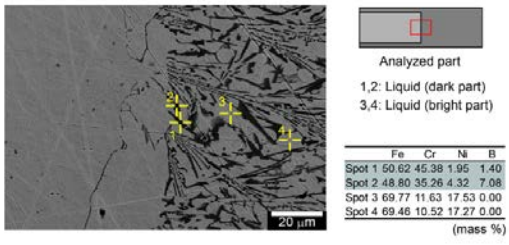

Figure 3. BEI and result of EDS point analysis in vertical cross section after 4 min experiment.

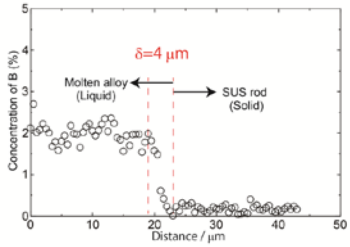

Figure 4. Concentration profile of B.

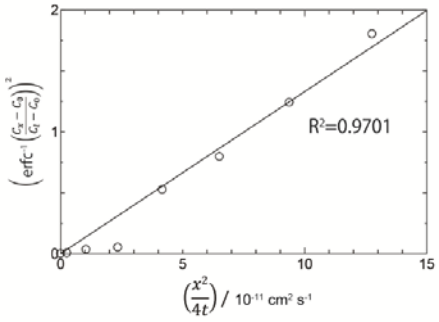

Figure 5. Estimation of apparent diffusion coefficient of B.

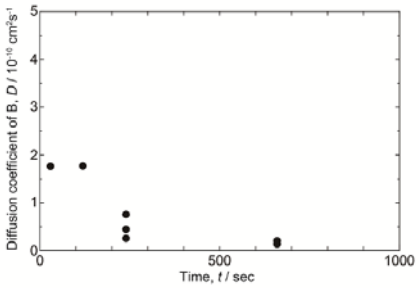

Figure 6. Apparent diffusion coefficient of B in molten Fe–Cr–Ni–B–C alloy.

4. Conclusions

Regarding the collapse mechanism of stainless rod by the attack of Fe-Cr-Ni-B-C alloy during SA in FDNPP, there are two types of dissolution mode in this system: (1) chemical dissolution by eutectic reaction between Fe and B and (2) physical dissolution caused by the grains falling off from rod due to infiltration of molten metal. The apparent diffusion coefficient was estimated and was on the order of 10^{-11} cm^2/s. It is considered that the chemical dissolution in this system was slow, therefore, physical dissolution caused by grain detachment would be predominant mechanism.

Acknowledgment

This work was financially supported by the project of "Accessibility for removal of fuel debris in BWR plant after severe accident" in The Center of World Intelligence Project for Nuclear S&T and Human Resource Development, Ministry of Education, Culture, Sports, Science and Technology.

Reference

[1] Tanaka S.: Proc. Jpn. Acad. 2012; 88:471-484.
[2] Washiya: International symposium on the decommissioning of TEPCO's Fukushima Daiichi Nuclear Power Plant Unit 1-4 [Internet];2012 March 14; Tokyo (Japan). Available from: http://www.meti.go.jp/english/earthquake/nuclear/decommissioning/pdf/20120315_01_014.pdf.
[3] Nagase F.: Journal of the Atomic Energy Society of Japan. 2014; 56:235-239.
[4] SGTE alloy database. B-Fe system. 2004.

A.4 Progress of Neutron Capture Measurements at Tokyo Institute of Technology

Masayuki IGASHIRA, Tatsuya KATABUCHI, Tatsuhiro SAITO,
Seigo UMEZAWA, Karin TAKEBE, Ryo FUJIOKA

1. Introduction

In 2016 fiscal year, our research group worked on three topics:

1. Neutron capture cross section measurement on Re isotopes
2. Angular distribution of gamma-ray emission from the ^{7}Li(p,p')^{7}Li and ^{7}Li(p,γ)^{8}Be reactions
3. Neutron capture cross section of ^{99}Tc

Experiments for the first two topics were performed in the Tokyo Tech. Measurements for the last topic were made in the Japan Proton Accelerator Research Complex (J-PARC) in the Japan Atomic Energy Agency.

2. Tokyo Tech

2.1. Rhenium isotopes

We measured the neutron capture cross section and the neutron capture γ-ray spectrum of ^{185}Re and ^{187}Re by both the time-of-flight (TOF) and activation methods in the keV neutron energy region. This experiment was motivated by a Re/Os nucleo-cosmochronometer, which has been proposed to date a rapid neutron-capture process (r-process) in nucleosynthesis. Rhenium-187 is primarily considered a pure r-process nuclide and has a long half-life of 43.5 Gyr. Thus, the ^{187}Re/^{187}Os abundance ratio changing with the ^{187}Re half-life can be a good chronometer for the r-process. However, slow neutron-capture process (s-process) through an isomer state of ^{186}Re ($T_{1/2}$ = 0.2 Myr) may contaminate the ^{187}Re/^{187}Os abundance ratio. It is necessary to evaluate a contribution from ^{186m}Re created from the ^{185}Re(n,γ)^{186m}Re reaction. In this work, we experimentally determined the total capture cross section of ^{185}Re by the TOF method, and the partial capture cross section leading to the ground state of ^{186}Re by the activation method. Experiments were performed at the Laboratory for Advanced Nuclear Energy at the Tokyo Institute of Technology. Incident neutrons were generated through the ^{7}Li(p,n)^{7}Be reaction by a pulsed proton beam from a Pelletron accelerator bombarding a lithium target. The incident neutron energy distributed from a few keV to 100 keV, determined by the TOF method. Capture gamma rays from the sample were detected with an anti-Compton NaI(Tl) spectrometer in the TOF experiments. The (n,γ) cross sections were obtained from the pulse height spectra by the pulse-height weighting technique. In the activation experiments, decay gamma-rays after neutron irradiation were measured with a HP Ge detector well shielded from natural background gamma-rays. We reported the preliminary results in the 16th International Symposium on Capture Gamma-ray Spectroscopy (CGS16) [1].

2.2. Angular distribution of gamma-ray emission from the ^{7}Li(p,p')^{7}Li and ^{7}Li(p,γ)^{8}Be reactions

This research was motivated by a medical application of neutron science, i.e. boron neutron capture therapy (BNCT). BNCT uses high LET particles from the ^{10}B(n,α)^{7}Li reaction to terminate cancer cells. Neutron sources for BNCT has been nuclear reactors since the beginning of the history but accelerator neutron sources are emerging for the next generation of BNCT. Accelerator-based BNCT can overcome limits the current BNCT has, for example, strict regulation associated with nuclear reactors or public acceptance to implement BNCT in city areas. To achieve the technological requirements, several types of BNCT accelerators have been suggested. In the suggested ideas, the ^{7}Li(p,n)^{7}Be reaction is one candidate neutron production reaction. The ^{7}Li(p,n)^{7}Be reaction requires low proton energy, thus leading to a compact accelerator system. However there is one concern to deploy ^{7}Li(p,n)^{7}Be neutron sources for the medical application. When a lithium target is bombarded with a proton beam, not only neutron production reaction ^{7}Li(p,n)^{7}Be but also γ-ray production reactions, ^{7}Li(p,p')^{7}Li* and ^{7}Li(p,γ)^{8}Be, occur. The γ-ray production rate is high and the γ-ray energy distributes up to around 18 MeV. This γ-rays from a p-Li neutron source introduce undesired radiation dose to a patient. To estimate absorbed dose by the γ-rays, γ-ray nuclear data such as γ-ray production yield and γ-ray spectrum, are necessary. In 2015, we measured the γ-ray spectrum from a p-Li neutron source and derived γ-ray production yields of the ^{7}Li(p,p')^{7}Li* and ^{7}Li(p,γ)^{8}Be reactions. The results were reported in Ref. [2]. In the present work, we measured the angular distribution of γ-rays from the ^{7}Li(p,p')^{7}Li and ^{7}Li(p,γ)^{8}Be reactions

Experiments were performed in the Tokyo Institute of Technology. A Li target on a Cu backing was irradiated with a proton beam from a Pelletron accelerator. The thickness of the Li target was 0.3 mm, thick enough for the proton to stop in the Li layer. Gamma-rays from the neutron source were detected with a NaI(Tl) detector, changing the detection angle from 0° to 125° with respect to the beam axis. After background subtraction, the γ-ray spectrum was derived by unfolding the obtained pulse-height spectrum with detector response functions.

3. J-PARC

3.1. Technetium-99

We measured the neutron capture cross section of ^{99}Tc at J-PARC. Technetium-99 is a long-lived fission product

(LLFP) produced in spent nuclear fuel. Long-term nuclear waste management is a debatable issue due to LLFP and long-lived minor actinides. One proposed solution is the nuclear transmutation, in which LLFP nuclides are transmuted into stable or short-lived isotopes via the neutron-induced nuclear reaction. Technetium-99 is high priority for transmutation because the cumulative fission yield and the radio toxicity are very high. To design a nuclear transmutation system, reliable nuclear data of ^{99}Tc are required. Thus, we conducted measurement of the nuclear capture cross section of ^{99}Tc.

A TOF spectrum of neutron capture events of ^{99}Tc was measured using the Accurate Neutron Nucleus Reaction Measurement Instrument (ANNRI) at J-PARC. The sample of ^{99}Tc was placed at a flight distance of 27.9 m from the spallation neutron source. Capture γ-rays from the sample were detected with an NaI(Tl) detector placed at a scattering angle of 90° with respect to the beam axis. The neutron capture cross section of ^{99}Tc was determined from the thermal to keV energy region. In paticular, effort has been made to measure the cross section in the high energy region. The results were reported in Ref. [3].

Reference

1. T. Katabuchi, K. Takebe *et al*., Neutron capture cross section of ^{185}Re leading to ground and isomer states of ^{186}Re in the keV-neutron energy region, 16th International Symposium on Capture Gamma-Ray Spectroscopy and Related Topics (CGS16), Shanghai, China, 18-22 September 2017.
2. T. Saito, T. Katabuchi *et al*., Journal of Nuclear Science and Technology, **54**, pp. 253-259 (2017).
3. T. Katabuchi *et al.*, Measurement of the neutron capture cross section of ^{99}Tc using ANNRI at J-PARC, EPJ Web of Conference, **146**, 11050 (2017), Proceedings of the International Conference on Nuclear Data for Science and Technology (ND2016), Bruges, Belgium, 11-16 September 2016.

A.5 Velocity Profile Measurement on Turbulent Swirling Flow by Ultrasound Techniques

Hiroshige KIKURA, Ari HAMDANI

1. Introduction

Velocity profile measurement of fluid flow in a complex flow is specific because of flow conditions and its parameter have to be to calculate the efficiency of the power plant. In this report, the fluid velocity profile is measured in the swirling flow condition.

2. Experimental Setup

We made the rotary type swirling generator, and it was installed at 32D (D=50mm) from an inlet at the position of fully developed region in a circular water flowing system. The measurement position was located 7D downstream of the swirling generator. Two ultrasonic measurement systems were used; UVP-Duo (for one-dimensional velocity) and Phased Array UVP (for two-dimensional velocity).

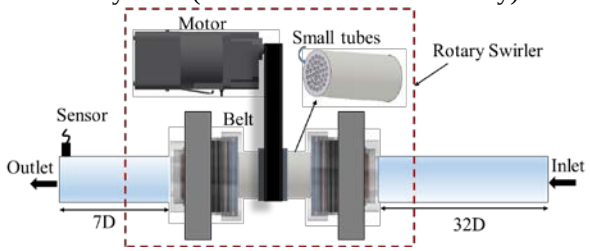

Fig. 1 Rotary type swirling generator and test section.

3. Result and discussions

3.1. One-dimensional Velocity Profile Measurements

One-dimensional velocity profile in the different swirling intensities (S) is shown in Fig. (1). Swirl number is defined by the ratio of radial momentum flux to axial momentum flux as shown in Eq (1).

$$S = 2\pi\rho\int_0^R r^2\bar{u}_z\bar{u}_\theta dr \Big/ 2\pi\int_0^R r\bar{u}_z^2 \quad \text{(or)} \quad S = \frac{\omega D}{2U_m} \qquad (1)$$

where, r is radial distance from a pipe radius (R), u_z is streamwise mean velocity, and u_θ is circumferential mean velocity. Moreover, the swirl intensity can be calculated from the angular velocity ω of rotary pipe, diameter of pipe D and mean velocity U_m of the fluid.

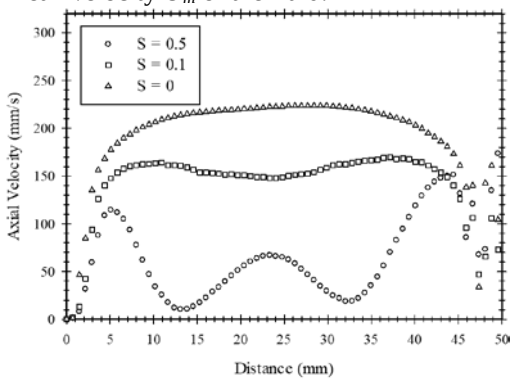

Fig. 2 One-dimensional velocity profile of swirling flow.

The axial mean velocity profile in the pipe center is decreasing by increasing the swirling number.

3.2. Two-dimensional Velocity Profile Measurements

Phased Array UVP system is applied to measure two-dimensional velocity profile. Phased array sensor can measure multi-dimensional and multi-measurement lines. Three measurement lines (with incident angle 10˚, 0˚ and -10˚) plot two-dimensional velocity profile of the fluid in the swirling intensities (S = 0.5). Fig. (3) and Fig. (4) show the axial and tangential mean velocity vector of the swirling flow in a straight pipe.

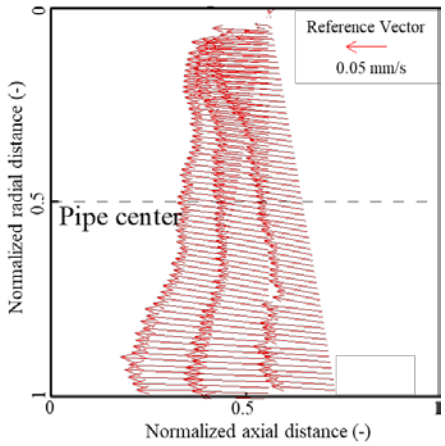

Fig. 3 Axial mean velocity vector of swirling flow.

Two-dimensional axial and tangential mean velocity can be measured, and the swirling core is observed at the pipe center in the tangential velocity measurement.

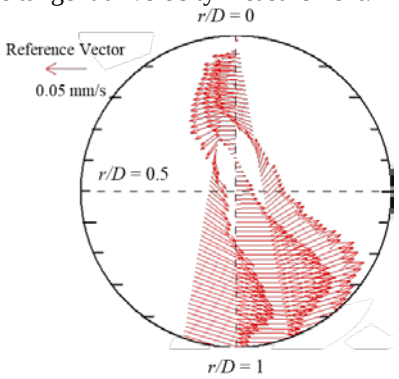

Fig. 4 Tangential mean velocity vector of swirling flow.

4. Conclusion

In conclusion, Ultrasound techniques can be applied in a turbulent swirling flow condition.

Reference

1. S. Shwin, H.Kikura *et al.*; AESJ, Young Researcher Forum, Poster Session, 30 March 2017, Tokai University, Tokyo, Japan.

A.6 Low Velocity UVP Measurement on Joule-Heating Flow

Hiroshige KIKURA

1. Introduction

High-level radioactive waste (HLW) is already produced in all over the world as a waste from nuclear power plants, and the method to reprocess HLW becomes an important issue to solve. In Japan, Liquid Fed Ceramic Melter (LFCM) type glass melter is being developed for the reprocessing. The glass melter applies Joule-heating to generate molten glass, and the melter can mix HLLW and molten glass by convective flow mainly induced by Joule-heating. These volumetric heating in lower part and cooled in the upper part make continuous chaotic flow behavior, named as 'chaotic steady state.' In a cavity which has similar shape to the real glass melter, a non-flow area can be observed by 2-D visualization, the flow in this area was very slow. As the velocity resolution of the former UVP method is not enough, the flow in the bottom of the cavity is difficult to measure. Hence, a new UVP method named phase difference method for very low velocity field was developed. However, the Joule-heating flow is affected by thermal field, electromagnet field and flow field. These three field lead flow is completed and the echo of ultrasound signal is difficult to receive. In this paper, phase difference method was tried to apply in the Joule-heating flow and compare with previous study.

2. Experiment Apparatus

In this experiment, the work fluid was 80wt% glycerin-water solution, and 0.5wt% LiCl was added into the fluid to lead fluid possess the conductivity. After the glycerin- water solution mixed, nylon powder was added into the fluid as a reflected powder.

The initial temperature of the fluid was also 20°C. Cooling temperature of the top surface was 20°C as the room temperature by using copper heat sinks and a water circulator at top surface. The electrodes side was adiabatic condition. In the experiment, AC power was applied in the experiment to generate Joule-heating. UVP transducer was set at the bottom of the cavity.

3. Verification of Phase Difference Method

The flow profile in the cubic cavity was measured by phase difference method and compare with the time repetition method. The flow behavior in the center line of cubic cavity measured by phase difference method is shown as the Fig. 1(a), and the Fig. 1(b) shows the data was measured by the time repetition method. The similar chaotic flow can be observed in almost whole of the cavity. The chaotic flow occurred almost in the whole cavity. However, in the phase difference method, the flow in the bottom parts is complete and difficult to analyze.

It can be find that flow measurement was not start at 0mm position, the noise observed by the phase difference method was the echo from wall. However, in the cavity, the echo of ultrasound signal from reflect powder can be recognized well, the chaotic Joule-heating flow was observed by the phase difference method clearly. Therefore, the phase difference method can be applied for the Joule-heating flow measurement.

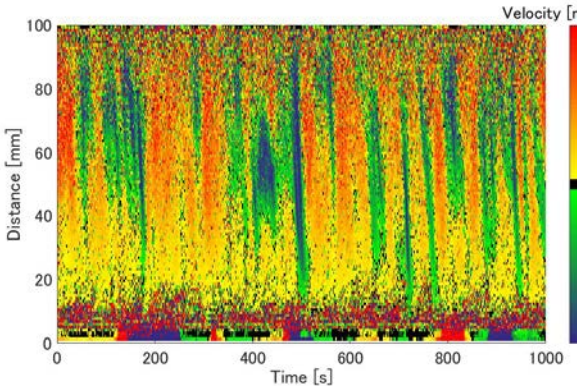

(a) Phase difference method

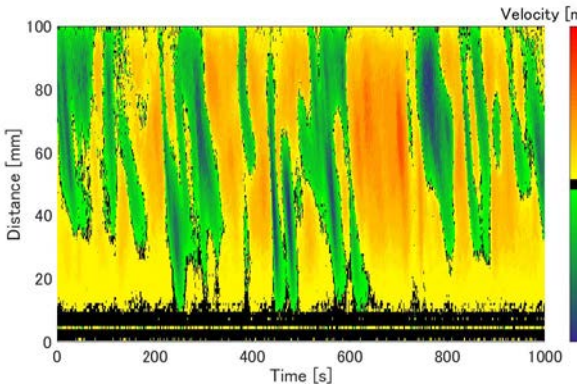

(b) Conventional method

Figure 1: Flow behavior at the center line.

4. Conclusion

A new UVP measurement method, phase difference method was developed for low velocity measurement. The new UVP system can be applied in the Joule-heating flow. When the repetition number of high, few reflect powder field is difficult to measure. However, the velocity profile can be observed by the average data. In addition, If the reflect powder can keep in a high mount, the low flow field can be measured.

Reference

1. J. Zhou, H.Kikura *et al.*;11th International Conference on Advances in Fluid Mechanics, 2016, Ancona, Italy, 127-138.
2. J. Zhou, H.Kikura *et al.*:10th International Symposium on Ultrasonic Doppler Methods for Fluid Mechanics and Fluid Engineering (ISUD10), 2016, Tokyo, Japan, 89-92.

A.7 Tracking Technique for Ultrasonic Measurement of Bubbles

Hiroshige KIKURA

1. Introduction

Bubbly two-phase flows appear in reactor cores as well as in suppression pools of BWRs. Bubbles are often measured by a high-speed camera (HSC), which has certain limitations such as a need for an optical access. The ultrasound can overcome these limitations and complement HSC to obtain good understanding of the bubble behaviour.

Ultrasonic Reflector Recognition and Tracking Technique (URRTT) detects the trajectory of bubble's surface [1] and use it to measure the bubble velocity or diameter. The reliability and accuracy of the URRTT was improved and the measurement capabilities were improved [2,3,4] by introducing a semi-online measuring system.

2. Experimental settings

The experimental apparatus is shown in Fig. 1. Air bubbles entered the water box through a bubble positioner, which forced all bubbles into a narrow measurement volume. There was a HSC in front the water box as a reference measurement.

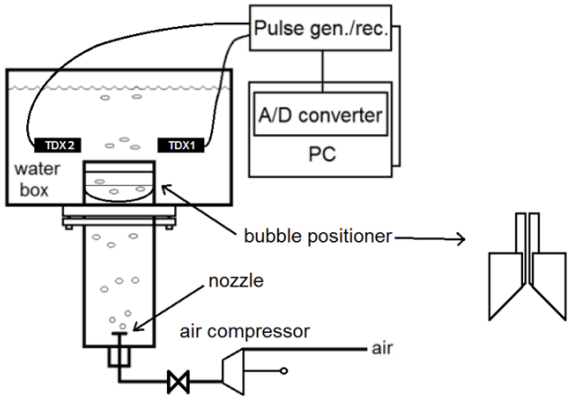

Fig. 1 Experimental apparatus: a) side view, b) top view, c) side view of the bubble positioner

3. URRTT principle

3.1. Reflector recognition

Ultrasonic transducer (TDX) emitted pulses. The reflection from bubble was detected by the TDX with certain delay dependent on the TDX-bubble distance. Signal processing used intensity and cross-correlation with an expected signal to get a precise delay. The dependency of bubble position on signal delay was calibrated using reflections from known positions to improve the accuracy. The whole reflector recognition process run online and produced points (detected bubbles) with time, position and the signal strength. The online measurement allowed to measure over extremely long periods of time.

3.2. Reflector tracking

A clustering type algorithm tracked points and divided them to trajectories. The algorithm searched in cycles for the closest pair of trajectories (using their times and positions). However, this approach sometimes connected two close trajectories into one. The signal strength is analysed as well to treat this. A similar approach was used to associate final trajectories with those from HSC.

4. Results and conclusions

The error rate of the trajectory detection improved from 30.7% to 3.7%. The accuracy has improved as shown in Fig. 2 and Fig. 3, where normalised bubble size error was the bubble-averaged difference between bubble sizes measured by URRTT and HSC.

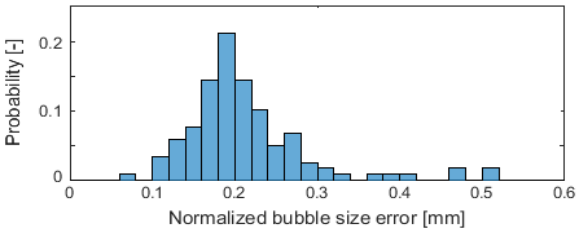

Fig. 2 Bubble size error distribution (older)

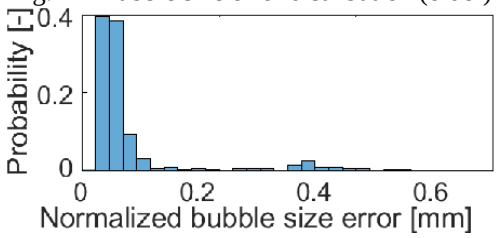

Fig. 3 Bubble size error distribution (newest)

The URRTT was improved as documented above. In the future, the URRTT performance will be tested for various conditions of the bubbly flow. The performance should deteriorate with higher void fraction and it is important to know the void fraction limit.

Reference

1. A.Povolny, H.Kikura *et al.*: International Conference on Multiphase Flow 2016, Firenze, Italy, ICMF2016-628.
2. A.Povolny, H.Kikura *et al.*: 24th International Conference on Nuclear Engineering (ICONE24), 2016, Charlotte, USA.
3. A.Povolny, H.Kikura *et al.*: 10th International Symposium on Ultrasonic Doppler Methods for Fluid Mechanics and Fluid Engineering (ISUD10), 2016, Tokyo, Japan.
4. A.Povolny, H.Kikura *et al.*: 11th Intl. Topical Meeting on Nuclear Thermal-Hydraulics, Operation and Safety (NUTHOS-11), 2016, Gyeongju, Korea, N11A0200.

A.8 Measurement of Subcooled Boiling Flow using Ultrasonic Technique

Hiroshige KIKURA

1. Introduction

Subcooled flow boiling is important in many industrial and engineering application. Bubble characteristics in subcooled flow depend on many conditions, such as pressure, flow rate, temperature, etc. Improve understanding of subcooled boiling flow may very helpful for safety analysis of thermal hydraulic systems.

There are some experimental investigations of subcooled boiling flow, however, mainly using the optical visualization method. For the ultrasonic technique, in the previous study, T.T. Nguyen measured bubble condensation rate in subcooled liquid column which the flow rate of water is assumed as zero. In this study, UVP method is applied to measure the condensation rate and velocity of vapor bubbles rising in subcooled water flow. The condensation rate and the rising velocity of the bubbles are two of important parameters because they use to calculate the heat transfer coefficient which is used in the models of numerical simulations of condensing two-phase flow.

2. Measurement method

The condensation rate is defined as the rate of change in diameter of bubbles: dD_b/dt. Consider a bubble rising in subcooled boiling flow as shown in Fig.1. Two transducer TDX1 and TDX2 were set up at angle of ±45° parallel with the pipe. The measured velocities of two transducers V_{TDX1} and V_{TDX2} should include component of the bubble rising velocity and the condensation rate:

$$V_{TDX1} = v_b cos\theta - v_c; \quad V_{TDX2} = v_b cos\theta + v_c \qquad (1)$$

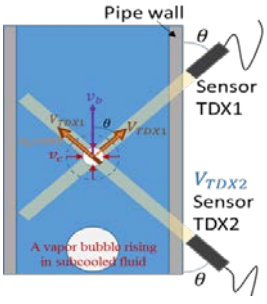

Fig. 1. Principle for measurement of condensation rate using UVP method.

From Eqs.1 the condensation rate and rising velocity of bubble can be calculated as:

$$v_c = \frac{V_{TDX2} - V_{TDX1}}{2}; \qquad v_b = \frac{V_{TDX2} + V_{TDX1}}{2cos\theta} \qquad (2)$$

For multi-bubbles measurement, the average condensation rate and average rising velocity of bubbles are calculated using average velocities:

$$\overline{v_c} = \frac{\overline{V_{TDX2}} - \overline{V_{TDX1}}}{2}; \qquad \overline{v_b} = \frac{\overline{V_{TDX2}} + \overline{V_{TDX1}}}{2cos\theta} \qquad (3)$$

3. Measurement results

3.1. Measurement of air-bubbly flow

For confirmation of the method, the measurements were conducted with the adiabatic air-water bubbly flow. Because that the air bubbles in this measurement were not collapsed during transport in the flow, the condensation rate, in this case, should be zero. Fig. 2 shows the velocity profiles which measured by two transducers. Two velocity profiles are mainly identical. The calculated condensation rate for this case by applying the Eq. 3 is almost zero.

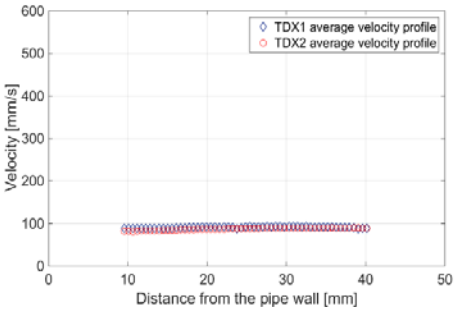

Fig. 2. Velocity profile of air bubbles.

3.2. Measurement of condensing bubbles in subcooled flow

Fig. 3 shows the velocity profiles which were measured by two transducers for vapor bubbles in the subcooled liquid flow. The subcooling temperature, in this case, is 5.6°C, and the average velocity of subcooled water is 6.3 mm/s. The difference in velocity profiles of two transducers, in this case, is caused by the collapse of the vapor bubbles. By using Eqs. 3, the average condensation rate was calculated as 19.5 mm/s, and the average rising velocity is 258.0 mm/s.

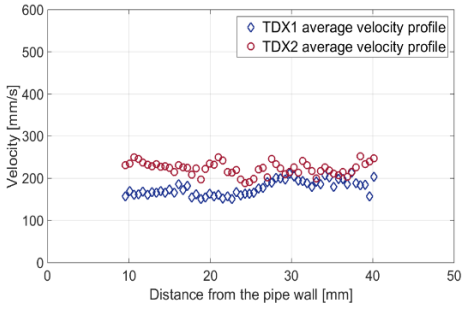

Fig. 3. Velocity profile of vapor bubbles in the subcooled boiling flow.

4. Conclusions

It has been confirmed that the development system is capable of measuring velocity in the subcooled boiling flow. In this test, the condensation rate and the average velocity of bubbles were calculated.

Reference

T.V.Tran, H.Kikura *et al.*: 15th Wakate Kenkyuusha Happyo Touronkai, AESJ Kantoukouetsu-Branch, 2016, Tokyo, Japan, A-2.

A.9 Remote System with Phased Array Ultrasound Velocity Profiler Method for Flow Measurement

Hiroshige KIKURA

1. Introduction

One of the essential issues in Fukushima Dai-ichi nuclear power plants unit 1 to 3 is groundwater contamination due to water leakage from damaged primary containment vessels (PCVs). In order to stop the leak, detections of these leakages are required. However, because the reactors are the highly-dosed environment, telemetry systems with robots are applied to the detection of the leakages. When the telemetry measurement is conducted, an integration of a robot and measurement techniques are demanded. Optical measurements have not detected the leakage points due to poor visibility in turbid water in PCVs. As a measurement method which can meet demands in the environment of PCVs, a phased array ultrasonic velocity profiler (UVP) method is proposed. The phased array UVP method can measure 2-D velocity map of flow in cloudy water, and the leakage point is determined from the flow map. A basic telemetry system using a robot and the phased array UVP method was developed, and the robot positioned the sensor[1]. The technique of remote detection of the leakage point based on the flow map of the poured water in PCV was proposed. In this research, we measured flow map using robot arm with three degrees of freedom linkage mechanism as the basic stage of development.

2. Basic remote flow measurement system

As a basic telemetry system, a robot arm with three degrees of freedom was developed, because the three-dimensional measurement can be achieved with two-dimensional phased array measurement. A photograph of the robot arm is shown in Fig. 1. The robotic arm is driven by the wire tension, which is Tendon driven multi-joint manipulate. The advantage of this robotic arm is lightweight that contributes saving the output of motors. Therefore, the robotic arm was compact and has enough output for transporting phased array sensor. The position of array sensor was controlled by a motor driver (EPOS2 24/5, MAXSON) using a DC motor (RE25 ϕ25 24V 20W, MAXSON). The place of phased array sensor is calculated from the rotary encoder attached to the DC motor.

For the demonstration of the phased array flow measurement using the robotic transportation, water flow into a leakage hole was measured. The experiment apparatus and condition were same as previous experiments. The phased array sensor was placed at a position 60 mm from the front side face of the outlet and 80 mm from the bottom face by controlling the robotic arm. Moreover, the phased array UVP measurement was performed at the place. The measurement result is shown Fig. 2. Flow towards the leakage hole can be observed in the region where the height is above 30 mm. Accordingly, the possibility of the remote measurement system using the robot arm was confirmed.

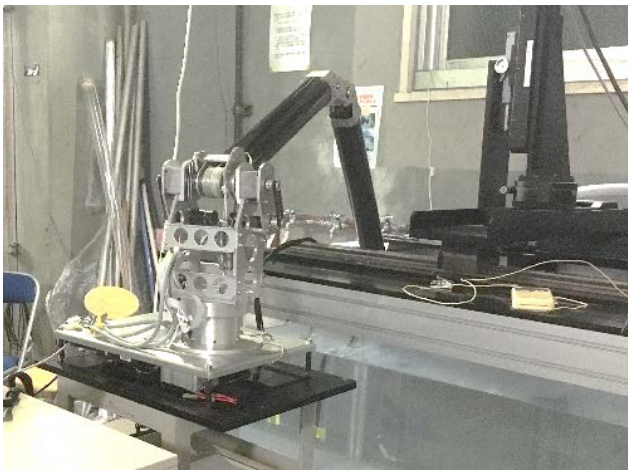

Fig. 1 Robot arm under the measurement.

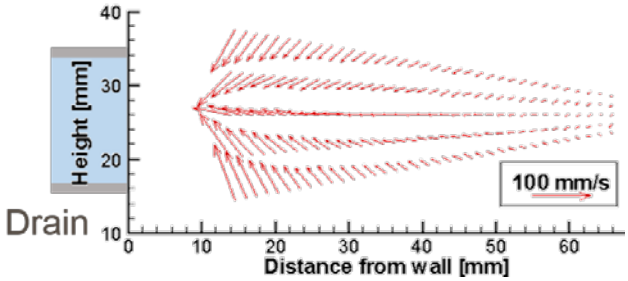

Fig. 2 Flow measurement of the phased array UVP method using the robot arm.

3. Conclusion

The possibility of measuring 2-D velocity map with the developed telemetry system of flow near the leakage point was verified. Consequently, the basic remote system for the detection of the leakage was established.

Acknowledgment

A part of this study is the result of “An ultrasonic measurement system and its robotic deployment into vessels for the combined assessment of debris condition and water leakage” carried out under the Center of World Intelligence Project for Nuclear S&T and Human Resource Development by the Ministry of Education, Culture, Sports, Science and Technology of Japan.

Reference

1. R. Nishiwaki, H. Kikura *et al.*: Fundamental study of telemetry system with phased array ultrasonic velocity profiler method for flow measurement; 25th International Conference on Nuclear Engineering (ICONE25), 2016, Shanghai, China, ICONE25-68010.

A.10 Study of an Ultrasonic Measurement System and its Robotic Deployment into Vessels for the Combined Assessment of Debris Condition and Water Leakage

Hiroshige KIKURA, Ari HAMDANI

1. Introduction

In 2011 the severe accident occurred at Fukushima Dai-ichi NPP which caused by the huge earthquake and massive tsunami afterward. Consequently, a damaged structure was found in Primary Containment Vessel (PCV) and Reactor Pressure Vessel (RPV). Furthermore, this event leads water cooling leakage to the groundwater and melted fuel felt down to the PCV and little fuel has left in RPV. Retrieval of the fuel debris is the primary requirement for the ending of the accident and regaining of Fukushima NPP. The way toward retrieval of fuel debris is, however, long and tough. Retrieval of the fuel debris, especially in unit 1, 2 and 3, is the primary requirement for the ending of the accident. In mid-and-long-term decommissioning roadmap by TEPCO, first of all, the location, the shape, and also the properties of debris have to be investigated. As recent work on the decommission, inspection inside the PCV has been conducted using the robot and video camera. However, the inspection seems to be though due to the highly radioactive environment and water turbidity.

Therefore, for decommissioning purpose, we proposed a measurement method for determining a water leakage location and the shape of fuel debris by an ultrasonic method that is also integrated with a robot. The ultrasonic inspection was utilized due to its to be applicable in an opaque fluid and has high resistance to radioactivity.

2. Measurement method and results

2.1. Aperture synthesis method for fuel debris inspection

For determining fuel debris distribution, we focused on aperture synthesis method. This method can achieve high signal-noise ratio by taking advantage of multi-receiving at each transmitting (see **Fig. 1**). This means that in the case of target surface has angle against the transmitted beam, the method can capture significant echo signal from the target surface and allow precise detection. Since echo intensity varies according to the shape of the target, detailed shape of the target can be reproduced by synthesis of the received signals. The spatial intensity at the measurement point $S_p(x)$ is defined as follow.

$$S_p(x) = \sum_{(i,j)\in P} u_{ij}(t_i(x) + t_j(x)) \qquad (1)$$

where i, j is transmitting and receiving element in linear array sensor, $u_{ij}(t)$ is waveform as a function of time, t_i is transit time from transmitting element to the measurement point along with measurement line, and t_j is transit time from the measurement point to receiving element.

Figure 2 shows measurement setup and result of the reconstructed image using aperture synthesis method. It can be seen in Fig. 2. (b) that aperture synthesis method successfully visualizes the surface of imitated fuel debris.

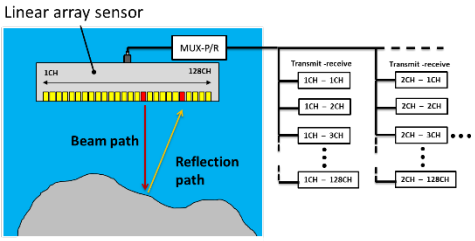

Fig. 1. Basic of aperture synthesis method using linear array sensor.

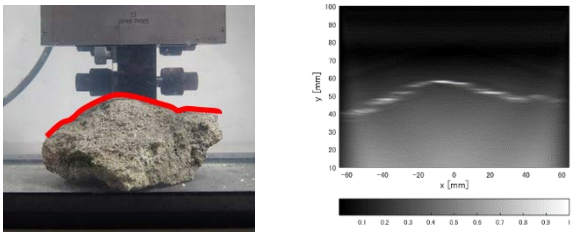

(a) (b)

Fig. 2. (a) Measurement setup (b) Results of the reconstructed image using aperture synthesis method.

2.2. Robotic transport and phased array UVP measurement for leakage point inspection.

For detection water leakage location, a crawler robot was developed. The phased array sensor was mounted on the crawler robot arm. Thus two-dimensional flow mapping is possible to be conducted. Figure 3 shows the measurement setup and the measurement were done at five different locations. As a result, flow mapping was done as depicted in Fig. 3. (b). The flow pattern of two-dimensional velocity can observe the location of water leakage.

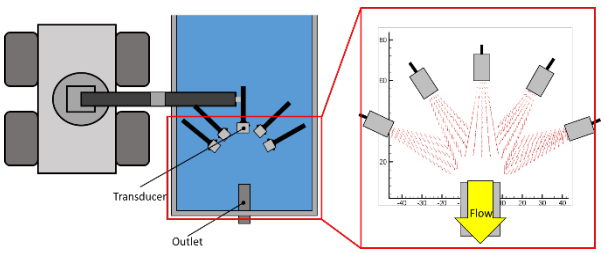

(a) (b)

Fig. 3. (a) Crawler robot transport and ultrasonic sensor (b) Result of 2D flow mapping using phased array UVP.

3. Summary

The possibility of determining the shape of the object and identifying water leakage location by ultrasonic method was verified.

Reference

1. T. Kawachi, H.Kikura *et al.*: International Conference on Advancing the Global Implementation of Decommissioning and Environmental Remediation Programmes, IAEA, 2016, Madrid, Spain.

A.11 Developing the Three-dimensional Object Shape Imaging System with Air-coupled Ultrasonic Sensing

Hiroshige KIKURA

1. Introduction

Retrieval of fuel debris is one of the most urgent issues regarding the decommissioning of Fukushima Daiichi Nuclear Power Plant (NPP). Retrieval fuel debris has many challenges due to the complicated internal structure and high radiation exposure in the surrounding air. In this study, ultrasonic measurement is proposed because of ultrasonic technique's some advantage *e.g.* the feasibility in the severe environment such as the high-radiation environment. Practically, the air-coupled ultrasonic technique has more difficulties to be applied in the air such as high attenuation and low acoustic impedance compared with in water and solid materials. Therefore, we employed the point focus sensor (Fig. 1) which can converge ultrasonic energy in the smaller measurement area. In 2016, the following activities and fundamental studies were conducted:

1. Auto-measurement system which consists of electric stage, stage controller and PC was developed (Fig. 2). This system enabled several measurements precisely and automatically.
2. The three-dimensional object shape imaging program were designed based on distance measurement using ultrasonic sensor. The reconstructed image using this program were evaluated.

These showed the ultrasonic measurement features and good performance on object shape measurement.

Fig. 1. Point focus sensor

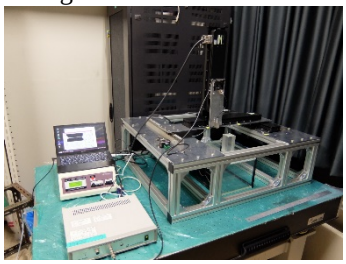

Fig. 2 Auto-measurement system with electric stage

2. Object shape imaging experiment

2.1. Measurement method and apparatus

The distance *l* between the object and the sensor is calculated using a following simple relationship.

$$l = \frac{ct}{2}. \qquad (1)$$

where *c* is the velocity of sound in the air, and *t* is a transit time of the echo signal. The measurment apparatus is showen in Fig. 3. The apparatus consisits developed measurment system, the point-focus ultrasonic sensor, and pulser/receiver. The rock imitates fuel debris were measured as the object. The distance *L* between the top of the rock and sensors was 40 mm same as the focal length of the point focus sensors. The object shape was reconstructed scanning the ultrasonic distance measurement.

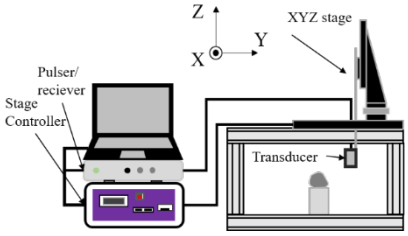

Fig. 3. The apparatus of the air-coupled ultrasonic imaging

2.2. The results and Conclusions

Object shape of the reconstructed image (Fig. 4) showed good agreements with edge photo which extract the edge of the objects (Fig. 5). The results showed good performance of the air-coupled ultrasonic imaging in the condition of the distance *L* was 40 mm.

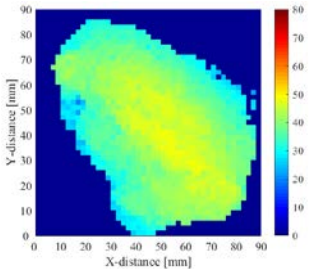

Fig. 4 Reconstructed image

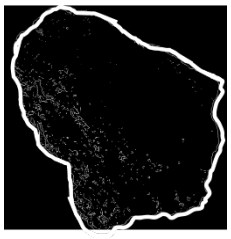

Fig. 5. Edge photo

Reference

1. H. Kiuchi, S. Kimura, K. Tsukada, H. Kikura, D. Sasa, S. Omori: Fundamental study on measurement of object shape and surface flow by air-coupled ultrasound; The Japanese Society for Experimental Mechanics, Osaka, September 1-3, 2016, A060
2. H. Kiuchi, S. Kimura, H. Kikura, D. Sasa, S. Omori: Fundamental study on three-dimensional measurement of object shape by air-coupled ultrasound; AESJ Young Researchers Forum, Tokyo, November 2, 2016, A-11
3. H. Kiuchi, S. Kimura, H. Kikura, D. Sasa, S. Omori: Fundamental study on measurement of fuel debris' surface shape by air-coupled ultrasound; Conference for R&D Initiative on Nuclear Decommissioning Technology by the Next Generation, Tokyo, March 7, 2017
4. H. Kiuchi, S. Kimura, H. Kikura, D. Sasa, S. Omori: Fundamental study on shape measurement of specimens in imitation of debris by air-coupled ultrasound; The Japanese Society of Mechanical Engineers, March 16, 2017, 717

A.12 Ultrasonic Velocity Measurement for Compacted Bentonite

Hiroshige KIKURA, Kazumi KITAYAMA

1. Introduction

One of the important issues of nuclear power is how to deal appropriately with the high-level radioactive waste (HLW). The HLW contains high level radioactivity and various types of long-lived nuclides. The HLW should be isolated from the human environment for a very long time period by a combination of engineered and natural geological barriers since the radioactivity will remain for more than 10,000 years. The engineered barriers consist of the vitrified glass, overpack, and buffer material. For example, buffer material is installed at the outermost part of the engineered barriers to provide stable chemical and physical environment for inner engineered barriers. Bentonite, which is a clay material, is considered to be a good candidate for the buffer material of geological disposal because of its swelling property, low water permeability and low diffusion for nuclides. Bentonite is planned to be compacted and installed in the disposal repository. Understanding groundwater behavior inside compacted bentonite is the most important issue for evaluation of radionuclides transfer for long-term safety. Recently, the effect of water content on elastic properties of compacted bentonite has been investigated by ultrasonic velocity measurement [1]. Ultrasonic measurement technique for water saturation level in compacted bentonite was proposed. In this study, Longitudinal wave velocities measurement was carried out in order to investigate the relation between the velocities and water content in bentonite.

2. Velocity determination method

In order to obtain the velocity of bentonite, group delays were calculated. Group delay can be calculated from a reference signal r(t) and a transmitted signal t(t) as follows.

$$R(\omega) = \int_{-\infty}^{+\infty} r(t)e^{-i\omega t}dt = |R(\omega)|e^{-i\phi_r(\omega)}$$

$$T(\omega) = \int_{-\infty}^{+\infty} t(t)e^{-i\omega t}dt = |T(\omega)|e^{-i\phi_t(\omega)}$$

Where ω is angular frequency. R(ω) and T(ω) are Fourier transforms of reference signal and transmitted signal, respectively. Φ_t(ω), ϕ_r(ω) are phase of reference signal and phase of transmitted signal. The differentiation of phase spectrum, the slope of phase spectrum, indicates the group delay. The group delay corresponds to the transit time of the signal. In order to obtain the transit time, the calibration of the initial phase using the signal of reference specimen is required. The polycarbonate specimen was used as the reference specimen.

$$\mathrm{t_g}(\omega) = \frac{d}{d\omega}(\phi_t - \phi_r)$$

Where t_g is the calibrated transit time.

3. Velocity measurement in compacted bentonite

The sample material of pure smectic bentonite powder (Kunipia-F) was prepared for the compacted specimen. Kunipia-F is a purified bentonite and a content of a smectite, the main component of bentonite, is more than 99%. The experimental apparatus consists of two ultrasonic transducers for longitudinal wave (B0.5C20N, Japan Probe Co., Ltd.) a pulser/receiver (JPR-10CN, Japan Probe Co., Ltd.), a computer, and an external amplifier (PR-60A5, Japan Probe Co., Ltd.). The transducer for longitudinal wave has an element with a diameter of 20 mm. The center frequency of the transducer is 500 kHz. Transducers were installed in opposite position at both ends of a specimen. The frequency of the emitting wave was 500 kHz. The calibrated transit time was obtained by averaging the group delay between 100 kHz to 500 kHz.

Figure 1 shows the variation of longitudinal wave velocity with varying a degree of saturation. Red circles, green circles, blue circles, and purple circles are water content of ~20%, ~25%, ~30%, and ~35%, respectively in Fig.1. The longitudinal wave velocity increases with increasing the degree of saturation. It can be found that the velocity at a degree of saturation of 100% is very close to at the longitudinal wave velocity of 1,480 m/s in water. Furthermore, the longitudinal wave velocity at low water content level is higher than high water content level in the same degree of saturation. Consequently, the proposed method for compacted bentonite can measure longitudinal wave velocity.

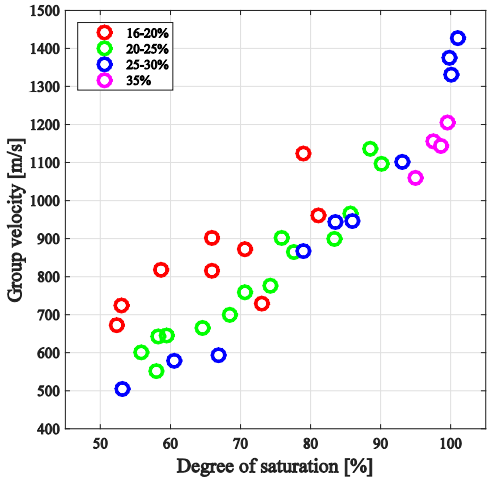

Fig.1. The variation of longitudinal wave velocity with varying a degree of saturation.

Reference

1. S. Kimura, H.Kikura *et al.*, *2016 Fall Meeting of the Atomic Energy Society of Japan*, 2016, Fukuoka Japan, 2D12.

A.13 A Solar Cavity Receiver with Coiled Tubes: Modeling

Hiroshige KIKURA, Kentaro KANATANI, Yutaka TAMAURA

1. Introduction

A model of a solar cavity receiver using helically coiled tubes as heat absorber has been developed. The receiver geometry of the model mimics that of an experiment for a Cross Linear concentrating system at a test site in Minamisoma, Fukushima, Japan, although the model has a potential for application to the same type of receivers.

2. Receiver geometry

Four helically coiled tubes with five turns are combined as shown in Fig.1, and covered by insulators except for the bottom or the aperture. The coil height is 700 mm, and the coil inner diameter is 500 mm. The design parameters of the receiver have been chosen based on optical simulation.

Fig. 1 Heat absorber tubes used at the test site

3. Modeling

The modeling of the receiver contains three procedures. The first is optical simulation, the second is derivation of absorbed heat distribution, and the third is determination of the temperature distribution of the receiver.

3.1. Optical simulation

From the heliostat field at the test site (Fig. 2), the flux density distribution of the concentrated solar light incident on the inner wall of the cavity receiver is obtained using the Monte Carlo ray-tracing technique. The flux density distribution on the receiver is illustrated in Fig. 3.

3.2. Absorbed heat distribution

Absorbed heat distribution is calculated from the incident flux distribution applying conservation of the solar radiation.

3.3. Temperature distribution

The steady-state temperature distribution of the heat transfer fluid and the coiled tubes is sought from the absorbed heat distribution applying energy conservation. Since the cavity receiver for the CL concentrating system is fixed and the aperture almost faces downward, the convective heat loss from the cavity is neglected. Here, a heat transfer coefficient between the tube and the fluid within the tube is prescribed instead of solving the bulk equations of the fluid. From the temperature distribution of the fluid (air in this work), the pressure drop along the coiled tube and the required pumping power for the heat transfer fluid can also be estimated.

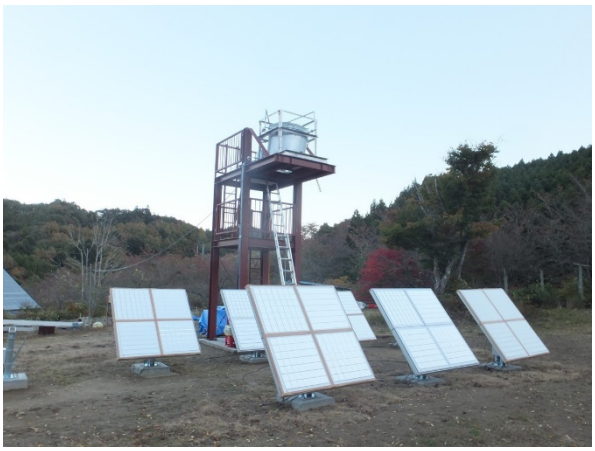

Fig. 2 Heliostat field at the test site

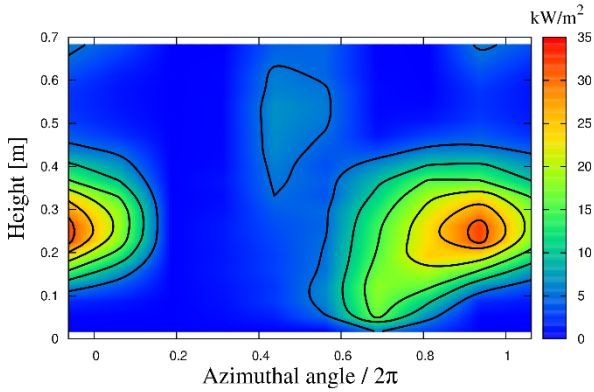

Fig. 3 Flux density distribution of the concentrated solar light incident on the inner wall of the cavity receiver from the heliostat field. The azimuthal angles 0 and $\pi/2$ are oriented to the south and the west. The height 0 is located at the center of the inlet.

Reference

1. T. Aiba, K. Kanatani, Y. Tamaura and H. Kikura, Feasibility Study on 20 MWe Cross Linear Concentrated Solar Power Plant, Proceedings of ASTECHNOVA 2015, Yogyakarta, Indonesia, Paper No.2.

B. Actinide Management Division

B.1 Enhanced Desorption of Cesium from Vermiculite by Hydrothermal Treatment with Divalent Cations

Kenji TAKESHITA, Xiangbiao YIN, Hideharu TAKAHASHI, Yusuke INABA

1. Introduction

Following the accident at Fukushima Dai-ichi Nuclear Power Plant (FDNPP) in March 11, 2011, radioactive Cs (^{137}Cs and ^{134}Cs) have widely contaminated the area around the northern Kanto and Tohoku regions in Japan. Since Cs isotopes are mainly retained within the surface 5 cm of the soil as a result of their selective sorption on clay minerals, topsoil had been extensively stripped and therefore large amount of contaminated soils (18.7~28 million m^3) has been generated and accumulated from the primary decontamination activities, most of which currently are stored at several temporary storage sites and being transferred to interim storage facility (ISF) for further treatment prior to final disposal. Subsequently, the remediation of these cumulated hazardous soils and their volume reduction have become the subject of renewed attention. As a standard Cs decontamination technology has not been unequivocally established currently, it is critically necessary that investigations with more efficient Cs^+ desorption could be attempted in order to satisfactorily remediate the Cs-contaminated soils in Fukushima.

In our previous work, we elucidated that Cs intercalated in vermiculite was effectively desorbed by exchange with various cations in seawater[1]. The most notable finding is that hydrothermal treatment of the Cs sorbed vermiculite with seawater could greatly promote desorption efficiency while details of desorption process by each cation are not completely clear. In present study, we further attempt to report this novel technical method to efficiently desorb Cs^+, especially from the collapsed interlayer regions of vermiculite[2]. Herein, the refinement of desorption process with mechanism classification is of critical importance.

2. Experimental

2.1. Materials

The used vermiculite (termed as Verm) sample, a 2:1 phyllosilicate clay mineral, was purchased from Vermitech Co. Ltd, Japan. Verm particles were firstly sieved to size of 250~710 μm and washed using distilled water for 5 times to dissolve the impurities. Then, the samples were dried in an oven at 40°C prior to the experiment. Reagent grade CsCl was purchased from Wako Pure Chemical Industries, Japan and employed without further purification. All other used reagents were of analytical grade (or higher).

2.2. Adsorption Experiments

The Cs adsorption on Verm was measured in polyethylene test tubes at ambient temperature with batch method. We prepared two Cs-sorbed Verm specimens at low and high loading levels (denoted as Verm-low and Verm-high, respectively). In detail, Verm (1 g) was equilibrated in 0.1 L of solutions containing 0.1 mM NaCl, 0.075 mM CsCl for low loading level, and 7.5 mM CsCl for high loading level during 38 days with continuous stirring. After achieving sorption time, suspension was centrifuged and the supernatant was separated from the solid particles by filtering through membrane filter of 0.2 μm. Cs sorbed Verms were dried at 75°C for 24 h while the Cs^+ amount remaining in filtrate was measured by atomic absorption spectroscopy (AAS, SpectrAA-6200, Shimadzu Corp). The adsorption quantity of Cs^+ thus obtained were calculated as 5.49×10^{-3} mmol g^{-1} and 2.69 mmol g^{-1} to Verm-low and Verm-high samples, corresponding to 2% and 100% of the saturation amount, respectively

2.3. Desorption Experiments

We carried out the desorption experiments in two different procedures (i.e. ambient and hydrothermal desorption treatments). During two procedures, desorption treatment was conducted according to a sequential extraction method, which allows to indicate the inefficiency of a single treatment and to identify some after-effects as well as to compare the highest desorption yield and patterns achieved for each desorption reagent. In the ambient treatment procedure, two Cs-sorbed Verms (100 mg) were suspended in 10 mL of aqueous solution containing various 0.01M chloride electrolytes (NH_4^+, Na^+, K^+, Mg^{2+} and Ca^{2+}). Triplicate batches were conducted for each condition. The mixture was shaken end-over-end for 50 h for the first three repetitions and 250 h for the fourth treatment. In each extraction, once after filtering the suspensions, the precipitates were dispersed again in a same freshly prepared electrolyte solutions and Cs^+ amounts in filtrate were used to determine the desorption yield.

In the second procedure, hydrothermal treatment (HTT) desorption was carried out in same sequential extraction method as that used in ambient desorption, but at increased temperature, with 5 times repetition and in shorter contact time. Cs-Verm powder (500 mg) was mixed with 50 ml of each electrolyte solution in a stainless steel cylinder reactor (51 mm × 260 mm, MMJ-500, OM-Labotech Co., Ltd.). Then the suspension was subjected to heating at specific temperature (100-250°C) for 30 minutes within a nitrogen atmosphere and maximum saturated vapor pressure below 4 MPa. The subsequent desorption yield was evaluated by centrifuging the suspension once the mixture was cooled down to 70°C and determining the Cs^+ amount in separated supernatant. During the whole desorption treatment of two procedures, the solid-liquid separation, drying of the Cs-desorbed Verm particles, analysis of Cs^+ amount in filtrate were all strictly same as those in adsorption section.

2.4. X-Ray Diffraction (XRD) Measurements.

The XRD pattern for each Cs sorbed and desorbed dry Verm samples was obtained using a powder X-ray diffractometer (MultiFlex, Rigaku Co.) with CuKα line

radiation (λ = 0.15406 nm) at 40 kV and 20 mA. Verm clay fine particles were crushed briefly in a mortar before the XRD measurements. Each measurement scan was performed at room temperature for 2θ= 3° to 10°, with a step interval angle (θ) of 0.02° at a rate of 0.2°/min.

3. Results and Discussion

3.1. XRD patterns of Cs sorbed vermiculite.

Figure 1 reveals the corresponding XRD patterns of original Verm and Cs sorbed Verms (i.e. Verm-low and Verm-high). In case of original Verm, there were totally five diffraction peaks occurring at 2θ = 3.5°, 6.1°, 7.1°, 7.3° and 8.7° in the low-angle regions from 3 to 10°, which corresponded to the basal space of 25 Å, 14.3 Å, 12.4 Å, 12.0 Å and 10.1 Å, respectively. These observations implied that such Verm included several different layers. Among which, the peaks at 2θ values of 6.1° (14.3 Å) corresponded well to interlayers containing hydrous Mg^{2+} in the basal space. Additionally, the weak but sharp peak at 8.7° (10.1 Å) was well matching the reflection obtained for the K^+-mica layer. Finally, weak broad peak at around 2θ = 3.5° (25 Å) and intense broad peak at 7.1°/7.3° (12.4 Å/12.0 Å) were reasonably interpreted as the nearly regular 1:1 and random interstratification between the K^+-mica layer and Mg^{2+}-Verm layer, respectively. Based on XRD identification by some of previous studies, these five diffraction peaks can be separately identified as a Mg-vermiculite phase for the 14.3 Å peak, a k-mica phase for the 10.1 Å peak and an interstratification phase for the 25Å and 12.4 Å/12.0 Å peaks. Therefore, our results revealed an accurate identification of the interstratified structure for the used vermiculite.

On the other hand, comparing the XRD patterns of Cs sorbed Verm with that of original Verm, it clearly suggested that the different loading level of Cs^+ on Verm produced its varied layer structure. A recent study has proved that the adsorption of Cs in Mg-vermiculite proceeded by selectively exchanging with preexisted Mg^{2+} but not with K^+. Therefore, such structure variation was mainly induced by interaction of Cs^+ in hydrous Mg-layer. At low loading level, the primary peaks of Verm-low sample approximately overlapped with those of original Verm, indicating their similar interstratified structure as a result of few replacement of preexisted Mg^{2+} by adsorbed Cs^+. Meanwhile, it suggested that such a low loading level of Cs^+ on Verm was not high enough to obviously form dominant degree of interlayer collapse. However, as opposed to the abovementioned case, the main characteristic peaks of Verm except for the one at 8.7° (10.1 Å) totally disappeared upon Cs^+ saturated sorption. These results could be well explained by the transition from Mg^{2+}-Verm layers to Cs^+-substituting layers. When originally occupied Mg^{2+} was progressively substituted by Cs^+ in a mono-interlayer, this gradually resulted in dehydration of Cs^+ due to its low hydration energy and subsequently forming of collapsed Cs-layer with the peak around 2θ = 8.2° (10.7 Å). Such phenomenon of structural collapse upon Cs sorption at high loadings has been similarly found for other vermiculites.

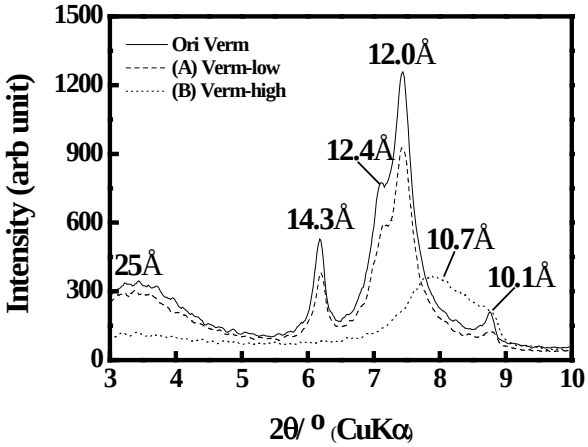

Fig. 1. XRD patterns of original and Cs sorbed Verm, with d spacing values in Å. (Solid): original Verm. (Dash): Verm-low (Dot): Verm-high.

3.2. Effect of interlayer collapse on the inhibition of Cs desorption.

The Figure 2 indicated the batch desorption results from Verm-low and Verm-high specimens, respectively. Overall, it demonstrated that intercalated Cs on Verm-low and Verm-high both underwent further replacement by various cations leading to a different degree of back-release. Firstly, when treating the Verm-low with 0.01M electrolyte, it showed that most sorbed Cs was readily desorbed by divalent cations and presented a desorption order as $Ca^{2+} \approx Mg^{2+} > K^+ > Na^+ > NH_4^+$ (Figure 2a), which is opposite to the selectivity of cations to the interlayer sites of vermiculite. Such results were consistent with recently reported observations by Mukai et al. and Tamura et al. that trace amount of sorbed Cs in vermiculitized biotite can be hardly displaced by NH_4^+ while more readily by Mg^{2+}. Since it is generally though that Cs^+ ions in collapsed layers are poorly replaced by divalent cations because decreased interlayer spacing will greatly restrict the entry of divalent cations, it was quite surprising that divalent cations desorbed Cs to a much larger extent (more than 80%). One explanation to this behavior may lie in the dominant sorption of Cs^+ on un-collapsed interlayer/planar/edge sites of Verm-low, although partial sorbed Cs^+ ions tend to concentrate and cumulate in some mono-interlayer space. In contrast, the stripping of Cs from saturated Verm-high was limited under the slight ionic strength (0.01M) for each electrolyte, of which no one attained a desorption yield higher than 20%, suggesting that sorbed Cs^+ occurring mostly in collapsed interlayer region was fixed tightly against replacement for desorption (Figure 2b). Furtherly, it had improved the Mg^{2+} concentration gradient in solution to higher ionic strength (0.1-3M). However, less than 50% of Cs could be desorbed from Verm-high even by the drastic sequential treatments at the highest concentration of 3M. Based on the distinct desorption patterns from two Cs-Verms, it clearly suggested that cation exchange for desorption of Cs^+ from interlayer region of Cs saturated Verm was hard to achieve

at room temperature and was greatly inhibited by interlayer collapse.

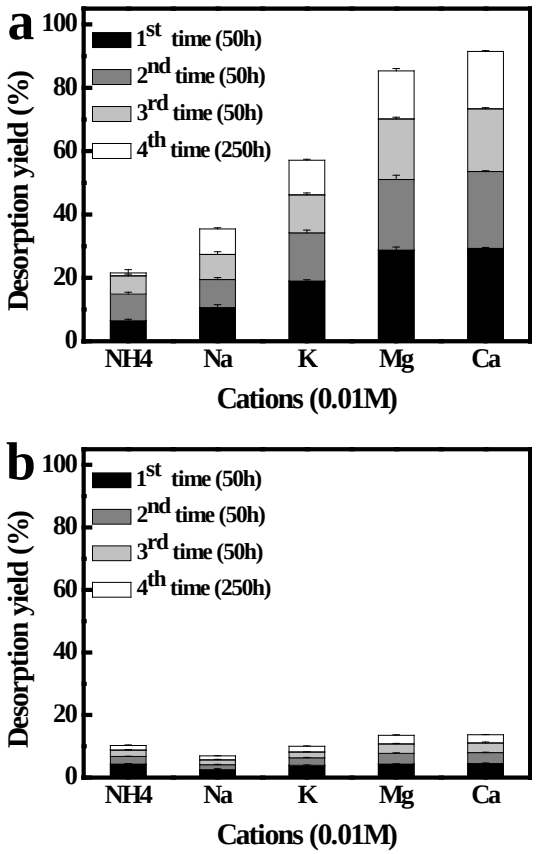

Fig. 2. Sequential Cs desorption as functions of cation species by ambient treatment with 0.01M electrolytes from two Cs loaded Verm. (a) Verm-low. (b) Verm-high.

3.3. Effect of hydrothermal treatment on the enhancement of Cs desorption.

In order to desorb more tightly fixed Cs^+ from the deeper region of collapsed interlayer space in Verm, enhanced desorption had been conducted at elevated temperature. Figure 3 presented the sequential HTT desorption results obtained for Verm-high after 5 times repetitions. It was surprising that desorption patterns obtained for the divalent cations were quite different from those achieved for monovalent cations. In the case of three monovalent cations, total desorption yield after 5 cycles of treatment were still less than 20%, although slight increase was achieved for each cation compared to the results of ambient desorption (Figure 2b). In contrast to the poor efficiency of monovalent cations, desorption with divalent cations could be described as relatively effective in each single extraction and continuous even after several repetitions, presenting a result of significant increase in the total desorption yield. After 5 cycles of treatment, 90-100% removal of saturated Cs^+ was achieved.

To clarify the dependence on temperature of Cs desorption from Cs saturated Verm-high, we further conducted the HTT desorption at different temperatures. Figure 4 revealed desorption results, which indicated that the total desorption yield of Cs^+ after 5 cycles of treatment increased with the heating temperature during HTT. Approximately 30%, 55%, 88%, and 100% of Cs^+ were finally desorbed by 0.01M Mg^{2+} at 100 ^oC,150 ^oC,200 ^oC,and 250 ^oC,respectively.

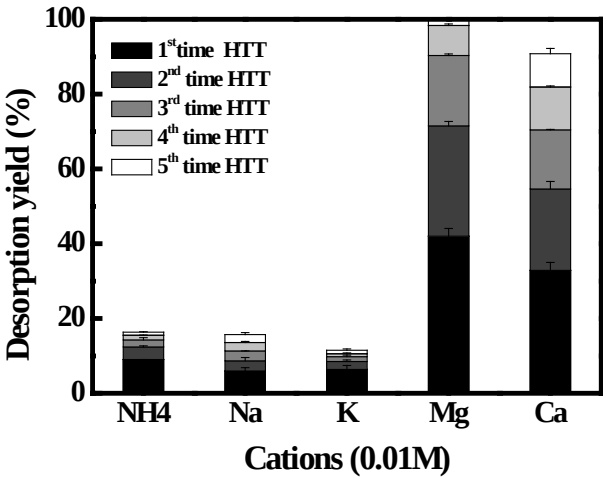

Fig. 3. Sequential Cs desorption from Cs saturated Verm as functions of various cation species by hydrothermal treatment (V/m: 50 ml/0.5 g; t: 30 min; T: 250^{o}C; Cation: 0.01M).

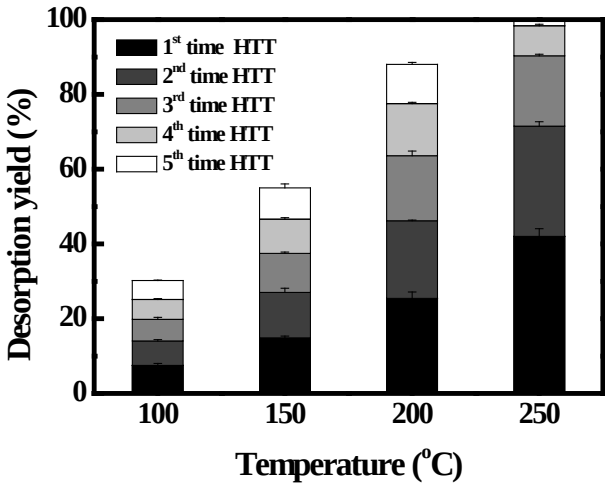

Fig. 4. Sequential Cs desorption from Cs saturated Verm as functions of temperature by hydrothermal treatment with Mg^{2+} (V/m: 50 ml/0.5 g; t: 30 min; Mg^{2+}: 0.01M).

3.4. XRD patterns of Cs desorbed vermiculite.

To account for the effect of temperature on Cs desorption, the Cs saturated Verm-high samples following desorption treatment with 0.01M Mg^{2+} at 25 ^oC and 250 ^oC were analyzed by XRD measurement. Alteration of interlayer structure was revealed by the changes in the basal spacing of XRD patterns to Cs desorbed Verms with referencing those of original Verm and Cs saturated Verm (Figure 5). After treatment at 25 ^oC, the pattern of Cs desorbed Verm approximately overlapped with those of Cs saturated Verm and maintained the unchanged collapsed

interlayer distance (10.7 Å), indicating most of Cs still resided in treated Verm. This result was consistent with the considerably poor desorption yield in ambient desorption treatment (Figure 2b). In contrast, after hydrothermal treatment, the Cs depleted Verm showed a significant change of the basal spacing, which reappeared again the interlayer distances of Mg-layer for 14.3 Å and interstratification distance for 25.0 Å/12.4 Å/12.0 Å, suggesting that Mg^{2+} indeed intercalated into the collapsed Verm interlayers and once again substituted fixed Cs in these regions. Moreover, compared to the original Verm, the Cs depleted Verm showed an increase of intensity of the interstratification peak at 7.1° (12.4 Å), while a decrease of that of interstratification peak at 7.3° (12.0 Å) and K^+-mica peak at 8.7° (10.1 Å). The shift of dominant interstratification distance changing from 12.0 Å for original Verm to larger 12.4 Å for Cs depleted Verm clearly suggested that higher proportion of Mg^{2+}-Verm layer to K^+-mica layer was presented in the crystal of Cs depleted Verm than that of original Verm. This result proved that Mg^{2+} not only indeed completely desorbed all Cs^+ in collapsed Cs^+-layers but also substituted K^+ in some (not all) mica layer under HTT condition, being well consistent with earlier reported observations.

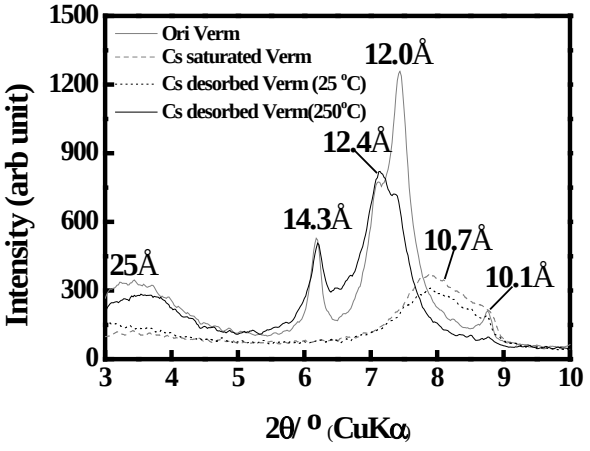

Fig. 5. Typical XRD patterns of original Verm (Gray solid), Cs saturated Verm (Gray dash) and Cs desorbed Verm by sequential treatment with 0.01M Mg^{2+} at 25 °C (Black dot) and 250 °C (Black solid), with d spacing values in Å.

Desorption of Cs from standard clay minerals or soils has been previously attempted by various cations, suggesting that desorption efficiency depends on the used cation species. Generally, divalent cations (Mg^{2+}, Ca^{2+}) can desorb more Cs^+ than monovalent cations (NH^{4+}, Na^+, K^+) from vermiculite/smectite clay fractions, while contrary is true for Cs desorption from illite/ muscovite clay fractions. In accordance with these earlier observations, Cs sorbed on Verm-low was desorbed more readily by leaching with divalent cations than with monovalent cations in present study, while saturated Verm-high bound Cs tightly against desorption by either divalent or monovalent cations at room temperature (Figure 2). These results could be well explained as the results of the varied Cs fixation scenarios in Verm-low and Verm-high samples and the different ionic properties (i.e. hydrated radius, hydration energy and ionic valence) between divalent and monovalent cations.

In the case of divalent cations, they have the larger hydrous radii and ionic valence than that of monovalent cations, which were generally able to desorb some Cs^+ interacted on the accessible edge, un-collapsed interlayer sites and planar sites of Verm through electrostatic attraction with the structural negative charge (Figure 2a). However, they were less effective in desorbing Cs present in the collapsed area because of their larger hydrated radii and thus limited entry into the collapsed space even at a relatively high concentration of 3M at ambient temperature. In contrast, monovalent cations have smaller hydrous radii and closer selectivity with respect to Cs on clays than that of bivalent cations, which can access to FES or collapsed interlayers and therefore generally are thought to desorb Cs more easily. However, when they are used to desorb the Cs^+ mostly sorbed in un-collapsed interlayer sites, such cations would tend to firstly exchange with the surplus hydrous Mg^{2+} rather than the sorbed Cs^+, accompanied with collapsing the edge-interlayer sites tightly due to their considerably low hydration energy and, in turn, hindering the Cs exchange for desorption in the subsequent sequential extraction. Such process explained why lower desorption yield was achieved by monovalent cations than that by divalent cations (Figure 2a). On the other hand, to desorb the Cs^+ in collapsed area from Verm-high, the considerable poor desorption yield of monovalent cations was reasonably attributed to the limited diffusion of these cations into collapsed layers for cation exchange under the slight leaching ion strength gradient, even if the collapsed basal spacing permits the entry of these cations for their smaller ions radii. While such situation could be improved by desorption at higher monovalent electrolyte concentration, as the cation diffusion within interlayer space would be more facilitated by the higher ion strength gradient. In addition, when increasing the number of treatment repetitions, a decrease of desorption yield in subsequent sequential operation was found for all of five electrolytes (Figure 2/3), indicating a gradually increased resistance of Cs desorption. This can be explained reasonably simply as increasing fraction of residual Cs were located near the center core area of Verm particles and leading to the increasing obstacle of Cs interlayer diffusion for desorption in sub-extraction. All these results strongly supported inhibition of Cs desorption by interlayer collapse, thus any effective decontamination measure should account for this situation and attempt to desorb these tightly fixed Cs^+ from collapsed interlayer regions.

Surprisingly, continuous back-release of tightly fixed Cs^+ in collapsed Verm when treated with divalent electrolytes at elevated temperature was opposite to its poor desorption by ambient treatment (Figure 2/3), suggesting positive effect of temperature on enhancement of cation exchange for Cs desorption. Liu et al., in experiments with 0.5 M $NaNO_3$ at 55°C, found that elevating temperature

allowed more replacing of Cs^+ by Na^+ for Hanford sediments, leading to the similar results presented here. However, these results were in contrast with the earlier observations that Cs desorption from sediment containing vermiculite and illite was reduced after heating treatment (>200ºC) of Cs sorbed sediment itself or in water solution without replacing cations. The reduction in desorption with elevating temperature was due to the interlayer collapse and the formation of secondary Cs-containing phyllosilicates at high temperatures. As a result, the findings of this work clearly suggested that the effects of hydrothermal treatment with divalent cations were expected to overwhelm the interlayer collapse and secondary phyllosilicates formation in temperature range (100-250ºC) leading to readily release of Cs. Also, it should be important to note that some released Cs^+ during HTT may resorb again on Verm during cooling to 70ºC from the heating temperatures (100-250ºC), as the substitution of Cs^+ in Verm by replacing cations (Mg^{2+}/Ca^{2+}) in solution is a reversible reaction. Nevertheless, almost all fixed Cs^+ within collapsed interlayer position had been quantitatively desorbed into the solutions after 5 cycles of treatments. Complete desorbability has been attributed to three major factors: a) decollapse of the edge-collapsed interlayer region induced by treatment of strongly hydrated divalent cations (Mg^{2+}/Ca^{2+}) rather than monovalent cations (NH_4^+/Na^+/ K^+) at elevated temperature due to their larger hydrated radii, which might be a necessary initial step to destabilize and remove all of fixed Cs in collapsed region; b) facilitated diffusion of Cs^+ within collapsed interlayer regions; and c) a decrease in hydration radius of the Cs^+ cation at higher temperatures (70ºC), which may have resulted in a decreased selectivity of the clays for Cs^+ and hence decreased re-sorption of Cs^+ by the Verms after Cs^+ release during HTT.

For the remediation of Cs contaminated soils in Fukushima, the Cs desorption using an appropriate reagent electrolyte consisting of specific cation could be effective. General candidates for efficient Cs removal are divalent cations for vermiculite/smectite clay fractions but monovalent cations for illite/micaceous clay fractions. Our results indicated that divalent cations can desorbed more Cs from un-collapsed interlayer sites, while high concentrated monovalent cations can desorb more Cs from collapsed interlayer sites, implying that the desorption treatment at room temperature using only monovalent or divalent cations may fail to easily desorb all Cs in soils and is not efficient for the remediation. This incomplete desorption could be a result of readily induced interlayer collapsed by monovalent cations, limited entry of divalent cations into collapsed interlayer regions and slow diffusion of Cs^+ ions inside of collapsed interlayer space.

However, almost all the saturated Cs^+ was desorbed after 5 cycles of HTT with 0.01M Mg^{2+}. Taking into account low divalent cation concentration (0.01M) and short retention time (0.5h) employed in each HTT, it clearly suggested the potential availability of HTT approach for Cs desorption, especially from severe Cs fixation scenario encountered in field situation (i.e. in collapsed interlayer sites or FES) by achieving short retention time, low environmental stress and good efficiency. Without destructing the phyllosilicate structure of clays, ambient/hydrothermal treatment may rarely change the soils properties and possibly recover them back to the farming lands to reduce the volume of contaminated soils; while the desorbed Cs could be recovered and concentrated by efficient Cs adsorbents and immobilized in stable materials for final disposal. Herein, ambient treatment is recommended to be applied directly to the stripped contaminated topsoils with leaching by divalent rather than monovalent electrolytes; while the classified soils primarily containing higher radioactivity more than 100,000 Bq/kg and/or residual soils with radioactivity higher than 8,000 Bq/kg after ambient treatment can be further treated at elevated temperature. Nevertheless, similarly with decontamination approach of sublimation (650~1000ºC), hydrothermal treatment (100~250ºC) itself may be of high energy consumption and, thus practically limited, it is expected to operate the treatment at temperature as low as possible by optimizing the process through adjusting the treatment time or using a column approach et al in our future work.

4. Conclusion

In this study, desorption of Cs from vermiculite has been investigated in detail by combining sorption with different Cs loading amount and desorption treatment with various cations at changed temperature. At room temperature, Cs^+ sorbed at 2% saturated amount was dominantly fixed within un-collapsed interlayer space and thus was desorbed more readily on leaching with 0.01M Mg^{2+}/Ca^{2+} (more than 80%) than with NH_4^+/Na^+/K^+ (20~60%); However, contrary was true for Cs^+ saturated Verm, on which Cs^+ occurred mostly in collapsed interlayer region and was tightly fixed against replacement by 0.01M divalent/monovalent cations resulting in poor desorption (less than 20%). In contrast with ambient treatment, ~100% removal of saturated Cs^+ was achieved after five cycles of treatment at 250ºC with 0.01M divalent cations rather than monovalent cations. Based on these results, we clarified the effect of cation species and temperature dependence on the Cs desorption from the (un-)collapsed interlayer regions of a 2:1 phyllosilicate clay mineral, elucidated the corresponding desorption process and discussed the mechanism. All these results are expected to provide new insights to explore the available decontamination process for the Cs-contaminated soils in Fukushima.

Reference

1. Xiangbiao Yin, Hideharu Takahashi, Yusuke Inaba, Kenji Takeshita, The Fifth International Symposium on Innovative Nuclear Energy systems (INES-5), Tokyo, Oct. 31- Nov. 2, 2016, B21-1.
2. Yin X.**,** Takeshita K., et al. *Journal of Hazardous Materials*, **326**, 47-53 (2017).

C. Global Nuclear Security Division

C.1 Cs accumulation pathway by filamentous fungi from wood log

Toshihiko OHNUKI, Yukitoshi AIBA, Fuminori SAKAMOTO, Naofumi KOZAI, Tadafumi NIIZATO, and Yoshito SASAKI

Filamentous fungi like mushrooms are well known to accumulate radioactive cesium (Cs) from contaminated wood, litter, and soil[1-2]. Many reports have described the high accumulations of radioactive Cs in wild mushrooms collected around Europe after the Chernobyl nuclear accident, and in Japan before and after the Fukushima Daiichi Nuclear Power Plant Accident. Although all kinds of mushrooms accumulate radioactive Cs, the mechanisms by which radioactive Cs accumulates in the mushroom fruit body from contaminated wood, litter, and soil have not been fully clarified. We here first report the direct accumulation pathway of radioactive Cs from contaminated wood logs to the fruit-bodies of shiitake mushrooms through the basal portion of the stipe[3]. In this pathway, radioactive Cs is not transported through the hyphae. This pathway results in a high accumulation of radioactive Cs in the fruit-body, more by the excess accumulation of radioactive Cs from the wood logs than that through the hyphae.

The spawn of Shiitake mushroom was prepared in sawdust and grain mixed with and without mineral powder. Cylindrical plugs of sawdust spawn 1 cm in diameter and 2 cm in height were inoculated in the radioactive Cs contaminated wood logs (150 $Bq \cdot kg^{-1} \pm 20 Bq \cdot kg^{-1}$ $^{134}Cs+^{137}Cs$). The inoculated wood logs were installed in an uncontaminated forest in Yamanashi, Japan, approximately 300 km from Fukushima Daiichi Nuclear Power Plant, for approximately 5 months (Photo 1). The harvested fruit-bodies collected from the wood logs were powdered for the measurement of radioactivity by an NaI(Tl) scintillation system (EMF211, EMF Japan). After the harvest of Shiitake mushrooms, the wood logs were cut to obtain a cross section at the regions where the fruit-bodies were harvested. The cut wood logs were laid on the imaging plate to obtain two-dimensional images of radioactive Cs in the wood logs by an autoradiography technique.

Photo 1 Mushroom fruit-bodies grown from wood log.

The Prussian blue dyed water was prepared by adding Prussian blue powder at 0.2% weight into water. Well colonized wood logs with no radioactive Cs contamination were submerged into the Prussian blue-dyed water at 15°C. The Prussian blue-dyed water was introduced into the wood logs by vacuum pumping for 2 min. The submerged wood logs were placed in a temperature- and humidity-controlled room until the fruit-bodies were grown. The regions of the wood logs where the fruit-bodies had developed were cut into 13.8×9.6×14.9 mm pieces to measure the distribution of Prussian blue by micro X-ray computed tomography system (Y.CT Compact 320, YXLON).

The photograph (Fig. 1: a) and AR image (Fig. 1: b) of the cross section of the wood log after harvest of the fruit bodies of Shiitake mushrooms showed dense areas of radioactive Cs at positions near the surface of the wood log. The dense areas circled in yellow in the AR image correspond to the inoculated spawn areas where the fruit-bodies were grown, indicating that radioactive Cs was accumulated around the fruit-body area. On the contrary, the white circle in the AR image showed that no dense spots appeared without the presence of a fruit-body even despite the presence of vermiculite powders of 10% in weight, indicating no specific accumulation of radioactive Cs in the inoculated spawn area without the formation of a fruit-body.

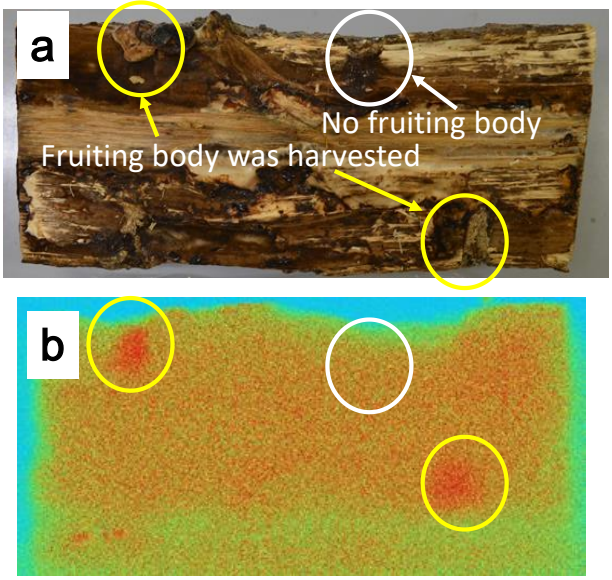

Fig. 1A photograph (a) and AR image (b) of the cross section of the wood log after the harvest of the fruit-bodies of shiitake mushroom. Yellow and white circles show the areas, respectively, where a fruit-body arose and did not arise from the inoculated spawn medium containing 10% weight vermiculite.

In growing Shiitake mushrooms, the wood logs are usually submerged in water for 1~2 days in order to stimulate the formation of the fruit-bodies from the

well-colonized hyphae in wood logs. This submersion treatment dissociates radioactive Cs from the contaminated wood logs into the interstitial water. Thus, the dissolved radioactive Cs in the submerged water of the wood logs was sorbed by the minerals during transport to the fruit-body. We added nano-sized dye of Prussian blue at 10% weight to the submersion water as a tracer of this water. After harvesting the Shiitake mushrooms from a non-contaminated wood log, the distribution of the nano-sized Prussian blue was measured by micro X-ray CT analysis. The nano-sized Prussian blue was distributed just beneath the fruit-bodies (Fig. 2a). The three-dimensional distribution of the Prussian blue showed that the Prussian blue powders were distributed in an ellipsoidal shape from the fruit-body. The cross section of the distribution of Prussian blue (Fig. 2b) showed the presence of an empty area in the center of the ellipse underneath the fruit-body. The color of the fruit-body was not changed while the color beneath the fruit-body was changed to blue. These results reveal that the interstitial pore water was transported toward the fruit-body.

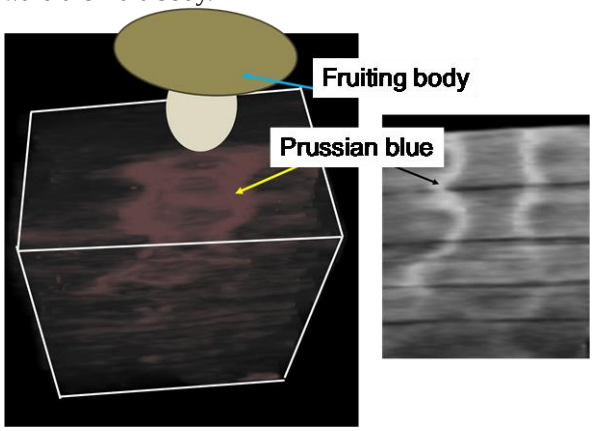

Fig. 2 Three-dimensional distribution (a) and cross section of distribution of nano-sized Prussian blue after harvesting the fruit-bodies from the surface of the wood log. The three-dimensional distribution the Prussian blue in the wood log was determined by X-ray CT analysis, which detected dense materials in the materials. Prussian blue contains Fe in its structure. The determined distribution was identified as that of Prussian blue. The fruit body was illustrated as an image based on the photograph taken after the fruit body was harvested.

The hyphae of Shiitake mushroom were grown on a membrane filter placed on agar medium containing Prussian blue at 0.1% weight, which changes color in the medium to dark blue. Even though the color of the medium was dark blue, the color of the hyphae was white and radioactivity in the hyphae was 0.18±0.022 Bq g^{-1}, showing that Prussian blue and ^{137}Cs did not penetrate into the hyphae. This result clearly suggests that the Prussian blue which accumulated ^{137}Cs in the submersion water was not transported to the hyphae, but through the interstitial water in the wood log outside of the hyphae. It is reported that the addition of the Prussian blue in submersion water of contaminated wood logs decreases the concentration of radioactive Cs in the fruit-body. These findings reveal that accumulation of radioactive Cs from the wood log to the fruit-body results from two processes. One is the pathway by which the radioactive Cs was accumulated through the hyphae. The other is the pathway by which radioactive Cs is transported directly from the interstitial pore water to the fruit-body.

Radioactive Cs is highly accumulated in the fruit-bodies of filamentous fungi. Since radioactive Cs is known to accumulate in hyphae, it is believed that radioactive Cs is transported to the fruit-body through hyphae[4]. Cesium accumulated in the hyphae of *Pleurotus ostreatus* is trapped by intercellular materials of polyphosphate in vacuoles or other organs. Indeed, hyphae function in the uptake and transport of the radioactive Cs dissolved in the interstitial water into the fruit-bodies[5]. Our results showed the presence of a direct pathway of radioactive Cs accumulation into the fruit-body from the contaminated wood logs. In the forest the fruit-bodies of edible and inedible mushrooms tend to grow after rain events. The rain water dissolves radioactive Cs in the litter zone[6]. Some portion of the dissolved radioactive Cs is transported directly to the fruit-body, causing excess accumulation of radioactive Cs in the fruit-body rather than through hyphae. Therefore, direct accumulation pathway of radioactive Cs from the contaminated wood, litter, and soil should be included to understand the migration of radioactive Cs in forest.

Reference

1. S. Yoshida, et al., J. Environ. Radioact. **22**, 141 (1994).
2. G. Heinrich., *Radiat. Environ. Biophys*. **31**, 39 (1992).
3. T. Ohnuki, et al., Scientific Reports, 6:29866 (2016).
4. M. M. Vinichuk, et al. *J. Environ. Radioact.* **78**, 77 (2005).
5. M. A. Bazala, et al., *J. Environ. Radioact*. **99,** 1200 (2008).
6. M. Sakai, M. et al., *J. Environ. Radioact.*. **144**, 15-20 (2015).

C.2 Estimation Technique of Cs Retention Fraction in Irradiated Nuclear Fuel with Intact/Damaged Form

Hiroshi SAGARA, Kazuki NAKAHARA and Chi Young HAN

INTRODUCTION

Even in the case of severe accident such as in TMI-2 or Chernobyl-4 or Fukushima Dai-ichi nuclear power station, waste partitioning in the decommission process or special nuclear material (SNM) accountancy in molten core material is important. Though Cs-137 concentration information is used for burnup estimation in conventional spent nuclear fuels, it could not be applied for damaged nuclear fuel of severe accidents because of both a large release fraction of Cs and significant change of its shape and form by core melting. The ratio of 134Cs/137Cs has often been used as an index of the burnup in the cleanup of TMI-2 and the Chernobyl Drum Assay System in Chernobyl-4 and other cleanup activities, assuming that the Cs isotope ratio inside the fuel matrix would be the same as in the fuel debris, whereas its retention fraction would vary. Cs retention fraction information would be very important for the reliability of the burnup estimation as well as for the severe accident safety analysis. In the present research, a principle of new technique to estimate the Cs retention fraction is proposed and examined by sensitivity analysis of the FP inventory in conventional BWR irradiated fuel numerically, and validated by comparing the past experimental data based on gamma spectrometry[1,2].

METHODOLOGY

A broad parametric survey of inventory was conducted using simple but well qualified generation/depletion calculation codes ORIGEN-ARP. Firstly, fuel burnup calculations were performed with 9×9 BWR fuel assemblies, those irradiation parameters were derived from. Secondly, the candidates of indices of Cs retention fraction were examined by inventories, chemical volatility and gamma-ray measurability.

Here the Cs retention fraction is defined as followings;

$$\text{Cs retention fraction} \equiv \frac{(\#\ \text{of Cs retained in fuel})}{(\#\ \text{of Cs generated in fuel})} \quad (1),$$

whose number is usually unity in case of intact fuel since generated Cs by fission reaction is retained in the original position, though the number would be less than unity in case of damaged fuel.

Finally, the selected indices were validated by gamma spectrometry. comparing with the past experimental data based on try.

RESULTS AND DISCUSSION

Figure 1 shows the results of the axial profile of Cs-134/Eu-154 weight ratios in spent fuel for different irradiation histories, burnup and axial position in BWR fuel assemblies, dots with lines are the calculated and the black circles are the post irradiation examinations (PIEs). Due to the similarity of the production mechanisms of two neutron absorptions,

U-235(n,f) → Cs-133/Eu-153 (n,g) → Cs-134/ Eu-154 (2),

the ratio remains at a nearly constant value with standard deviation σ <10% in any position, burnup and irradiation history. Compared with the PIE results of 3.9% EU, the ratio fits the results of the 3.8% EU assembly within the standard deviation, too. Because of the low volatility of lanthanide oxides from the spent nuclear fuel even in the damaged form, Eu-154 can be considered as a standard nuclide and the difference of Cs-134/Eu-154 ratio between the damaged and the intact could provide Cs retention fraction.

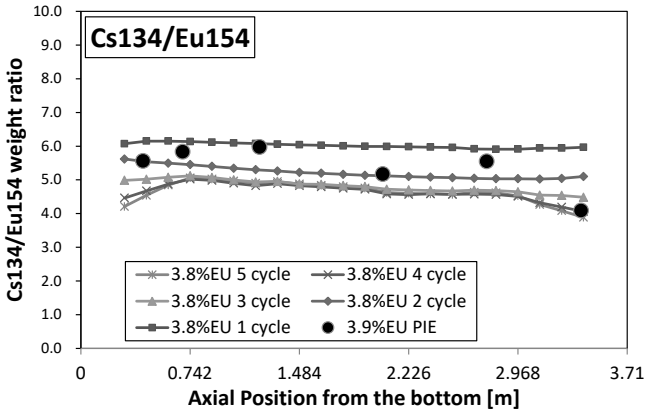

Fig. 1 Cs-134/Eu-154 ratio axial distribution in BWR fuel

A new index to estimate Cs retention fraction in irradiated nuclear fuel is proposed as followings;

$$\text{Cs retention fraction} = \frac{I_{Cs134}(E_1)}{I_{Eu134}(E_2)} \Big/ \frac{I_{0,Cs134}(E_1)}{I_{0,Eu134}(E_2)} \approx \frac{I_{Cs134}(E_1)}{I_{Eu134}(E_2)} / C \quad (3),$$

where $I_{Cs134}(E_1)$ means the photo-peak count rate emitted from Cs-134 with photon energy E_1, and $I_{Eu154}(E_2)$ means that from Eu-154 with photon energy E_2, E_1 = 723.3keV and E_2 = 795.8keV. I_0 in the denominator means the photo-peak count rate in intact fuel, and I in the numerator means that in damaged fuel. Since the denominator of eq. (1) can be considered as a constant value C, independent from any operation parameters in BWRs as shown in Fig. 1 and be prepared by burnup calculation of the fuel, the gamma spectrometry measurement of irradiated nuclear fuel gives the numerator information and derives the final Cs retention

fraction by eq. (1).

Figure 2 gives the outline image of the Cs retention fraction estimation. The most important key characteristics of the Cs retention fraction index proposed in the present research is to utilize only the relative photo-peak intensity of Cs-134 and Eu-154 with similar photon energy, not dependent on any absolute data measurement. It leads the following advantages;

A) its applicability to simple and easy non-destructive methodology passive gamma spectrometry

B) its applicability to damaged fuel with form and/or composition changes because it does not rely on any absolute data measurement

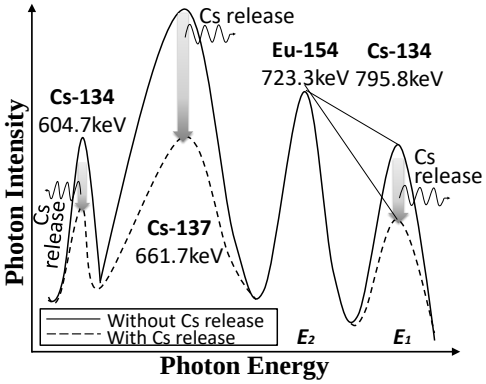

Fig. 2 Cs retention fraction estimation principle by measuring photo-peak ratio of Cs-134/Eu-154

Finally, the index was applied for the past measurements in TMI-2 debris measured in Japan Atomic Energy Research Institute, the former organization of Japan Atomic Energy Agency [4]. In the reference measurement, Cs retention fraction of damaged fuel was measured by the comparison between Cs-137 662keV photo-peak from damage fuel piece and that from intact fuel piece recovered from similar irradiation positions. As one of the measured data, VIP-9H-a was examined and its specification is listed in Table 1. The gamma spectrometry data is shown in Fig. 3, and the photo-peak of Cs-134 795.8keV and Eu-154 723.3keV were clearly observed. By using the photo-peak data from the results for the numerator of eq. (3), and the intact fuel inventory information for the denominator *C* of eq. (3), the Cs retention fraction is estimated as 5.1 % by the present index, much closed to the reference data 5.3 %. The index was also applied to the other samples from various recovery positions, and there was generally good agreement with the reference data. It will be discussed in more detail in the presentation.

Table 1 The specification of VIP-9H from TMI-2 samples

Sample ID	VIP-9H a
Burnup, MWd/t	3,500
Sampling location	Lower plenum
Weight, mg	61.31
Appearance	Resolidified Ceramic Particle

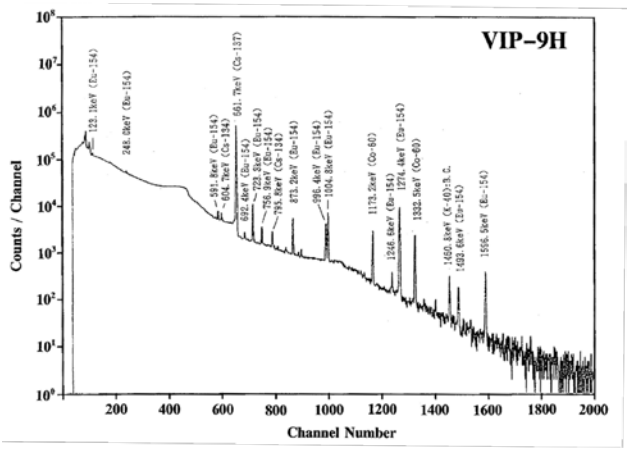

Fig. 3 An example of gamma spectrum measured in TMI-2 debris sample [3]

CONCLUSIONS

In the present research, a principle of new technique to estimate the Cs retention fraction is proposed and examined by sensitivity analysis of the FP inventory in conventional BWR irradiated fuel numerically, and validated by comparing the past experimental data based on gamma spectrometry. A new index to estimate Cs retention fraction in irradiated nuclear fuel was proposed as a fractional index, the numerator photo-peak ratio emitted from Cs-134 and Eu-154 measured by simple passive gamma spectrometry, and the denominator as the ratio prepared by burnup calculation of the intact fuel. It was confirmed that the denominator of Cs-134/Eu-154 inventory remained at a nearly constant value with standard deviation □ <10% in any position, burnup and irradiation history, validated with post examination results. The overall index applicability to damaged fuels was investigated by using the past post-exanimated TMI-2 fuel data, and there was generally good agreement with the reference experimental data. More data are under examination, the detail will be reported in the presentation.

REFERENCES

1. Hiroshi SAGARA et al., Trans. Ame. Nucl. Society, Vol. 115, Las Vegas, NV, November 6–10, 2016
2. Hiroshi. SAGARA, et al., *J. Nucl. Sci. Technol* , vol. 51, No. 1 (2014).
3.Hiroshi UETSUKA et al., *JAERI –RESEARCH 95-084* (1995).

C.3 Material Balance Area Design for the Transuranic Fuel Cycle Employing High Temperature Gas Cooled Reactors

Takeshi AOKI, Hiroshi SAGARA

A major impetus has been to ensure safety in nuclear power plant systems from the beginning of its development to the current period of nuclear renaissance. As one of the next generation reactors with a high level of nuclear safety, high temperature gas cooled reactor (HTGR) has attracted large attention because of the possibility to shut down the reactor safely and remove decay heat without the use of active cooling. A deep-burn concept of fuel utilization is proposed and studied for HTGRs to alleviate plutonium proliferation concern. The idea is to utilize the plutonium extracted by reprocessing the light water reactor (LWR) spent fuel and discharge it only at higher fuel burn-ups of up to 90 atom %. In addition HTGRs have been studied to utilize transuranic (TRU) fuel. A large amount of special nuclear material (SNM) will be used in the HTGR advanced fuel cycle. The inherent proliferation resistance and material attractiveness of the fresh fuel and discharged spent fuel have been discussed against the diversion from peaceful to military uses.

On the other hand safeguards of SNM is also important to prevent nuclear proliferation under the Non-Proliferation Treaty between the state and International Atomic Energy Agency (IAEA). Facility operators are responsible to design material balance area (MBA) and provide enough information on material balance of SNMs for the safeguards conclusion. The material unaccounted for (MUF) and measurement uncertainty in MUF (σMUF) represent accuracy of material balance. The MBAs have to be designed and established to achieve enough confidence level on MUF and σ MUF. The MBA design is challenging for nuclear facilities managing large amount of bulk (instead of items) SNM because of potentially large MUF and σMUF. A concept and guidance of MBA design for uranium fueled HTGRs has been discussed

In this study, a MBA design is presented for the transuranic fuel cycle employing HTGRs. The MUF and the σ MUF is calculated and evaluated using international target values (ITVs) provided by the IAEA.

An MBA design was presented for safeguarding a fuel fabrication facility and a nuclear power plant in advanced transuranic fuel cycle employing HTGRs. The MUF and measurement uncertainty in MUF were evaluated using the ITVs provided by the IAEA. It was confirmed to achieve 99% of confidence level and enough accuracy to draw safeguards conclusion with the MBA configuration provided with the assumed MBP value of one month. Assuming that the MBP for non-irradiated and irradiated nuclear materials set to one month, the MBA design was available for the fuel cycle employing one HTGR core. Up to 2% of holdup for the equilibrium flow rate was acceptable in the bulk MBA in the fuel fabrication facility.

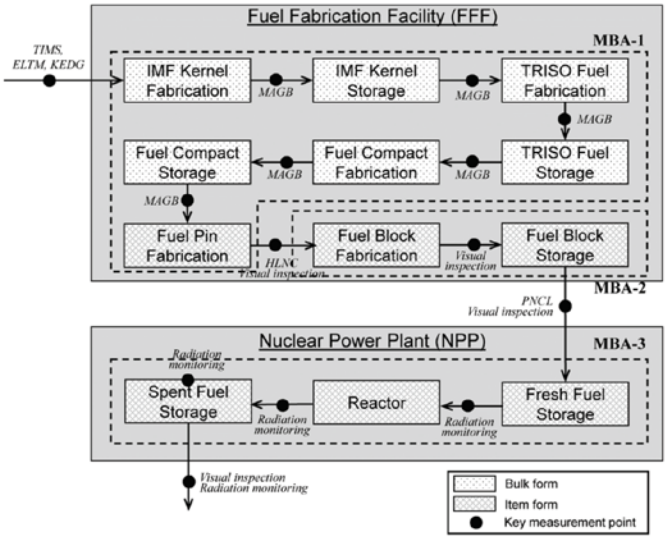

Fig. 1. Proposed material balance area design at the fuel fabrication facility and the nuclear power plant

TABLE II MUF and σ_{MUF} for various hold-up fractions in MBA-1

	Hold-up fraction [%]			
	0	1	2	3
MUF [SQ]	0.00	0.09	0.17	0.25
$3\sigma_{MUF}$ [SQ]	0.26	0.25	0.24	0.23
$3\sigma_{MUF}$* [SQ]	0.42	0.41	0.40	0.39
Expected diversion time [mo.]	2.4	2.4	2.5	2.6

REFERENCES

1. Takeshi Aoki, Sunil S. Chirayath, Hiroshi Sagara Takeshi AOKI et al., Transactions of the American Nuclear Society, Vol. 115, Las Vegas, NV, November 6–10, 2016

C.4 Principle validation of nuclear fuel material isotopic composition measurement method based on photo-fission reactions

Rei KIMUMRA, Hiroshi SAGARA and Satoshi CHIBA

In this paper, the feasibility of the photonuclear fission reaction is studied in terms of the concealed unknown form of highly enriched uranium. Based on the characteristics of photonuclear reaction, the robustness to gamma-ray noises could be expected because of the high threshold energy at nearly 5 MeV. The reaction is thus hardly affected by the gamma rays produced by the nuclide decay reaction or spontaneous fission reaction; the nuclide decay reaction has a gamma-ray energy of about 2.6 MeV, which is almost equal to the maximum gamma-ray energy of 208Tl, while the fission reactions produce very few gamma rays that are over the threshold energies [10]. These gamma rays do not dominate the photonuclear reaction. In the present method, the number of neutrons produced by the photo-fission reactions at several specific photon energies is measured. Only information on relative counts is needed for enrichment induction using the mathematical process. The present paper thus aims at proposing a new NDA technique principle and validating this principle through case studies involving numerical simulations.

This study validated the principle of the new NDA method based on the photonuclear reaction. The 11 MeV/6 MeV incident photon case showed good reproducibility of ^{235}U enrichment, with errors of less than 5% and 10% for the 1 and 10 mm target thickness cases, respectively. Furthermore, the present methodology estimated ^{235}U enrichment value with 8% accuracy when the nuclide had a 5% photo-fission cross section uncertainty. The reduction in the uncertainty of the predicted enrichment due to the photonuclear cross section uncertainty was confirmed by selection of appropriate incident photon energy.

Furthermore, detectability of the photo-fission reaction to utilize coincidence counting was investigated. In particular, when the counting time is 10 s, a photon source flux of 4 × 109 photon/s was estimated to keep less than 0.5% relative standard deviation of the ^{235}U enrichment value. This requirement of the photon flux is realizable in the next generation gamma-ray source.

In conclusion, the present isotopic composition measurement method has realizability. Additionally, we believe that the precision of the present method will be improved to give an uncertainty of less than 5% of the predicted value of ^{235}U enrichment when the photonuclear cross section uncertainty is improved to be less than 3% (**Fig. 1**). In the future, we plan to extend the present method to other areas, such as actual measurement techniques and multi-nuclide measurements.

Finally, we hope that this study will contribute to world peace.

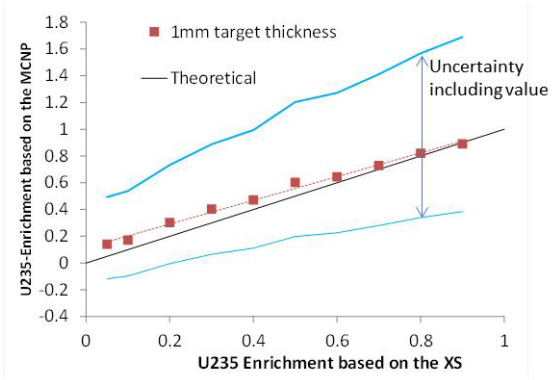

(a) The predicted value and its uncertainty of the ^{235}U enrichment based on the 10MeV/8MeV incident photon that has the Gaussian-shaped energy distribution

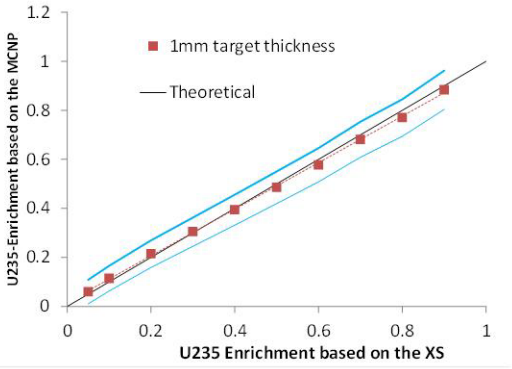

(b) The predicted value and its uncertainty of the ^{235}U enrichment based on the 11MeV/6MeV incident photon that has the Gaussian-shaped energy distribution

Fig. 1 The uncertainty included results of the predicted value of the ^{235}U enrichment

REFERENCES

1. Rei Kimuraa, Hiroshi Sagara and Satoshi Chiba, “Principle validation of nuclear fuel material isotopic composition measurement method based on photofission reactions” J. Nucl. Sci. Technol., Vol. 53, Issue 12, p. 1978-1987 (2016).

C.5 Mechanical Properties and Machinability of SiC/BN Composites with Oxide Additives

Katsumi YOSHIDA, Toyohiko YANO

1. Introduction

Silicon carbide (SiC) is one of the promising materials for structural applications at high temperatures since it shows high thermal and chemical stability, high stiffness, high hardness, high thermal conductivity, excellent oxidation, corrosion and wear resistance, high mechanical strength up to high temperature, low thermal expansion and good resistance to high-energy neutron irradiation.

In general, ceramic materials used as structural parts show low machinability because of their brittleness and high hardness. In order to reduce not only the difficulty in machining of ceramics but also the machining cost, machinability should be given to ceramics without decrease in their mechanical properties has been required. Hexagonal boron nitride (h-BN) has a similar crystal structure with graphite, and it shows good lubricity derived from its layered structure, and it has been used as a high temperature solid lubricant. A lot of studies on the fabrication of machinable ceramics with h-BN addition as a secondary phase, for example, Si_3N_4/BN, AlN/BN and SiC/BN composites, have been performed. In addition to the improvement of machinability, it is expected that the thermal shock resistance of ceramics is also improved by the addition of BN due to its low elastic modulus. Generally, BN addition to SiC inhibits the densification of SiC, and effective sintering additives, sintering method and sintering temperature must be selected for the densification of SiC/BN composites. Present authors paid attention to these sintering additives for the densification of SiC/BN composites. In our previous study, the authors reported that sinterability of SiC with BN was enhanced using Al_2O_3-Y_2O_3-CaO oxides as sintering additives at a relatively lower sintering temperature [1]. Therefore the authors tried to fabricated SiC/BN composite using Al_2O_3-Y_2O_3-CaO oxides as sintering additives by hot-pressing.

In this study, h-BN with different particle sizes were added to SiC, and SiC/BN composites were fabricated by hot-pressing using Al_2O_3-Y_2O_3-CaO as sintering additives, and sinterability, mechanical properties and machinability of SiC/BN composites were investigated.

2. Experimental

2.1. Fabrication of SiC/BN Composites

Beta-SiC (Ultrafine, average particle size: 0.28 μm, Ibiden, Japan) and h-BN were used as the starting materials. Three kinds of h-BN powder with different particle sizes (average particle size: 3.0 μm, 0.7 μm, and 0.1 μm) were used in this study. The composition of h-BN in SiC/BN composite was 0, 5, 10 and 15 wt%. Alpha-Al_2O_3 (14 wt%), Y_2O_3 (4 wt%) and CaO (2 wt%) were added to the mixture of SiC and h-BN powder as the sintering additives. The powder was mixed by ball-milling for 24 h, and then dried with a rotary evaporator. After drying, the powder was crushed with an agate mortar, followed by sieving. After sieving, the powder was formed into a compact under a uniaxial pressure of 50 MPa. The green compact was hot-pressed at 1800°C for 1 h in Ar flow under a uniaxial pressure of 40 MPa.

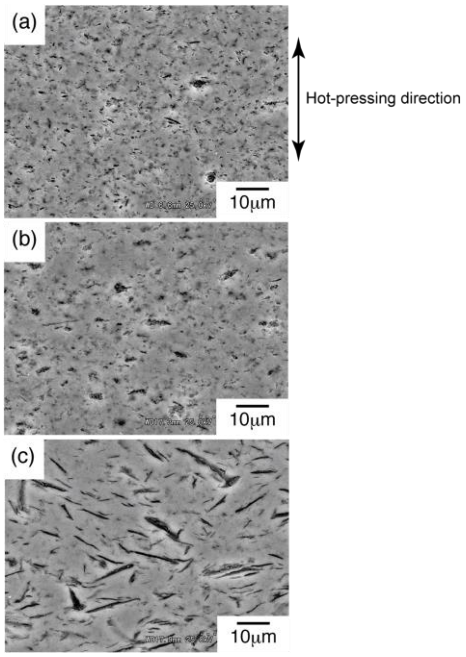

Fig. 1 SEM micrographs of microstructure of SiC/BN composite containing 10 wt% BN with the particle size of (a) 0.1 μm, (b) 0.7 μm and (c) 3.0 μm

2.2. Characterization and Evaluation of SiC/BN Composites

Bulk density of SiC/BN composites was measured by Archimedes' method. Theoretical density of SiC/BN composites was calculated from the composition of SiC, BN and oxide sintering additives. Crystalline phases of SiC/BN composites were identified by X-ray diffractometry (XRD). Bending strength and elastic modulus of SiC/BN composites were measured at room temperature by four-point bending test and strain guage method, respectively. Hardness of SiC/BN composite was evaluated by Vickers hardness test at room temperature according to JIS R1610. Applied load and holding time were 98 N and 20 sec, respectively. Fracture toughness (K_{Ic}) of SiC/BN composite was measured by indentation fracture method using Vickers hardness tester according to JIS R1607. Applied load and holding time were 98 N and 20 sec, respectively. Machinability of SiC/BN composites was evaluated by

cutting test and grinding test. In cutting test, the time required to cut the sample completely was measured. The rotation rate of blade in cutting test was 26.4 m•min^{-1}. Rectangular bars of SiC/BN composite with the size of 3^t x 4^w x 34^l mm^3 were used for cutting test. The sample was cut in the direction of the thickness i.e. in hot-pressing direction. In grinding test, weight change of the sample after grinding for 20 min was measured. The rotation rate of grinding disk and applied load to the sample during grinding were 28.5 m•min^{-1} and 5.8 x 10^4 Pa, respectively. Contact area of SiC/BN composite to grinding disk was 68 mm^2. Microstructure of SiC/BN composites and crack propagation after indentation in the composites were observed by scanning electron microscope (SEM).

3. Results and Discussion

3.1 Characterization of SiC/BN Composites

XRD analysis indicated SiC/BN composite mainly consisted of β-SiC and h-BN. Diffraction peaks corresponding to α-SiC formed by β-α phase transformation during sintering were also observed in XRD patterns. In addition, α-Al_2O_3 and $Y_3Al_5O_{12}$ (YAG) phases derived from sintering additives existed in SiC/BN composites.

Relative density of monolithic SiC was 95.7%. Relative density of SiC/BN composite using BN with the particle size of 0.1 μm was slightly lower than that of monolithic SiC. In the case of SiC/BN composites using BN with the particle size of 0.7 μm and 3.0 μm, their relative density was higher than that of monolithic SiC. The values were in the range from 96.6 to 97.2%.

SEM micrographs of microstructure of SiC/BN composites containing 10 wt% BN were shown in Fig.1. Black parts indicated BN particles in these SEM micrographs. BN particles were well dispersed in the composite, and it seemed that plate-like BN particles were almost oriented perpendicular to hot-pressing direction. There were few pores in the SiC/BN composites and the composites were almost dense. These results suggested that the addition of BN to SiC did not inhibit the sinterability of SiC, i.e. the sinterability of the composite was enhanced using Al_2O_3-Y_2O_3-CaO as sintering additives.

3.2 Mechanical Properties of SiC/BN Composites

Bending strength of monolithic SiC was approximately 600 MPa. In the case of SiC/BN composite using BN with the particle size of 0.1 μm, its bending strength ranged from 490 to 580 MPa. Bending strength of SiC/BN composites using BN with the particle size of 0.7 μm or 3.0 μm gradually decreased with an increase in BN content from 450 and 430 to 370 and 280 MPa, respectively. Bending strength of the SiC/BN composites decreased with an increase in the amount of BN addition and particle size of BN. This result implies that the bending strength of SiC/BN composites depends on not only the amount of BN addition but also particle size of BN.

Elastic modulus of monolithic SiC was 380 GPa, and that of SiC/BN composites almost linearly decreased with the amount of BN addition. The elastic modulus of h-BN was reported to be 83 GPa, and the elastic modulus of the composites was much lower than that of SiC. SiC/BN composite containing BN with smaller particle size showed slightly higher elastic modulus.

Vickers hardness of monolithic SiC was 17.1 GPa, and that of SiC/BN composites almost linearly decreased from the value of monolithic SiC as the amount of BN addition increased because Vickers hardness of h-BN (1.96 GPa) was much lower than monolithic SiC. In the case of submicron-sized BN (0.1 μm or 0.7 μm) addition, Vickers hardness of SiC/BN composites with the same amount of BN addition showed a similar value independent of BN particle size. Vickers hardness of SiC/BN composite using micron-sized BN (3.0 μm) powder was lower than that of the composites using submicron-sized BN powder. BN particle size strongly affected the Vickers hardness of SiC/BN composites in addition to the amount of BN addition.

Fracture toughness of monolithic SiC was 3.5 MPa•m$^{1/2}$. With 5 wt% BN addition, fracture toughness of SiC/BN composite using micron-sized BN powder was slightly higher than that of monolithic SiC, and the value was 3.7 MPa•m$^{1/2}$. SiC/BN composites using 5 wt% submicron-sized BN powder showed much higher fracture toughness than monolithic SiC, and their fracture toughness was ranged between 4.2 and 4.3 MPa•m$^{1/2}$. These values are comparable with SiC/BN nanocomposites reported in references. With BN additions more than 10 wt%, fracture toughness of SiC/BN composites using micron-sized and submicron-sized BN powder decreased to 3.2 MPa•m$^{1/2}$ and 3.6-3.9 MPa•m$^{1/2}$, respectively. Fracture toughness of SiC/BN composite with submicron-sized BN powder was

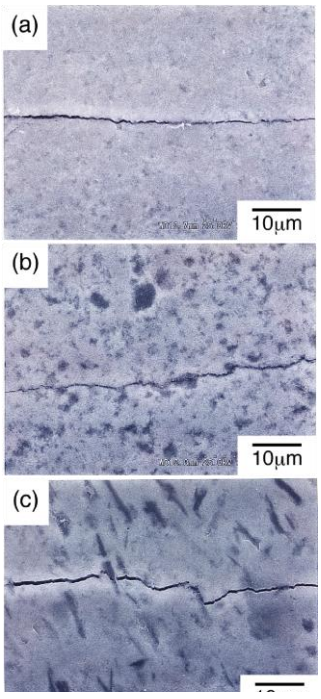

Fig. 2 SEM micrographs of crack propagation in (a) monolithic SiC and SiC/BN composite containing 10 wt% BN with the particle size of (b) 0.7 μm and (c) 3.0 μm.

still higher than that of monolithic SiC. This result suggested that smaller amount of BN powder and smaller BN particle size contributed to higher fracture toughness of SiC/BN composites.

Figure 2 shows SEM micrographs of crack propagation in SiC/BN composites containing 10 wt% BN. While a crack propagated almost straight in monolithic SiC, a crack deflected around or propagated along BN particles in SiC/BN composites. However, fracture toughness of the SiC/BN composite with micron-sized BN powder showed lower value. This reason is explained as follows; the crack length in the SiC/BN composite became longer than that in SiC/BN composite with submicron-sized BN powder because the crack propagated easily along micron-sized BN particles. For this reason, the fracture toughness of the SiC/BN composite with micron-sized BN powder was lower than that of monolithic SiC or SiC/BN composite with submicron-sized BN powder.

3.3 Machinability of SiC/BN Composites

Machinability of monolithic SiC and SiC/BN composites containing BN with the particle size of 0.7 and 3.0 μm was evaluated by grinding test and cutting test. Weight loss of monolithic SiC during grinding test was approximately 0.6 $mg•mm^{-2}•sec^{-1}$. For SiC/BN composites with 5 wt% BN addition, their weight loss during grinding was 1.6 - 1.8 times larger than that of monolithic SiC, and weight loss of the SiC/BN composites using BN powder with the particle size of 0.7 μm and 3.0 μm was 1.0 $mg•mm^{-2}•sec^{-1}$ and 1.1 $mg•mm^{-2}•sec^{-1}$, respectively. With 10 wt% BN additions or more, grinding weight loss of SiC/BN composite using BN with the particle size of 0.7 μm slightly increased up to 1.6 $mg•mm^{-2}•sec^{-1}$, and this value was 2.6 times larger than that of monolithic SiC. Grinding weight loss of SiC/BN composite using BN with the particle size of 3.0 μm significantly increased up to 8.3 $mg•mm^{-2}•sec^{-1}$. This value was much larger than that of monolithic SiC.

Cutting time for monolithic SiC was 1480 sec, and that for SiC/BN composites containing 5 wt% BN with the particle size of 0.7 μm was almost the same as that for monolithic SiC. With 10 wt% BN additions or more, cutting time for the SiC/BN composites using BN with the particle size of 0.7 μm linearly decreased to 490 sec. This cutting time was a third of that for monolithic SiC and SiC/BN composite with 5 wt% BN addition. For SiC/BN composites using BN with the particle size of 3.0 μm, the composite with 5 wt% BN addition needed 1100 sec for cutting. It was shorter than monolithic SiC and SiC/BN composite containing 5 wt% BN with the particle size of 0.7 μm. With 10 wt% BN additions or more, the time needed to cut the SiC/BN composites using BN with the particle size of 3.0 μm linearly decreased to around 300 sec. It was a fifth of those for monolithic SiC and SiC/BN composite with 5 wt% BN addition. The results of cutting and grinding test suggested that the addition of BN to SiC was effective for decreasing the time for cutting and for increasing the weight loss during grinding, i.e. for the improvement of the machinability. In addition, cutting time and grinding weight loss of SiC/BN composite depended on the amount of BN addition and BN particle size. In this study, dense SiC/BN composites using Al_2O_3-Y_2O_3-CaO sintering additives with higher machinability and good mechanical properties were successfully obtained. Based on the results, material design of dense SiC/BN composite with both excellent mechanical properties and machinability using Al_2O_3-Y_2O_3-CaO oxides as sintering additives is proposed. The addition of BN with the particle size of 3.0 μm to SiC resulted in good machinability and sinterability. However, the SiC/BN composite exhibited low fracture toughness and bending strength. In the case of SiC/BN composite containing BN with the particle size of 0.7 μm, it showed good sinterability and mechanical properties. Furthermore, its cutting time and Vickers hardness was effective for good machinability. However, weight loss of the SiC/BN composite during grinding which also contributes to good machinability seemed to be small. Based on this consideration, the particle size of BN in SiC/BN composite using Al_2O_3-Y_2O_3-CaO sintering additives with much higher machinability and excellent mechanical properties should be a little bit larger than 0.7 μm.

4. Conclusion

SiC/BN composites were fabricated by hot-pressing using h-BN with different particle sizes and Al_2O_3-Y_2O_3-CaO as sintering additives, and the effect of BN particle size on sinterability, mechanical properties and machinability of SiC/BN composites was investigated. Dense SiC/BN composites were achieved by the use of Al_2O_3-Y_2O_3-CaO oxides as sintering additives. Bending strength of the SiC/BN composites decreased with an increase in the amount of BN addition and particle size of BN. Elastic modulus and Vickers hardness of SiC/BN composites almost linearly decreased from the values of monolithic SiC with the amount of BN addition. BN particle size strongly affected the Vickers hardness of SiC/BN composites in addition to the amount of BN addition. Fracture toughness of SiC/BN composite using submicron-sized BN powder was higher than that of monolithic SiC. However, fracture toughness of SiC/BN composites with micron-sized BN powder addition was not improved. This result was explained by crack propagation and deflection. It was suggested that smaller amount of BN powder and smaller BN particle size contributed to higher fracture toughness of SiC/BN composites. From the results of cutting and grinding test, the machinability of SiC/BN composite depended on the amount of BN addition and its particle size. In this study, dense SiC/BN composites using Al_2O_3-Y_2O_3-CaO sintering additives with higher machinability and good mechanical properties were successfully obtained.

References

1. K. Yoshida, M. Imai, T. Yano, *Key Eng. Mater.*, **164-165**, 135-138 (1999).

C.6 Transformation of nanodiamonds into onion-like carbon under IR heating

Anna GUBAREVICH

1. Introduction

Diamond is a widely used material, and due to its high stability at high temperatures and high radiation resistance in particular it has been applied as nuclear particles detector in nuclear energy field. With the development of nanotechnology, effect of nanostructure on the properties of conventional materials is considered to be an important issue. That is especially important for carbon materials, where classical allotropes, diamond and graphite, give an amazing diversity of structures at nanolevel, such as graphene and carbon nanotubes, to mention a few.

This research is focused on diamond nanoparticles (or nanodiamond (ND) hereafter) and their transformation into onion-like carbon (OLC), which is a characteristic transformation between carbon nanostructures. OLC is a carbon nanomaterial with a characteristic structure of concentrically arranged curved graphene layers. It has a moderately high specific surface area (300~500 m^2/g) and high electrical conductivity provided by its graphitic structure. Due to such combination of properties OLC has been gaining an increasing attention as an electrode material in high power energy storage devices (electric double layer capacitors) and as an attenuating material in electromagnetic shielding applications.

It is known that ND transforms into OLC under thermal annealing for several hours in an inert atmosphere or vacuum at temperatures 1600-1800 ^{0}C. In the present research transformation of ND into OLC under short-time infrared (IR) heating was investigated.

2. Experimental

IR heating experiments have been conducted using a double-type infrared gold image furnace (ULVAC SINKU-RIKO MR 39H/D), which has two halogen lamps and two gold ellipsoidal reflectors arranged to make a focal point in the center part. Commercially available ND powders were dried at 80 ^{0}C in vacuum for 24 hours before use. About 20-25 mg of ND powder was placed in a platinum holder, which was set at the focal point of the gold reflectors. The maximum temperature was 1600 ^{0}C, heating rate in the range of 800-1600 ^{0}C was 40 ^{0}C/min, and holding time at the maximum temperature was 1 minute. Temperature was controlled with an S-type thermocouple. Heating was carried out under argon flow (80 ml/min). Afterwards, the specimen was cooled down to the room temperature in the argon flow.

The structure of the virgin ND and synthesized OLC powders was investigated using an energy-filtering transmission electron microscope (EF-TEM) (Leo, model EM-922) with an Omega-type energy filter. The electron acceleration voltage was 200 kV. The sample for TEM observation was prepared by dispersing the carbon specimens in alcohol and pipetting them onto holey carbon support films.

Chemical bonding in virgin ND and OLC was characterized by UV laser Raman spectroscopy (wavelength 244 nm [5.1 eV]). UV excitation provides better sensitivity ratio of sp^3/sp^2 carbon comparing to visible excitation. To avoid damage to carbon materials under UV irradiation, the signals from about 50 points, obtained by moving the sample by 20 μm increments in the XY plane, were collected and averaged. This method provides a high signal-to-noise ratio for the short irradiation time of each investigated area.

Specific surface area of OLC powders was measured by a static manometric adsorption of nitrogen at cryogenic temperature (77 K) using Belsorp 28SA apparatus. The powders were outgassed at 300 ^{0}C for 2 hours directly before measurement. Calculation of the specific surface area was done according to the Brunauer-Emmet-Teller (BET) method. The value of molecular cross-sectional area for nitrogen molecule was taken as 0.162 nm^2.

3. Results

2.1. Structure change during heat treatment

Figure 1 shows zero-loss bright-field TEM images of the virgin ND powder (a) and synthesized in the infrared furnace OLC (b). It can be seen that starting ND powder consists of aggregated round-shaped particles with size between 4 and 10 nm. No amorphous carbon is observed. As can be confirmed from the Fig. 1 (b), ND transformed to OLC in a result of the heating in the infrared furnace. It is seen clearly that the synthesized OLC consists of round-shaped particles with concentrically arranged graphitic structure. The size of the particles is about 5-8 nm and some particles reach 10 nm in diameter. The majority of particles have a shape close to spherical, and lager particles have a tendency to adopt a polyhedral shape. Number of concentrically arranged graphitic layers in a single particle varies from 5 and 10 and depends on the particle size. The distance between graphitic layers is estimated to be 0.33 nm, which is close to the interplanar distance in graphite (0.3376 nm). Almost no amorphous carbon or other carbon forms is observed.

2.2. Change in carbon chemical bonding

UV Raman spectra of ND and OLC are shown in Fig. 2. The UV spectrum of ND has following features on the strong photoluminescence background: the characteristic peak of nanodiamond phase at 1323 cm^{-1} and a low asymmetric band around 1560-1600 cm^{-1}. The nanodiamond peak is broadened and downshifted with respect to the bulk diamond characteristic peak position of 1332 cm^{-1}. The shift can be explained by the phonon confinement effect due to the nanosize of the particles.

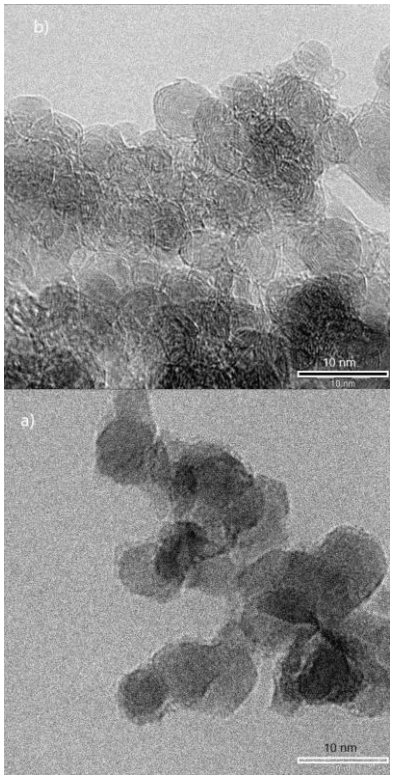

Fig. 1 EF-TEM images of ND (a) and OLC (b).

Broadening of the peak can be related to the small size of nanodiamond crystals too. The band at 1560 – 1600 cm^{-1} is connected to the sp^2-bonded carbon and surface chemical groups such as hydroxyl and carbonyl.

UV Raman spectrum of OLC has a single dominant peak with maximum at 1564 cm^{-1}, which can be interpreted as downshifted G-band. G-band is a characteristic feature of graphitic carbon and its standard position is at 1592 cm^{-1}. Considerable downshift of the G-band can be explained by the curvature of graphitic layers in OLC. No peak of sp^3 carbon related to diamond structure was observed.

2.3. Specific surface area

Figure 3 shows nitrogen adsorption and desorption isotherms of OLC powder, where volume of adsorbed nitrogen (V_a, standard temperature and pressure) is shown as a function of partial pressure (p/p_0). The adsorption isotherm belongs to the Type II according to the 2015 IUPAC classification. This isotherm describes reversible physisorption on macroporous or non-porous materials. The BET surface calculated from the isotherm was 311 m^2/g. The estimated pore volume was 0.65 cm^3/g.

4. Discussion

Experimental results of the present work show that under conditions of IR heating ND completely transformed to OLC at 1600 ^{0}C. The structure of OLC is well formed, and no amorphous carbon was confirmed from TEM observations or Raman measurements. Compared to conventional methods of OLC synthesis, which usually require hours, the infrared heating permits to obtain OLC in minutes.

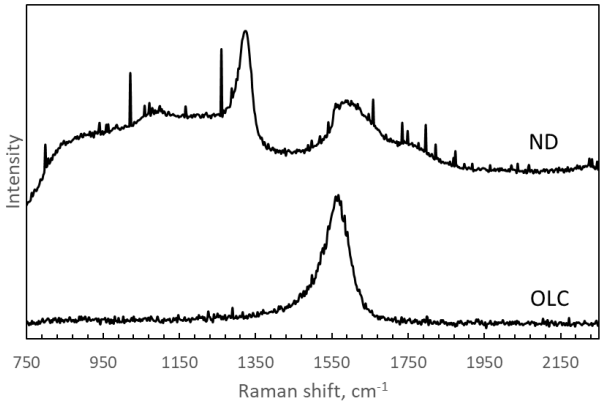

Fig. 2 UV Raman spectra of ND and OLC.

Such fast transformation kinetics requires additional consideration, since the maximum temperature applied in our experiments is 1600 ^{0}C or 1873 K, which is lower than the Debye temperature of diamond (1910 K). Transformation of ND to OLC is a kind of graphitization process of diamond or transformation of sp^3 into sp^2 bonded carbon. It is known that there exist at least two regimes with different kinetic parameters in the graphitization process of diamond, low-rate transformation at low temperatures and high-rate transformation at high temperatures, which are divided by the Debye temperature of diamond. Further research on kinetics of ND to OLC transformation in the vicinity of the Debye temperature and study on the effect of IR irradiation spectrum is necessary.

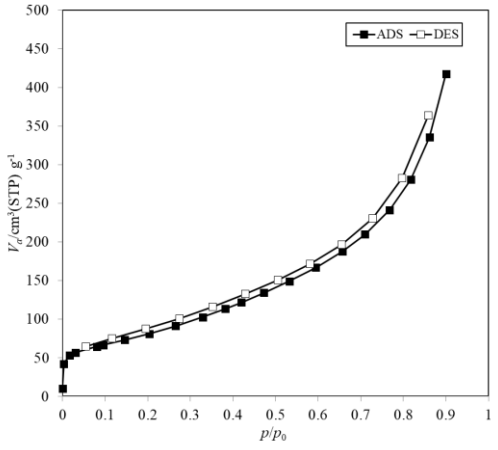

Fig. 3 Adsorption and desorption isotherms of OLC powder.

5. Conclusions

In this study it was shown that ND transformed into OLC under IR heating for a short duration. Mechanism of the fast transformation is worth to investigate in future.

Reference

1. A.V. Gubarevich, H. Wada, and O. Odawara: III International Conference on Nonisothermal Phenomena & Processes: From Thermal Explosion Theory to Structural Macrokinetics (NPP-2016), November 28-30, Chernogolovka, Russia (2016).

D. Advanced Medical Application Division

D.1 Development of Experimental Devices for Heavy Ion–Hot Matter Interaction Research

Yoshiyuki OGURI, Jun-ya KOBAYASHI, Fumisato GAMOU, Yuta SHUTOU, Hitoshi FUKUDA

1. Time-resolved velocimeter based on laser refraction

A time-of-flight laser velocimeter was designed for measurement of shock speed in an electromagnetic shock tube for production of dissociated hydrogen gas targets for heavy ion interaction experiments[1]. Fig. 1 illustrates the system setup (J. Kobayashi, Master thesis, Tokyo Institute of Technology (2018)). To eliminate the electromagnetic noise due to the plasma discharge in the tube, the laser beam was transported from a 633-nm CW He-Ne laser source (17 mW; 30995, Research Electro-Optics) placed at a distant position from the test section of the tube using a single-mode optical fiber. The passage of the shock is detected by observing the refraction of the laser beam by the shock. To maximize the detection sensitivity, the diameter of the laser beam in the shock tube was reduced to ≈ 100 μm by a lens system. Refraction of the laser is detected by a ϕ0.8-mm fast Si PIN photodiode (S5972, Hamamatsu photonics) at 1 m behind the shock tube.

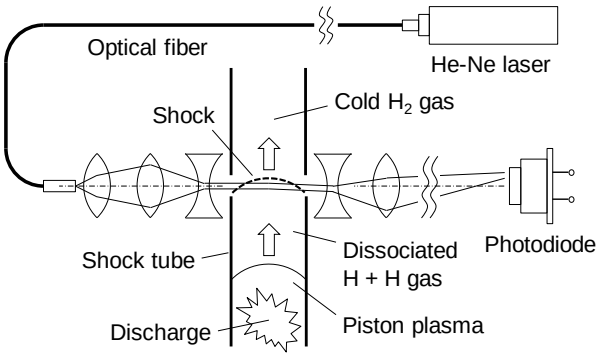

Fig. 1 Experimental setup for the laser velocimeter.

The shock detection performance was tested by using a simulated target consisting of a spectrophotometer glass cell (width = 10 mm, length = 20 mm) filled with a 66wt% standard sucrose solution (refractive index n = 1.456) and a quartz-glass (n = 1.457) cylindrical lens (10 mm × 10 mm, curvature radius = 9.2 mm). The cylindrical lens was put in the solution to simulate the curved shock in front of the piston plasma. The measured displacement of the laser spot position at the detector due to the passage through the lens–solution interface was ≈ 4 mm. The displacement by the actual shock expected from this result is ≈ 0.1 mm, which is enough to be detected by the present setup.

2. Fast beam kicker based on high-voltage MOSFET switches

A fast beam kicker was constructed and tested for time-resolved MeV heavy ion–hot matter interaction experiments. Fig. 2 shows the setup and the principle of the experiment (F. Gamou, Graduation thesis, Tokyo Institute of Technology (2018); Y. Shutou, Graduation thesis, Tokyo Institute of Technology (2018)). The kicker consists of three pairs of parallel metallic plates. Pulsed beams with arbitrary durations can be produced by adjusting the timing of fast high-voltage MOSFET switches (HTS50-05, Behlke; ON time = 100 ns (fixed)). The pulsed beam waveform was measured by a time-resolved detector consisting of a plastic scintillator (NE-102A, Nuclear Enterprise; rise time = 0.9 ns, decay time = 2.4 ns) and a photomultiplier tube (R647, Hamamatsu photonics; rise time = 2.1 ns).

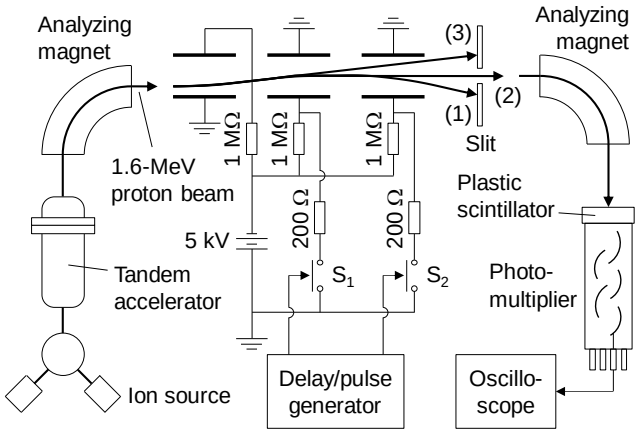

Fig. 2 Setup and the principle of the fast beam kicker experiment: (1) Beam-OFF (S_1 = OFF, S_2 = OFF), (2) Beam-ON (S_1 = OFF, S_2 = ON), (3) Beam-OFF (S_1 = ON, S_2 = ON).

By using a 1.6-MeV proton beam from the tandem accelerator, we have so far obtained a pulse duration of 34 ns (FWHM). This value should be further reduced in order to perform actual heavy ion interaction experiments with shock-driven dissociated hydrogen gas targets, of which the expected duration is ≈ 100 ns.

Acknowledgment

Naoyuki Tsuruoka is gratefully acknowledged for his help in preparation of the experimental devices.

References

1. K. Kondo and Y. Oguri: Velocity Evolution of Electro-Magnetically-Driven Shock Wave for Beam–Dissociated Hydrogen Interaction Experiment; *J. Phys.: Conf. Ser.*, Vol. **688**, 012052 (2016).

D.2 Generation of human induced pluripotent stem cells and neural stem cells for DNA damage response study

Mikio SHIMADA

1. Introduction

Genome DNA is exposed to many environmental factors including ionizing radiation, ultraviolet, chemicals and metabolic products. DNA repair machinery is important for genome maintenance and protection from these environmental factors in all organs. Defect of DNA repair leads to severe disease such as inherited disease and cancer. It is known that stem cells including embryonic stem cells and organs specific stem cells such as neural stem cells have different DNA repair machinery compared with somatic cells. However, detail of molecular mechanism remains unclear. In this study, to investigate molecular mechanism and transcriptional control of DNA repair machinery in stem cells, we established induced pluripotent stem (iPS) cells from skin fibroblast and neural stem (NS) cells from iPS cells. After ionizing radiation (IR) exposure to these cells, DNA damage response (DDR) was analyzed using western blotting method.

2. Results

2.1. Generation of induced pluripotent stem cells

NB1RGB human skin fibroblast was obtained from RIKEN bio resource center and used for reprogramming to iPS cells using RNA reprogramming method. After daily transfection of mRNA cocktail including OSKMNL (Oct4, Sox2, Klf4, cMyc, Nonog, Lin28) reprogramming factors, EKB (E3, K3, B18) immune evasion factors and Non-modified microRNAs for 4 times, NB1RGB cells were cultured with Nutristem XF/FF culture medium for 5-7 days. And then, iPSC like colonies were picked up into iMatrix511 pre-coated 24 well plates (Fig1). ROCK inhibitor Y27632 (Woko chemicals) was used for single cell expansion. To identify pluripotency, iPS cells were analyzed with alkaline phosphatase staining and immune-stained with pluripotent stem cells marker (OCT4, Nanog, KLF4, SOX2 antibodies)

2.2. Generation of neural stem cells

iPS cells generated from NB1RGB skin fibroblast was used for generation of NS cells. We used direct PSC neural induction medium (GIBCO) and followed manufacture protocol. iPS cells were cultured in iMatrix511 pre-coated 60mm dish with Nutristem XF/FF culture medium. Next day, iPS cells were cultured with PSC neural induction medium for 7 days, and then cells were expanded as passage 1(P1) cells (Fig 2). ROCK inhibitor Y27632 was used for single cell expansion. NS cells were immune-stained with neural stem cell markers, PAX6, SOX2, PAX2, Nestin and GFAP.

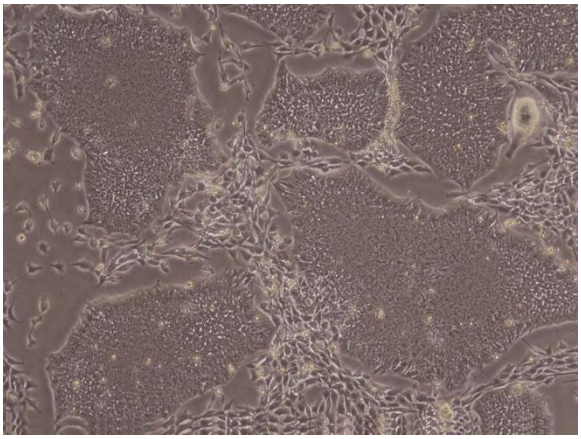

Fig. 1 iPS cells were derived from human skin fibroblast NB1RGB. Picture is microscopic observation.

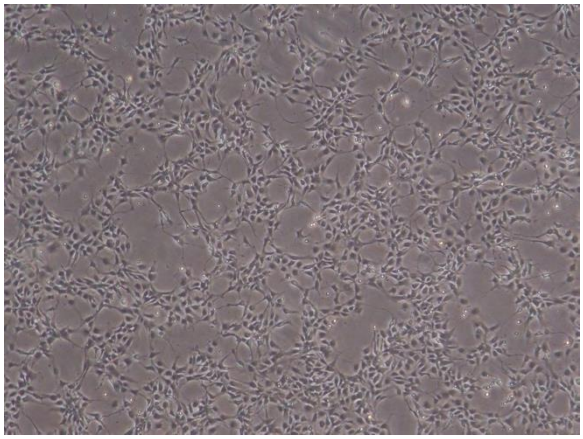

Fig. 2 NS cells were derived from NB1RGB iPS cells. Picture is microscopic observation.

Acknowledgment

Author thanks to Dr. Matsumoto laboratory member for critical discussion and Mr. Isao Yoda for technical assistance.

Reference

1. M. Shimada, et al.: 60th Annual meeting of Japanese association of Radiation Research, October 24-25, Chiba, Japan, (2017).

E. Fundamental Research Division

E.1 Study for nuclear fission and its application

Chikako ISHIZUKA and Satoshi CHIBA

1. Introduction

Nuclear fission has been studied for eighty years since its discovery. However, we still cannot explain the whole property of nuclear fission even of ^{236}U with sufficient predictive power, although empirical models have been applied to practical use. Such practical models may work well in the case of n-induce fission of ^{235}U and ^{239}Pu. On the other hand, in order to develop Accelerator-driven Systems (ADS) and Fast Reactors (FR), and to reduce the TRU wastes, we need high quality data on minor actinides (MA). Experiments to obtain fission data for MA and long-lived fission products (LLFP) have been performed in various facilities. But it is still difficult to cover whole fission data, such as fission product mass distributions (FFMDs), thermal energy (total kinetic energy; TKE), prompt and delayed neutrons, and decay heat from the fission products. We are working on the reduction of poisonous nuclear wastes by studying the whole mechanism of nuclear fission process from scission to β-decay, and by developing high-quality nuclear data. In our laboratory, we have also investigated the influence of nuclear data on the decommissioning costs.

2. Fundamental studies for nuclear fission

In our laboratory, we have studied the fundamental mechanism of nuclear fission at low energies using various nuclear-physics theories such as Multidimensional Langevin models, Anti-symmetrized Molecular Dynamics model, and Time-dependent Hartree Fock model. Nuclear fission is the motion of a many-body quantum system. It is still very difficult to describe the whole feature of a nuclear fission process with a single model. Therefore, we have adopted different models depending on our purpose. In this section, we briefly summarize these models we have developed.

2.1. Multidimensional Langevin models

Langevin models can reproduce and predict not only the fission product mass yields but also the total kinetic energies of the fission fragments of actinides. In the Lanvin model, a nuclear fission process is regarded as a time-evolution of the nuclear shape of a fissioning nucleus following the equation of motion under the friction force and the random force. Such equation of motion is called the Langevin equation. In the three dimensional model, in general, macroscopic transport coefficients have been used for simplicity. But the friction force should be changed depending on the potential surface, for example. We examined the potential dependence of the transport coefficients of the Langevin equation with the potential independent macroscopic transport coefficients and the potential dependent microscopic transport coefficients derived from the linear response theory [1]. Fig. 1 shows the systematic study for the averaged total kinetic energies (TKEs) of various actinides. The three dimensional Langevin model with the potential dependent microscopic transport coefficients showed the better reproducibility of the Viola's systematics lines based on the experimental data. However, three dimensional Langevin model constraints the nuclear shapes of fission fragments. We also have extended our Langevin model from three dimensional to four dimensional for more precise nuclear-shape description.

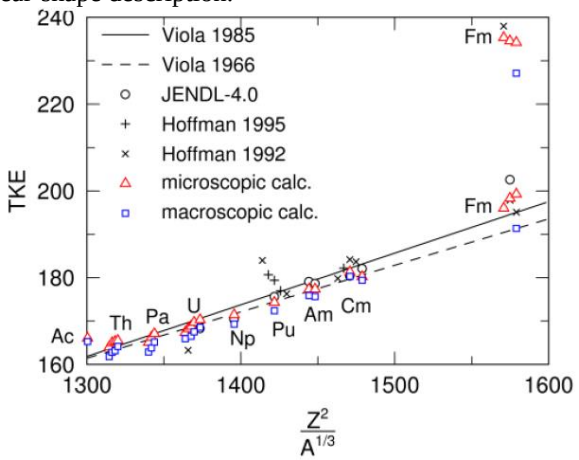

Fig. 1 Averaged TKEs of actinides

2.2. Anti-symmetrized Molecular Dynamics (AMD) model

The Langevin models cannot directly provide the spins of fission fragments and the division of nuclear excitation energy among fission fragments. Those quantities has been investigated by the Quantum molecular dynamics (QMD). However, a nucleus is a quantum many-body system of a fermions such as protons and neutrons. Fermions is anti-symmetric under particle exchange. Therefore we need to extend the QMD to include such anti-symmetrization for more precise description of nuclear fissions, though such extension had not been performed for long time due to the difficulty of the model. Such model with the anti-symmetrization is called the Anti-symmetrized Molecular Dynamics (AMD), which is a very powerful model to describe both nuclear reactions and nuclear structures. We have developed the AMD for the microscopic study of nuclear fission mechanisms and applied it to the ^{236}U fission for the first time. The spin analysis for the AMD results is in progress.

2.3. Time-dependent Hartree Fock (TDHF) model

In the standard Langevin models, the friction force is provided by the potential derivatives with a macroscopic coefficient evaluated the one-body dissipation model. In order to valid such friction force, we have performed the

Time-dependent Hartree Fock (TDHF) calculations. The TDHF model can derive the friction coefficient considering all nucleon degree of freedom. We evaluated the coefficient of the friction force in $^{16}O + ^{16}O$ collisions.

3. Beta decay of fission products

After prompt neutrons and gammas emitted from the fission fragments, the beta-decays of these nuclei will occur. Neutrinos produced by the beta-decay process play a significant role in the surveillance and in-service inspection in nuclear power plants. In our laboratory, we have studied the anti-neutrino spectrum from aggregate fission products beta-decays based on the gross theory [2] as shown in Fig.2. The red dashed line in Fig. 2 is the calculation result of improved version of our gross theory. In that calculation, we used fully theoretical spectrum except for ^{92}Rb which is the experimental data from Zakari. Thus, we succeeded in developing power tool to analyze the antineutrino spectrum from nuclear reactors because the improved gross theory can precisely explain the experimental data.

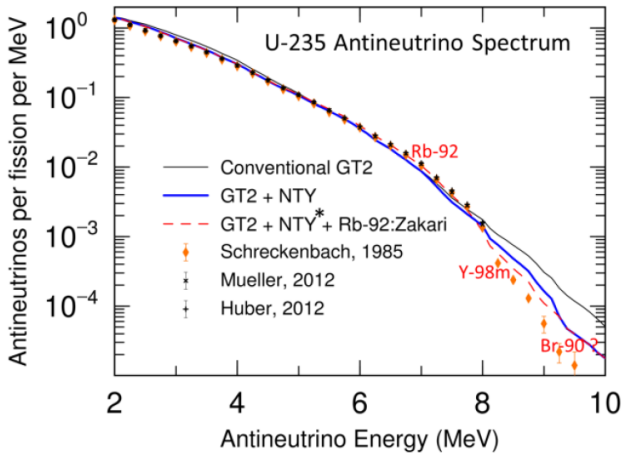

Fig. 2 Antineutrino energy spectrum from ^{235}U sample

4. Evaluation of nuclear data

High precision nuclear data is necessary to economically evaluate the total heat from the fission products and their toxicity. We have developed a new system to extract experimental data on the fission product yields (FPYs) from the open databases such as EXFOR and CINDA for the development of nuclear data based on original evaluations. Our new system can gather and analyze 6340 experimental data on ^{235}U(n,f) reactions as of the end of March in 2016. Collected data have been analyzed by comparison with major theoretical models such as TALYS, CFFP FREYA as shown in Fig. 3. We found that all evaluated major libraries adopted the sharp peak at A=134 in several experimental FPYs of ^{235}U(n_{th}, f) reactions. We also found that all theoretical models cannot reproduce the peak heights of light and heavy fragments and the peak at A=134. Thus, our analysis based on the experimental data can elucidate problems which have not been well discussed yet.

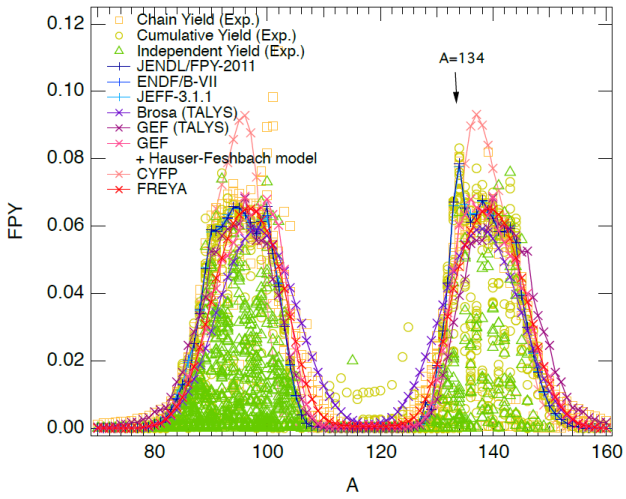

Fig. 3 Comparison of ^{235}U(n_{th},f) FPY

5. Application of developed nuclear data to the transmutation and decommissioning

Major nuclear data libraries such as JENDL-4.0 contains ambiguity due to the experimental data and human errors during coding process. In our laboratory, we have investigated the suspicious nuclear data, and have examined its influence on transmutation and decommissioning. For example, we found the possibility of 20% overestimation in the cross section of thermal neutron caption on ^{102}Ru of JENDL-4.0, where Ru-isotopes affect the transmutation efficiency using nuclear reactors. We also evaluated the ambiguity in the fission neutron spectrum in JENDL-4.0 which may influence the activation of reactor structural materials. Nuclear data is the most basic data for nuclear reactors. Therefore we have to pay much attention to its precision, and develop better nuclear data. For this aim, we have studied nuclear fission from the fundamental mechanism.

Acknowledgment

This work was supported by the grant “Comprehensive study of delayed-neutron yields for accurate evaluation of kinetics of high-burn up reactors” entrusted to Tokyo Institute of Technology by the Ministry of Education, Culture, Sports, Science and Technology of Japan (MEXT), and “Development of prompt-neutron measurement in fission by surrogate reaction method and evaluation of neutron-energy spectra” entrusted to Japan Atomic Energy Agency by MEXT. The authors also thank the WRHI (World Research Hub Initiative) program of Tokyo Institute of Technology, and IAEA CRP on beta-delayed neutrons (F41030).

Reference

1. M. D. Usang M. D. Usang, F. A. Ivanyuk, C. Ishizuka, and S. Chiba, Physical Review C **94**, 044602 (2016).
2. T. Yoshida, T. Tachibana, N. Hagura, S. Chiba, Progress in Nuclear Energy **88**, 175 (2016).

E.2 The Spectroscopic Characteristics of Nitrogen Molecule Puffed onto Cold Expanding Argon Arc Jet Plasma

Hiroshi AKATSUKA and Atsushi NEZU

High-speed arc-jet plasma flow is now drawing attention in many engineering applications, for example, divertor plasma of nuclear fusion reactors and plasma thrusters. In these areas, it is fundamentally crucial to examine the effect of gas-puff onto the high-speed plasma, since various kinds of excitation energy of many atomic and molecular states will be relaxed into other states, based on collisional processes, in the interactions between the plasmas and the puffed gases. We have also studied spectroscopic characteristics of nitrogen arc jet plasma. Concerning the spectroscopic measurement, the radiation from the plasma is observed along the direction perpendicular to the jet axis through the gaps of the magnets. We can find almost no signal of the nitrogen molecular band spectra without N_2 puffing, while we can detect them significantly with N_2 gas puffing onto the plasma jet in the downstream region even when the position of the puffing is far away from the anode nozzle of the plasma generator. Figure 1 schematically shows the experimental setup, including plasma jet generator, optical fiber terminal assembly to collect radiation and the gas puff piping system. Then, we analyzed the N_2 first positive system (1PS) and N_2 second positive system (2PS) by optical emission spectroscopy (OES) when N_2 gas is puffed onto the Ar plasma jet. We surveyed the vibrational (T_v) and rotational (T_r) temperatures of the B $^3\Pi_g$ and C $^3\Pi_u$ states of N_2. We determined those temperatures by fitting the calculated spectrum with that measured experimentally.

Figure 2 shows T_v and T_r of N_2 B and C states obtained from 1PS and 2PS, respectively. It was found that $T_v \approx 0.28 - 0.35$ eV and $T_r \approx 0.038 - 0.050$ eV for the B state (v =7, 8 and 9), whereas $T_v \approx 0.18$ eV and $T_r \approx 0.20$ eV for the C state (v = 0 and 1), which show almost the same value even when a gas puff rate is modified a little. Since the electron temperature in the observed area is about 0.4 eV, it is naturally considered that the N_2 C states are mainly produced by the resonant energy transfer from the Ar metastable to the N_2 ground state. Then, it is considered that similar values of T_v and T_r of the C state are the approximate value of the Ar gas temperature. On the other hand, the vibrational temperature of the B state is much higher than its rotational temperature, which is rather close to the room temperature. The vibrational distribution of the B state shows that the B state is populated not only by the radiative decay of the C state but also from other collisional processes, since the Franck-Condon principle cannot predict the vibrational population of the B state from the C state [1 – 5].

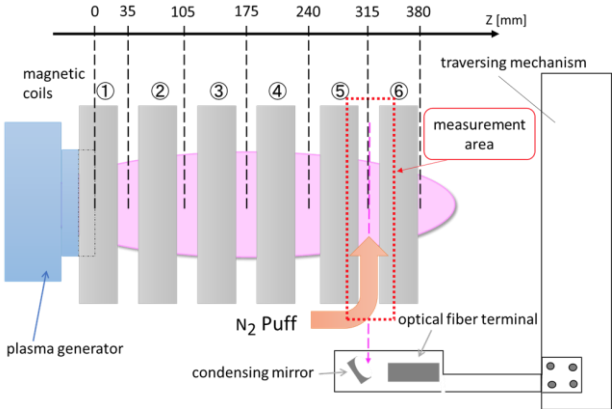

Fig. 1. Schematic diagram of the experimental set-up of optical terminal and the plasma plume.

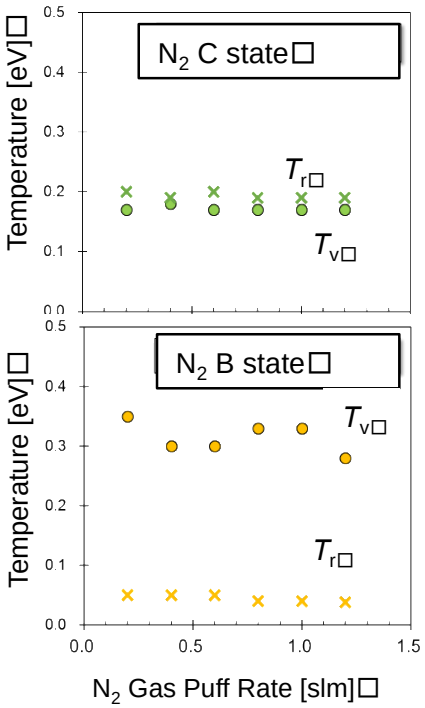

Fig. 2. Temperatures of N_2 B and C states puffed onto the Ar arc jet. The N_2 puff position is Z = 315 mm, observed from the same longitudinal position.

Reference

1. S. Fukukawa, A. Nezu, R. A. A. El-Koramy, and H. Akatsuka: 2017 Annual Meeting Record, IEE Japan, vol. 1, p. 184 (2017).
2. S. Fukukawa, A. Nezu, and H. Akatsuka: The Papers of Technical Meeting on "Plasma Science and Technology", IEE Japan, PST-17-061, pp. 9-14 (2017).
3. H. Akatsuka, S. Fukukawa, and A. Nezu: Proc. PLASAS-9, p. 18 (2017).
4. S. Fukukawa, A. Nezu, and H. Akatsuka: Extended Abstracts, The 78th JSAP Autumn Meeting, p. 07-002 (2017).
5. S. Fukukawa, A. Nezu, and H. Akatsuka: On-line Proc. Plasma Conf. 2017, 23P-88 (2017).

E.3 OES Measurements of Electron Temperature of Atmospheric-Pressure Microwave Discharge Argon Plasma — CR Model-Assisted Line-Intensity Measurement and Continuum Measurement

Hiroshi AKATSUKA, Reda A. A. EL-KORAMY and Atsushi NEZU

Atmospheric-pressure non-equilibrium plasmas have been arising keen interest among industrial society, particularly in the medical applications. Conventional diagnostic methods like electrostatic probes, or OES measurement with corona model or with LTE model cannot be applied to them. Recently, Park *et al.* reported T_e measurement method based on the spectral analysis of the continuum spectrum, emitted as the bremsstrahlung due to free electron collisions with neutral species in the plasma, which seems a promising method from the experimental and practical viewpoints [1].

We should describe the theoretical background of the continuum spectrum emitted from the atmospheric-pressure non-equilibrium plasma. Park *et al.* confirmed the validity of the emissivity of the electron-neutral bremsstrahlung is expressed as:

$$\epsilon_{ea} = \sqrt{\frac{2}{m_e}} \frac{n_e n_a}{\lambda^2} \frac{hc}{4\pi} \int_{h\nu}^{\infty} Q_{ea}^{B}(\lambda, E)\sqrt{E} f(E) \mathrm{d}E, \quad (1)$$

where $h\nu$, E, h, c, λ and m_e are the emitted photon energy, the electron energy, the Planck constant, the speed of light, the emitted photon wavelength and the electron mass, respectively. This indicates that we can analytically determine the spectral shape of the continuum spectrum, which can fit the observed one to determine the electron temperature [2].

Experimentally, we used a microwave discharge plasma torch electrode of coaxial type, keeping the flow rate of Ar at 8.0 l/min and changing that of N_2 (0.1 – 0.5 l/min) as a minor impurity to determine the rotational temperature. The plasma torch is made of aluminium. An aluminium antenna with 7 mm diameter and 23 mm length is used inside the quartz discharge tube, which is 170 mm in its length, with an inner diameter of 10 mm and outer diameter of 13 mm.

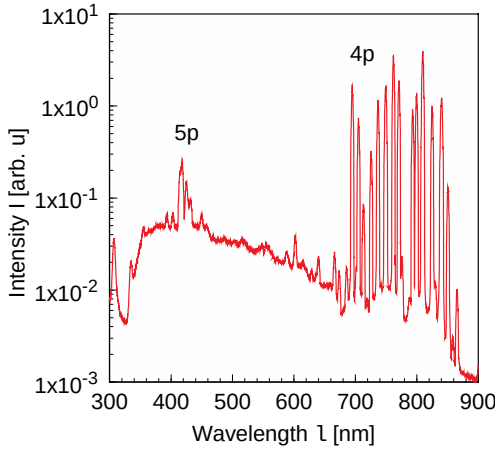

Fig. 1. The continuum spectrum with argon line spectra emitted from the present atmospheric-pressure microwave-discharge argon plasma.

Figure 1 shows the continuum spectrum obtained. Equation (1) directly fits the continuum spectrum, which determined T_e as the best-fit parameters, which indicates T_e ~ 0.9 eV.

To confirm this value, we applied a different method to deduce the electron temperature. We already obtained the relationship between the electron temperature and the excitation temperature based on the Ar-CR model that includes atomic collisional processes. When we fix the electron density and the gas temperature determined approximately by N_2 2PS rotational temperature as minor impurity, we can find the dependence of the excitation temperature of 4p-5p levels on the electron temperature, where we found that the dependence on the electron density is rather weak for $T_e \leq 1.2$ eV, as shown in Fig. 2. We observed the excitation temperature of Ar 4p-5p levels, which was found to be 0.38 eV. Then, we found the electron temperature to be (0.9 ± 0.1) eV from Fig. 2. We find a good agreement of the value of electron temperature, determined from continuum spectrum and from line-spectrum analysis assisted with the CR model. We consider that the reliability of both methods has now been improved considerably [2].

Reference

1. H. Akatsuka: Extended Abstracts of the 77th JSAP Autumn Meeting, 100000001-188 (2016).
2. H. Akatsuka, T. Yuji, and R. A. A. El-Koramy: Proc. 34th Symposium on Plasma Processing/29th Symposium on Plasma Science for Materials, P2-2 (2017).

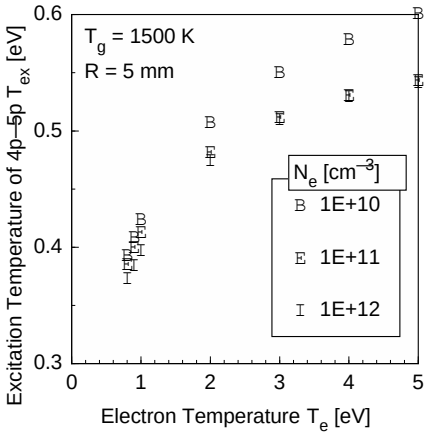

Fig. 2. Excitation temperature as a function of electron temperature and density.

E.4 Characteristics of Arc Plasma Generated in Water for the Application to Decommissioning of Degraded Power Nuclear Reactor

Hiroshi AKATSUKA, Atsushi NEZU and Shinsuke MORI

Since the accident of Fukushima No.1 nuclear power plant, it has been very pressing problem to establish how to decommission the accident reactor. One of the most serious issues is to take out solidified nuclear debris. In order to take it out of the reactors, we must cut or crush them into appropriate sizes. Since optical fibers as laser guide are weak for γ-ray radiation, to apply arc plasmas is one of the promising ways. The immersion of the debris into water for various treatment in remote handling has more safe. However, there was few study on the arc plasmas generated in water. In this study, we measure some characteristics of the arc discharge plasma with the electrodes immersed in water under atmospheric pressure.

Figure 1 schematically shows the plasma generator and other equipment. As for the plasma torch, the anode was made of copper and the cathode of 2%-thoriated tungsten. The flow rate of Ar was set at 30 L/min. We poured tap water into the chamber to immerse the electrodes over 10 mm from the nozzle tip. Ar was introduced through the torch and replaced the atmospheric gas as discharge gas between electrodes. The external motor controlled the distance between the electrodes. The way to ignite the arc plasma was to make electrodes short-circuited followed by separating them. We measured characteristics when the DC circuit current was set about 40 – 200 A [1].

We measured current-voltage characteristics of the discharge plasma. The voltage value was determined as the voltage difference of the electrodes at output terminal. Meanwhile, we measured the current value by a clamp-on current probe at the output terminal to the cathode, which is shown in Fig. 2. The distance between the electrodes, i.e. the arc length, was 2–5 mm. With increasing the current, the resistance continued to decrease and all of their resistance characteristics changed from negative ones to positive ones. However, the arc length effects on the arc voltage were different. It was found the voltage value of the gas-phase arc plasma depended on the length, whereas that of underwater one was almost independent [2].

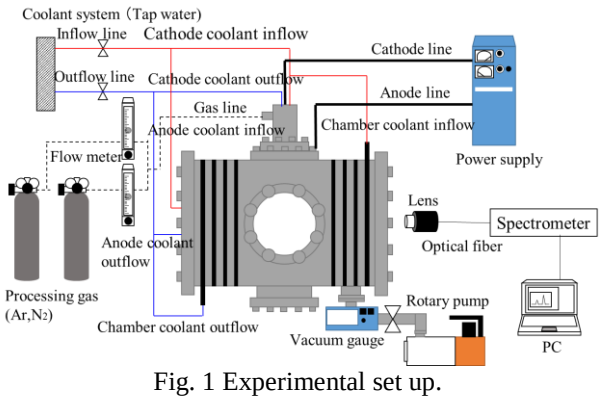

Fig. 1 Experimental set up.

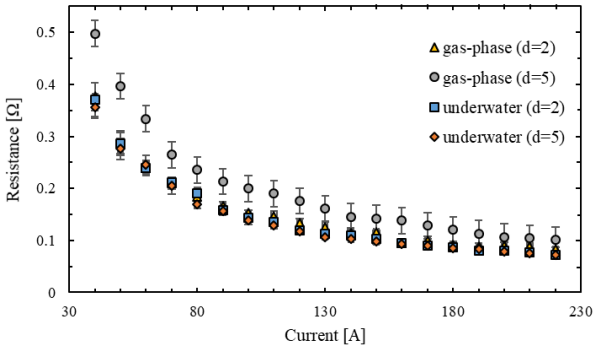

Fig. 2 Current-resistance characteristics of underwater and gas-phase arc plasma when the arc length d = 2, 5 [mm].

Figure 3 shows optical emission spectra from 200 nm to 800 nm of the underwater and gas-phase arc plasma in 160 A. They showed Ar I 4p-4s transitions in 700 - 800 nm and Ar I 5p-4s transitions in 400 - 450 nm. However, H α line around 656 nm area and H β line around 486 nm of the underwater arc plasma were obviously stronger than those of the gas-phase one. Therefore, we considered that underwater arc plasma decomposed the water molecule and generated hydrogen radicals. In addition, the underwater plasma should be turned on electrically through the water. Hence the arc length didn't influence so much on the voltage.

Reference

1. D. Hirotani, Y. Matsuoka, R. Suzuki, A. Nezu, S. Mori, R. A. A. El-Koramy and H. Akatsuka: Annual Meeting Record, IEE Japan, vol. 1, p. 96 (2017).
2. Y. Matsuoka, D. Hirotani, R. Suzuki, A. Nezu, S. Mori, H. Akatsuka: The Papers of Joint Technical Meeting on Plasma Science and Technology, Pulsed Power Technology and Electrical Discharge, IEE Japan, PST-17-024, PPT-17-024, ED-17-044, pp. 25-30 (2017).
3. R. Suzuki, D. Hirotani, Y. Matsuoka, A. Nezu, S. Mori, H. Akatsuka: On-line Proc. Plasma Conf. 2017, 21P-94 (2017).

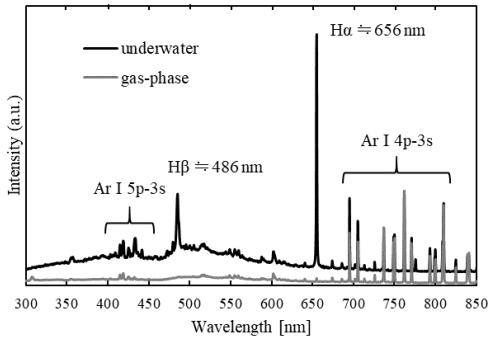

Fig. 3 Emission spectra of the underwater and gas-phase arc plasma in 160A.

III. Co-operative Researches

III. Co-operative Researches

III.1 Co-operative Researches within Tokyo Institute of Technology

(1) Development of the Clamp-on Ultrasound Flow Meter for Steam in Pipe, Dr. Tatsuya Kawaguchi of Department of Mechanical Engineering, Tokyo Institute of Technology
(2) Development of an Electromagnetic Shock Tube for Production of Dissociated Atomic Hydrogen Targets for Heavy-Ion Interaction Experiments, Department of Mechanical Engineering, School of Engineering.
(3) Akitoshi Okino (FIRST, IIR): Exploration of the mechanism for the birth of life on earth from the aspect of plasma and radiation.
(4) Study of fission and nuclear collision by Antisymmetrized Molecular Dynamics, Astuhiko Etori, Chikako Ishizuka, and Satoshi Chiba
(5) Study of nuclear fission using multidimensional Langevin models, Mark Usang, Chikako Ishizuka, Satoshi Chiba
(6) Study of antineutrons from nuclear reactors, Tadashi Yoshida, Rei Kimura, Hiroshi Sagara
(7) Study of nuclear fission mechanism using TDHF, Yoritaka Iwata, Takashi Nakamura, Kean Kun Ratha, Satoshi Chiba
(8) Study on the decommissioning, Kenichi Tanaka, Riku Nakamura, Satoshi Chiba
(9) Study of nuclear data evaluation for the transmutation, Shin Okumura, Kohsuke Tsubakihara, Atsunori Terashima, Satoshi Chiba
(10) Fundamental research on remote cutting and size-reduction of nuclear fuel debris immersed in water by arc discharge plasma, School of Materials and Chemical Technology

III.2 Co-operative Researches with Outside of Tokyo Institute of Technology

(1) Study on numerical kinetic analysis method by integral kinetic model with delayed neutrons, Hiroki Takezawa, Tokyo City University
(2) High-Temperature Solar Thermal Energy Recovery, Cross-ministerial Strategic Innovation Promotion Program, Cabinet Office, Government of Japan, 2014-2018.
(3) Solid oxide electrolysis cell development for CO_2 reduction, JSPS Grant-in-Aid for Scientific Research (B), 2016-2019.
(4) n_TOF Collaboration, CERN
(5) Collaborative research on thermal-hydrodynamics for future light water reactor, energy system and chemical technology development, Prof. Hai Ngoc DUONG of Vietnam Academy of Science and Technology.
(6) Collaborative research on two-phase flow dynamics for future light water reactor development, Director Won-Pil BAEK and Manager Chul-Hwa SONG of Korea Atomic Energy Research Institute.
(7) Collaborative research on fluid engineering, Prof. Hideki KAWAI of Muroran Institute of Technology.
(8) Collaborative research on multiphase flow engineering, Prof. Mituaki OCHI and Assistant Prof. Kenji KOFU of Nihon University.
(9) Collaborative research on treatment, disposal of radioactive waste and nuclear safety, Associate Prof. Kazushi Kimoto of Okayama University.
(10) Collaborative research on thermal-hydrodynamics for future light water reactor, energy system and chemical technology development, Prof. Horst-Michael PRASSER of Swiss Federal Institute of Technology (ETH Zurich).
(11) Development of Removal Process of Platinum Group Metals for Quality Improvement and Decrease of Generation Amount of Vitrified Object, Japan Science and Technology Agency (JST).
(12) Advanced Research and Education Program for Nuclear Decommissioning, Japan Science and Technology Agency (JST). (Principal Investigator: Prof. Obara, Tokyo Institute of Technology, Research Laboratory for Nuclear Reactors)
(13) Development of New Separation Technique of Radioactive Cesium from Contaminated Soil Using Agricultural and Waste Based Biomass, Grant-in-Aid for Young Scientists (B), Japan Society for the Promotion of Science (JSPS).
(14) Evaluation of Exposure Dose on Overpack and High Content Vitrified Waste of HLLW, Radioactive Waste Management Funding and Research Center.
(15) Cesium Recovery from soil by ion exchange using subcritical water containing metal ions and Vitrification for high volume reduction, Ministry of the Environment Government of Japan.
(16) Study for Cesium recovery from clay mineral by pressurized and heated water, Mitsubishi Materials.
(17) Consideration of mechanism related to remove DBP, IHI Corporation.
(18) Study on Low-Cost Process of SiC/SiC Composites: Japan Aerospace Exploration Agency (JAXA)
(19) Study on Properties of B_4C Neutron-Absorbing Materials for Control Rods: Japan Atomic Energy Agency (JAEA)
(20) Study on Neutron-Irradiation Resistance of Orientation-Controlled Ceramics: National Institute for Materials Science (NIMS)
(21) Sinterability of SiC Ceramics with Al_4SiC_4 Addition and Their Properties: National Institute for Materials Science (NIMS)
(22) Study on the Evaluation of Thermal Shock Fracture Behavior of Ceramics: Tokyo Metropolitan University
(23) Research on Formation and Characterization of Oxide Nanopowder : Vinca Institute, University of Belgrade, Serbia
(24) Development of Porous Ceramics using Natural Minerals for Adsorption and Immobilization of Radioactive Nuclides: Silica Material LLC.

(25) Fundamental Study on Plasma Resistance of Rare-Earth Fluoride Ceramics: Nippon Yttrium Co., Ltd.
(26) Formation of Conductors on Sintered Ceramics with Reaction Layer, SAMSUNG R&D Institute Japan.
(27) Development of Interphase Formation Process of High-Performance Ceramics-Based Composites Based on Electrochemical Approach, Grant-in Aid for Scientific Research (C), Japan Society for the Promotion of Science
(28) Development of Highly Microstructure-Controlled Neutron Control Ceramics for Improving Safety of Fast Breeder Reactors, Innovative Nuclear Research and Development Program, MEXT.
(29) Astrobiology Experiments Based on MeV Ion Beams, Division of Materials Science and Chemical Engineering, Faculty of Engineering, Yokohama National University.
(30) Development of Negative Ion Sources for Tandem Accelerators, Atomic Energy Research Laboratory, Tokyo City University.
(31) Selective Irradiation of Cancer Cells by Electrons Emitted from Cancer-Localizing Drugs, Grant-in-Aid for Scientific Research (B), Japan Society for the Promotion of Science.
(32) Synthesis of Anticancer Drugs inside Cancer Cells from Non-toxic Precursors by Monochromatic X-ray Irradiation, Grant-in-Aid for Challenging Exploratory Research, Japan Society for the Promotion of Science.
(33) The control of radiation dependent DNA damage response molecular network, Akihiro Yanagihara, Division of Radiation Biology and Medicine, Department of Medicine, Faculty of Medicine, Tohoku Medical and Pharmaceutical University
(34) Analyze of gene expression alteration after ionizing radiation exposure using chromatin immunoprecipitation sequence method, Hironori Hoji, Center for Disease Biology and Integrative Medicine, The University of Tokyo
(35) Biological significance of “protein phosphorylating” function of DNA-PK in DNA double-strand break repair, JSPS Grant-in-Aid for Scientific Research (B).
(36) Unification of effects of radiation and chemical substance and evaluation of personal variance in sensitivity, Ministry of Environment.
(37) Regulation of DNA double-strand break repair through dynamic change in protein secondary structure, Akinari Yokoya (QST).
(38) Mechanisms of DNA double-strand break repair through non-homologous end joining, Junya Kobayashi (Kyoto University).
(39) Molecular mechanisms of neutron-induced DNA damage and its repair, Hirokuni Yamanishi, Toshiro Matsuda (Kinki University).
(40) Molecular mechanisms of the repair of heavy ion-induced DNA damages, Ryoichi Hirayama (QST-NIRS).
(41) Study of fission and nuclear collision by Antisymmetrized Molecular Dynamics, Akira Ono
(42) Total Absorption Gamma-ray Spectroscopy for Decay Heat Calculation and Other Applications, Muriel Fallot, Tadashi Yoshida, Marek Karny, Alejandro Algora, Jose Tain, Alan L. Nichols Jean-Christoph Sublet, Alejandro Sonzogni, Paraskevi Dimitriou
(43) Study on nuclear astrophysics, Taketo Hayakawa, Toshitaka Kajino
(44) Study on measurements of fission product yield, Katsuhisa Nishio, Andrei Andreyev, Hiroyuki Koura, Ichiro Nishinaka, Kentaro Hirose, hiroyuki Makii, Riccardo Orlandi, James Smallcombe, Roman Leguillon
(45) Time-resolved Optical Emission Spectroscopic Measurement of Pulsed Discharge Plasmas and their Atomic and Molecular Processes, Grant-in-Aid for Scientific Research (B), Japan Society for the Promotion of Science.
(46) Spectroscopic Analysis of Low-Pressure Discharge Argon Plasma, Cannon Inc.
(47) Measurement of Vibrational and Rotational Temperature in Spark Discharge Plasma by Optical Emission Spectroscopy, Toyota Central R&D Labs., Inc.
(48) Effect of Plasma Jet Diameter on the Efficiency of Reactive Oxygen and Nitrogen Species Generation in Water, Kochi University of Technology.
(49) Fluoride Addition Effects on Voltammograms and UV-vis Spectra of Neodymium Cation in Molten Chlorides, Tokyo City University, Kyoto University, Osaka University.
(50) XAFS Measurement of Simulated Waste Glass Samples, JAEA, Tokyo City University.
(51) OES Measurements of Electron Temperature of Atmospheric-Pressure Microwave Discharge Argon Plasma, University of Miyazaki.

IV. List of Publications

IV. List of Publications

Journals

(1) Hiroki Takezawa, Toru Obara: Passive measure for preventing recriticality of fuel debris dust for defueling at Fukushima Daiichi nuclear power station; *Journal of Nuclear Science and Technology*, Vol **53**, No. 12, pp. 1960-1967 (2016).

(2) Odmaa Sambuu, Toru Obara: Possible design of PBR for passive decay-heat removal; *Journal of Nuclear Science and Technology*; Vol. **53**, No. 9, pp. 1296-1309 (2016).

(3) Irwan Liapto Simanullang, Toru Obara: Improvement of core design of small pebble bed reactor with accumulative fuel loading scheme; *Annals of Nuclear Energy*, Vol. **94**, pp. 87-92 (2016).

(4) Delgersaikhan Tuya, Toru Obara: Supercritical kinetic analysis in simplified system of fuel debris using integral kinetic model; *Annals of Nuclear Energy*, Vol. **91**, pp. 59-64 (2016).

(5) Julia Abudul Karim, Jun Nishiyama,, Toru Obara: Application of melt and refining procedures in the CANDLE reactor concept; *Annals of Nuclear Energy*, Vol. **90**, pp. 275-283 (2016).

(6) Haruka Kikuchi, Toru Obara: Development of Transient Analysis Code for Estimation of Total Released Energy in a Two-Fuel-Solution-Tank System; *Annals of Nuclear Energy*, Vol. **87**, pp. 486-493 (2016).

(7) Hai Quan Ho, Toru Obara: Design concept for a small pebble bed reactor with ROX fuel; *Annals of Nuclear Energy*, Vol. **86**, pp. 471-478 (2016).

(8) Y. Kato, "Industrial Application of Carbon Recycling Energy System Technology Driven by Nuclear Power", Energy Procedia, 131, 108–112 (2017)

(9) M. Zamengom, Y. Kato, "Comparison of magnesium hydroxide/expanded Graphite composites for thermal energy storage in cogeneration nuclear power plants", Energy Procedia, 131, 119–126 (2017)

(10) M. C. A. Nepomuceno, "Development of disk-type solid oxide electrolysis cell for CO_2 reduction in an active carbon recycling energy system", Energ Procedia, 131, 101–107(2017)

(11) Emanuela Mastronardo, Lucio Bonaccorsi, Yukitaka Kato, Elpida Piperopoulos, Maurizio Lanza, Candida Milone, Strategies for the enhancement of heat storage materials performances for MgO/H2O/Mg(OH)2 thermochemical storage system, Applied Therm. Eng., accepted on 1 Aprile, 2017.

(12) Hiroki Takasu, Junichi Ryu, Yukitaka Kato, "Application of lithium orthosilicate for high-temperature thermochemical energy storage", Applied Energy 193, 74–83(2017)

(13) Massimiliano Zamengo, Juraj Tomaškovič, Junichi Ryu, Yukitaka Kato, "Thermal Conductivity Measurements of Expanded Graphite-Magnesium Hydroxide Composites for Packed Bed Reactors of Chemical Heat Storage/Pump Systems", *J. Chem. Eng. Japan*, Vol. 49, No. 3, pp. 261-267, 2016.

(14) Tatsuhiro Saito, Tatsuya Katabuchi, Brian Hales, M. Igashira. Measurement of thick-target gamma-ray production yields of the ^{7}Li(p,p')^{7}Li and ^{7}Li(p,γ)^{8}Be reactions in the near-threshold energy region for the ^{7}Li(p,n)^{7}Be reaction, Journal of Nuclear Science and Technology, Vol. **54**, pp. 1-7, (2016).

(15) F. Gunsing, Tatsuya Katabuchi (64th author), n_TOF Collaboration (145 authors). Nuclear data activities at the n_TOF facility at CERN, The European Physical Journal Plus, Vol. **131**, 371, (2016).

(16) M. Barbagallo, Tatsuya Katabuchi (64th author), n_TOF Collaboration (133 authors). ^{7}Be(n,α)α reaction and the cosmological lithium problem: Measurement of the cross section in a wide energy range at n_TOF at CERN, Physical Review Letters, Vol. **117**, 152701, (2016).

(17) L.Cosentino, Tatsuya Katabuchi (65th author), n_TOF Collaboration (132 authors). Experimental setup and procedure for the measurement of the ^{7}Be(n,α)α reaction at n_TOF, Nuclear Instruments and Methods in Physics Research Section A, Vol. **830**, pp. 197-205, (2016).

(18) Tomonori Ihara, Nobuyoshi Tsuzuki and Hiroshige Kikura, Application of Ultrasonic Doppler Velocimetry to Molten Glass by Using Broadband Phase Difference Method, *Flow Measurement and Instrumentation*, Vol. **48** , pp. 90–96 (2016).

(19) Ari Hamdani, Tomonori Ihara, Nobuyoshi Tsuzuki and Hiroshige Kikura, Experimental Study of gas-liquid swirling flow in a Vertical Tube using UVP and WMS, *Journal of Mechanical Science and Technology*, Springer (Germany), Vol. **30,** No.9, pp.3897-3905 (2016),.

(20) Thang Tat Nguyen, Nobuyoshi Tsuzuki, Hideki Murakawa, Ngoc Hai Dung and Hiroshige Kikura, Measurement of the condensation rate in subcooled flow boiling by using two ultrasonic frequencies, *International Journal of Heat and Mass Transfer*, Vol. **99**, pp.159-169 (2016).

(21) Ari Hamdani, Tomonori Ihara and Hiroshige Kikura, Experimental and Numerical Visualizations of Swirling Flow in a Vertical Pipe, *Journal of Visualization*, Springer (Germany), Vol. **19**, No.3, pp. 369-382 (2016).

(22) Travis S. Grimes, Colt R. Heathman, Santa Jansone-Popova, Vyacheslav S. Bryantsev, Sriram Goverapet Srinivasan, Masahiko Nakase, Peter R. Zalupski,: Thermodynamic, Spectroscopic and Computational Studies of f-Element Complexation by N-hydroxyethyl-diethylenetriamine-N,N',N",N"-tetraacetic Acid; *Inorg. Chem.*, **56** (3), pp 1722–1733 (2017).

(23) Xiangbiao Yin, Xinpeng Wang, Hao Wu, Toshihiko Ohnuki, Kenji Takeshita: Enhanced desorption of cesium from collapsed interlayer regions in vermiculite by hydrothermal treatment with divalent cations; *Journal of Hazardous Materials*, Vol. **326**, pp.47–53 (2017).

(24) Kota Kawai, Tatsuya Fukuda, Yoshio Nakano and Kenji Takeshita: Thermal decomposition analysis of simulated high-level liquid waste in cold-cap; *EPJ Nuclear Sciences & Technologies*, **2**, 44 (2016).
(25) Imari Takatsuka, Hideharu Takahashi, Ttsuya Fukuda, Miki Harigai, Yusuke Inaba, Kenji Takeshita: Fundamental Study on Cs Elution Technique from Vermiculite by Hydrothermal Treatment Using Cellulose-based Biomass; *Journal of the Society for Remediation of Radioactive Contamination in the Environment*, Vol. **4**, No.3, pp.231-238 (2016).
(26) Q. Yu, T. Ohnuki, K. Tanaka, N. Kozai, S. Yamasaki, F. Sakamoto, Y. Tani, Fungus-promoted transformation of lanthanides during the biooxidation of divalent manganese, Geochimica Cosmochimica Acta, **Vol. 174**, 1-12(2016).
(27) Keiko Yamaji, Satoshi Nagata, Toshikatsu Haruma, Toshihiko Ohnuki, Tamotsu Kozaki, Naoko Watanabe, Kenji Nanba, Root endophytic bacteria of a 137Cs and Mn accumulator plant, *Eleutherococcus sciadophylloides*, increase 137Cs and Mn desorption in the soil, J. Environmental Radioactivity, **Vol 153**, 112-119(2016).
(28) Stephanie Handley-Sidhu, Thomas K. Mullan, Quentin Grail, Malek Albadarneh, Toshihiko Ohnuki & Lynne E. Macaskie, Influence of pH, competing ions, and salinity on the sorption of strontium and cobalt onto biogenic hydroxyapatite, Science Reports, **Vol. 6**:23361 | DOI: 10.1038/srep23361 (2016).
(29) Shinya Yamasaki, Junpei Imoto, Genki Furuki, Asumi Ochiai, Toshihiko Ohnuki, Keisuke Sueki, Kenji Nanba, Rodney C. Ewing, Satoshi Utsunomiya, Radioactive Cs in the estuary sediments near Fukushima Daiichi Nuclear Power Plant, Science of The Total Environment, **Vol. 551–552**, 2016, 155–162(2016).
(30) Toshihiko Ohnuki, Yukitoshi Aiba, Fuminori Sakamoto, Naofumi Kozai, Tadafumi Niizato,Yoshito Sasaki, Direct accumulation pathway of radioactive cesium to fruitbodies of edible mushroom from contaminated wood logs, Scientific Reports, **Vol. 6**, 29866 | DOI: 10.1038/srep29866(2017).
(31) Mohd Idzat Idris, Saishun Yamazaki, Katsumi Yoshida, Toyohiko Yano: Defects annihilation behavior of neutron-irradiated SiC ceramics densified by liquid-phase-assisted method by post-irradiation annealing; Nuclear Materials and Energy, Vol.9, 199-206 (2016).
(32) Toshihiro Isobe, Naoto Houtsuki, Yuko Hayakawa, Katsumi Yoshida, Sachiko Matsushita, Akira Nakajima: Preparation and properties of $Zr_2MoP_2O_{12}$ ceramics with negative thermal expansion; *Materials and Design*, Vol. 112, 11-16 (2016).
(33) Liang Sun, Yimin Gao, Yefei Li, Katsumi Yoshida, Toyohiko Yano, Dawei Yi: Structural, Bonding, Anisotropic Mechanical and Thermal Properties of Al_4SiC_4 and $Al_4Si_2C_5$ by First-Principles Investigations; *Journal of Asian Ceramic Society*, Vol. 4, 289-298 (2016).
(34) Makoto Koizumi, Motoaki Utamura, Toyohiko Yano, Susumu Nakano, Takanori Shibata, and Chihiro Myoren, “CFD analysis of water droplet behavior in axial flow compressor”, Internat. J. Gas Turbine, Propulsion and Power System, Vol.8, Number 3, pp.12-19 (2016).
(35) M. R. Matsuda, A.V. Gubarevich, H. Wada, O. Odawara: Effect of sintering temperature on the characteristics of ceramic hollow spheres produced by sacrificial template technique; *Ceramics International*, Vol. 42, No. 7, pp. 8409-8412 (2016).
(36) Y. Hu, K. Kondo, Y. Mizushiro, Y. Oguri, H. Fukuda: Direct Observation of Dose Distribution around a Syringe-Needle Type Proton-Induced X-ray Source Using Liquid Scintillator and a CCD Camera; *Int. J. PIXE*, Vol. **26**, pp. 53–60 (2016).
(37) K. Kondo, Y. Oguri: Velocity Evolution of Electro-Magnetically Driven Shock Wave for Beam–Dissociated Hydrogen Interaction Experiment; *J. Phys.: Conf. Ser.*, Vol. **688**, 012052 (2016).
(38) Someya M, Hasegawa T, Hori M, Matsumoto Y, Nakata K, Masumori N, Sakata K. Local tumor control and DNA-PK activity of peripheral blood lymphocytes in prostate cancer patients receiving radiotherapy. *J. Radiat. Res.*, **58**, 225-231 (2017). https://academic.oup.com/jrr/article/58/2/225/2605918, doi: 10.1093/jrr/rrw099.
(39) Hasegawa T, Someya M, Hori M, Matsumoto Y, Nakata K, Nojima M, Kitagawa M, Tsuchiya T, Masumori N, Hasegawa T, *Sakata K. Expression of Ku70 predicts results of radiotherapy in prostate cancer. *Strahlenther. Onkol.*, **193**, 29-37 (2017). DOI 10.1007/s00066-016-1023-7
(40) *Hori M, Someya M, Matsumoto Y, Nakata K, Kitagawa M, Hasegawa T, Tsuchiya T, Fukushima Y, Gocho T, Sato Y, Ohnuma H, Kato J, Sugita S, Hasegawa T, Sakata K. Influence of XRCC4 expression in esophageal cancer cells on the response to radiotherapy. *Med. Mol. Morphor.*, **50**, 25-33 (2016). 10.1007/s00795-016-0144-5.
(41) Takada Y, Someya M, Matsumoto Y, Satoh M, Nakata K, Hori M, Saito M, Horikawa N, Tateoka K, Teramoto M, Saito T, Hasegawa T, *Sakata K. Influence of Ku86 and XRCC4 expression in uterine cervical cancer on the response to preoperative radiotherapy. *Med. Mol. Morphor.*, **49**, 210-216 (2016). Doi 10.1007/s-00795-016-0136-5.
(42) Mikio Shimada: The role of PNKP in maintenace of genome stability and neural development; *Seikagaku*, vol. **88**, No. 4, pp. 484-487, Aug. 2016.
(43) Mikio Shimada, Fumio Matsuzaki, Akihiro Kato, Junya Kobayashi, Tomohiro Matsumoto, Kenshi Komatsu: Induction of Excess Centrosomes in Neural Progenitor Cells during the Development of

Radiation-Induced Microcephaly; *PLoS One*, Vol. **11**, No. 7, Jul. 2016.6.

(44) Y. Iwata, N. Shimizu, T. Otuka, Y. Ustuno, J. Menendez, M. Honma, and T. Abe : Erratum : Large-Scale Shell-Model Analysis of the Neutrinoless ββ Decay of ^{48}Ca ; *Physical Review Letters*, Vol **117**, pp. 179902 (2016).

(45) T. Hayakawa, S. Miyamoto, T. Mochizuki, K. Horikawa, S. Amano, D. Li, K. Imazaki, Y. Izawa, K. Ogata, S. Chiba: Laser Compton scattering gamma-ray experiments for supernovae neutrino process; *Plasma and Fusion Research*, Vol. **11**, pp. 3406066 (2016).

(46) S. Shibagaki, T. Kajino, G. J. Methews, S. Chiba, S. Nishimura and G. Lorusso: Relative contribution of the weak, main and fission-recycling r-process; *Astrophysical Journal*, Vol. **816**, No. 2, pp. 79 (2016).

(47) Tadashi Yoshida Takahiro Tachibana, Naoto Hagura and Satoshi Chiba: Composition, decomposition and analysis of reactor antineutrino and electron spectra based on gross theory of β-decay and summation method; *Progress in Nuclear Energy*, Vol. **88**, pp. 175-182 (2016).

(48) R.Capote, N. Carjan and S. Chiba: Scission-neutrons for U, Pu Cm and Cf isotopes: relative multiplicities calculated in the sudden limit; *Physical Review C*, Vol. **93**, pp. 024609 (2016).

(49) T. Hayakawa, T. Shizuma, S. Miyamoto, S. Amano, A. Takemoto, M. Yamaguchi. K. Horikawa, Y. Akimune, S. Chiba, K. Ogata and M. Fujiwara: Spatial anisotropy of neutrons emitted from the ^{56}Fe(γ,n)^{55}Fe reaction with linearly polarized γ ray beam; *Physical Review C*, Vol. **93**, pp. 044313 (2016).

(50) Rei Kimura, Hiroshi Sagara, and Satoshi Chiba: Principle validation of nuclear fuel material isotopic omposition measurement method based photofission reactions; *Journal of Nuclear Science and Technology*, Vol. **52**, No.12, pp. 1978-1987 (2016).

(51) F. A. Ivanyuk, S. chiba, Y. Aritomo: The Transport Coefficient of Collective Motion within the Two-Cemter Shell Model Shape Parametrization; *Journal of Nuclear Science and Technology*, Vol. **53**, No.6, pp. 737-748 (2016).

(52) D. Ichinkhorloo, M. Aikawa, S. Chiba, Y. Hirabayashi, K. Kato: Low energy scattering cross sections for n+^{6,7}Li reactions using the continuum-discretized couled-channels method; *Physica Review C*, Vol. **93**, pp. 064612 (2016).

(53) R. Leguillon, K. Nishio, K. Hirose, H. Makii, I. Nishinaka, R. Orlandi, K. Tsukada, J. Smallcombe S. Chiba, Y. Aritomo, T. Ohtsuki, R. Tatsuzawa, N. Takaki, N. Tamura, S. Goto, I.Tsekhanovich, C. M. Petrache, A. N. Andreyev: Fission fragments mass distributions of nuclei populated by the multinucleon transfer channels of the ^{18}O+^{232}Th reaction; *Physics Letters B*, Vol. **761**, pp. 125-130 (2016).

(54) Tadashi Yoshida, Takahiro Tachibana, Naoto Hagura, Satoshi Chiba: Composition, Decomposition and Analysis of Reactor Antineutrino and Electron Spectra based on Gross Theory of β-decay and Summation Method; *Progress in Nuclear Energy*, Vol. **88**, pp. 175-182 (2016).

(55) Atsunori Terashima, Masaki Ozawa: Evaluation of the specific radioactivity of 40 elements created by nuclear transmutation of fission products; *Progress in Nuclear Energy*, Vol. **93**, pp. 177-185 (2016).

(56) Mark Dennis A. Usang, Fedir A. Ivanyuk, Chikako Ishizuka, Satoshi Chiba: Effects of microscopic transport coefficients on fission observables calculated by the Langevin equation; *Physical Review C*, Vol. **94**, pp.044602 (2016).

(57) T. Hayakawa, Y. Toh, N. Huang, T. Shizuma, A. Kimura, S. Nakamura, H. Harada, N. Iwamoto, S. Chiba and T. Kajino: Measurement of the isomer production ratio for the ^{112}Cd(n, γ)^{113}Cd reaction using neutron beams at J-PARC; *Physical Review C*, Vol. **94**, pp. 055803 (2016).

(58) E. Sh. Soukovitskiim R. Capote, J. M. Quesada, S. Chiba, and D. S. Martyanov: Nucleon scattering on actinides using a dispersive optical model with extended coulplings; *Physical Review C*, Vol. **94**, pp. 064605 (2016).

(59) Jun-Seok Oh, Maito Kakuta, Hiroshi Furuta, Hiroshi Akatsuka, Akimitsu Hatta: Effect of Plasma Jet Diameter on the Efficiency of Reactive Oxygen and Nitrogen Species Generation in Water; *Japanese Journal of Applied Physics*, Vol. **55**, No. 6S2, 06HD01 (2016).

(60) Kei Kuwano, Atsushi Nezu, Haruaki Matsuura, Hiroshi Akatsuka: Dissociation Degree of Nitrogen Molecule in Low-Pressure Microwave-Discharge Nitrogen Plasma with Various Rare-Gas Admixtures; *Japanese Journal of Applied Physics*, Vol. **55**, No. 8, 086101 (2016).

(61) Hiroshi Akatsuka, Tomohiko Shibata, Atsushi Nezu: Discussion on Population Kinetics and Number Densities of Excited Species of Low-Pressure Discharge Nitrogen Plasma; *IEEJ Transactions on Electrical and Electronic Engineering*, Vol. **11**, Num. S1, pp. S9-S18 (2016).

(62) Haruaki Matsuura, Atsushi Nezu, Hiroshi Akatsuka, Akihiro Uehara, Toshiyuki Fujii: Fluoride Addition Effects on Voltammograms and UV-vis Spectra of Neodymium Cation in Molten Chlorides; *ECS Transactions*, Vol. **75**, No. 15, pp. 63-67 (2016).

(63) Takayuki Nagai, Hidekazu Kobayashi, Ken-ichi Sasage, Yasuo Ayame, Yoshihiro Okamoto, Hideaki Shiwaku, Haruaki Matsuura, Takafumi Uchiyama, Yukiko Okada, Atsushi Nezu, Hiroshi Akatsuka, Toshiaki Kakihara, Hidenori Kawashima: XAFS Measurement of Simulated Waste Glass Samples (Borosilicate Glass Including Vanadium); *JAEA-Research*, Vol. **2016**-015, pp. 1-52, (2016).

(64) Hiroshi Akatsuka, Jong-Shinn Wu, Kungen Teii, Koichi Takaki: Introduction to the Special Issue on

the 9th Asia-Pacific International Symposium on the Basics and Applications of Plasma Technology (APSPT-9), and the 28th Symposium on Plasma Science for Materials (SPSM-28); *IEEE Transactions on Plasma Science*, Vol. **44**, No. 12, pp. 3050 – 3051 (2016).

(65) Ampan Laosunthara, Jun Takeda, Hiroshi Akatsuka: Numerical Study of Electric Potential Formation in a Weakly Ionized Plasma Flowing Supersonically through Open Magnetic Field Lines; *Japanese Journal of Applied Physics*, Vol. **56**, No. 1, 016201 (2017).

(66) Kentaro URATA, Yoshinao KOBAYASHI. Precipitation mechanism pf copper sulfides in solid iron, Journal of the Japanese Society for Experimental Mechanics, Vol. 16, No. 4, pp. 342-347, Dec. 2016.

(67) rui lan, Rie Endo, Masashi Kuwahara, Yoshinao Kobayashi, Masahiro Susa. Thermal and Electrical Conductivity of Ge1Sb4Te7 Chalcogenide Alloy, Journal of ELECTRONIC MATERIALS, The Minerals, Metals & Materials Society, Oct. 2016.

(68) Takahiro Oshino, Yoshinao Kobayashi, Taichi Abe, Toshiyuki Koyama. Thermodynamics of Oxygen in the Fe-Nd-O System for Production of Dy Free Nd-Fe-B Magnet, Materials Transactions, JIM, Vol. 57, No. 10, pp. 1771 to 1775, Aug. 2016.

(69) Min WANG, Rie ENDO, Yoshinao Kobayashi, Yuki Susa, Masahiro Susa, Masahito Hanao. Radiative Heat Transfer Reduction across Mould Fluxes with Silicon Additions as Reducing Agent for Continuous Casting of Steel, Journal of the Technical Association of Refractories, Japan, Vol. 36, No. 1, p. 3-9, Apr. 2016.

(70) Rei Kimura, Hiroshi Sagara, Satoshi Chiba. Principle validation of nuclear fuel material isotopic composition measurement method based on photofission reactions, J. NUCL. SCI. TECHNOL., Vol. 53, Issue 12, p. 1978-1987, May. 2016.

(71) Nishikawa, M., Sano, T., Washimi, M., Takao, K., Tsubomura, T., Emission properties and Cu(i)-Cu(i) interaction in 2-coordinate dicopper(i)-bis(N-heterocyclic)carbene complexes, Dalton Transactions, Vol. 45, No. 30, pp. 12127-12136, 2016.

(72) Ikeda, S., Mori, T., Ikeda, Y., Takao, K., Microwave-Assisted Solvent Extraction of Inert Platinum Group Metals from HNO3(aq) to Betainium-Based Thermomorphic Ionic Liquid, ACS Sustainable Chemistry and Engineering, Vol. 4, No. 5, pp. 2459-2463, 2016.

(73) Mori, T., Takao, K., Ikeda, Y., Syntheses and physical properties of novel betainium-type ionic liquids derived from amino acids, Chemistry Letters, Vol. 45, No. 2, pp. 164-166, 2016.

(74) Masashi Otani, Tsutomu Mibe, M. Yoshida, Kazuo Hasegawa, Yasuhiro Kondo, N. Hayashizaki, Yoshihisa Iwashita, Yoshiyuki Iwata, Ryo Kitamura, Naohito Saito. Interdigital H-mode drift-tube linac design with alternative phase focusing for muon linac, Physical review accelerators and beams, Vol. 19, 040101-1/8, Apr. 2016.

(75) Daisuke Satou, M. Yoshida, N. Hayashizaki. Dielectric assist accelerating structure, Physical Review Accelerators and Beams, Vol. 19, 011302-1/9, Jan. 2016.

(76) Rio Kurimoto, Kei Kanie, Naokazu Idota, Mitsuo Hara, S. Nagano, Takehiko Tsukahara, Yuji Narita, Hiroyuki Honda, Masanobu Naito, Mitsuhiro Ebara and Ryuji Kato, Combinational Effect of Cell Adhesion Biomolecules and Their Immobilized Polymer Property to Enhance Cell-selective Adhesion, *International Journal of Polymer Science*, accepted (2016).

(77) Kyojiro Morikawa and Takehiko Tsukahara, Fabrication of Hydrophobic Nanostructured Surfaces for Microfluidic Control, *Analytical Sciences*, 32, 79-83 (2016).

(78) DongKi Hwang, Takehiko Tsukahara, Naomi Miyamoto,and Yasuhisa Ikeda, Spectrophotometric studies on solubility of lanthanoid(III) complexes with fluorinated β-diketonatesin supercritical carbon dioxide, *The Journal of Supercritical Fluids*, 110, 251-256 (2016).

(79) Masatoshi KONDO, Yuu NAKAJIMA, Teruya TANAKA, Takashi NOZAWA, Takehiko YOKOMINE. Experimental Study on Chemical Behaviors of Non-Metal Impurities in Pb, Pb-Bi and Pb-Li by Temperature Programmed Desorption Mass Spectrometer Analysis, Plasma and Fusion Research, The Japan Society of Plasma Science and Nuclear Fusion Research , Nagoya, Aichi, Japan, Vol. 11, Jul. 2016.

(80) Narumi Suzuki, Ryosuke Sasaki, Yoshihito Matsumura, Masatoshi Kondo. In-Situ Evaluation of Functional Layer by Electrochemical Impedance Spectroscopy, J. Japan Inst. Met., Vol. 80, No. 4, pp. 284-288, Mar. 2016.

(81) Narumi Suzuki, Ryosuke Sasaki, Yoshihito Matsumura Masatoshi Kondo, In-Situ Evaluation of Functional Layer Based on Impedance Behavior, J-STAGE, The Japan Institute of Metals and Materials, Vol. 80, No. 9, pp. 585-592, Jun. 2016.

(82) Masatoshi KONDO, Youji SOMEYA, Mitsuyo TSUJI, Satoshi YANAGIHARA, Hiroyasu UTOH, Kenji TOBITA Shinzaburo MATSUDA. Conceptual Design of Temporally Storage Area in Hot Cell for Fusion DEMO Reactor, Plasma and Fusion Research, The Japan Society of Plasma Science and Nuclear Fusion Research, Volume 11, pp. 1-7, Jun. 2016.

(83) Pribadi Mumpuni Adhi, Masatoshi KONDO, Minoru TAKAHASHI. Performance of solid electrolyte oxygen sensor with solid and liquid reference electrode for liquid metal, Sensors and Actuators B: Chemical, Elsevier, Vol. 241, pp. 1261-1269, 2016.

International Conference Proceedings

(1) Toru Obara, Jun Nishiyama, Hiroki Osato: CANDLE Burning Reactor with Plutonium Fuel Start-up Core; *Transactions of the American Nuclear Society*, **115**, 1319-1320 (2016) Las Vegas, NV, November 6-10, 2016.

(2) Y. Kato, H. Nogami, "Development of low carbon emission and material saving ironmaking system, SMART", 1st International Conference on Energy and Material Efficiency and CO_2 Reduction in the Steel Industry (EMECR2017), 11-13 October, 2017, Kobe.

(3) H. Takasu, H. Hoshino, Y. Tamura, Y. Kato, "Kinetic analysis of carbonation of lithium orthosilicate for thermochemical energy storage material", 1st International Conference on Energy and Material Efficiency and CO_2 Reduction in the Steel Industry (EMECR2017), 11-13 October, 2017, Kobe.

(4) Y. Numata, M. C. A. Mepomuceno, Y. Kato, "Development of Solid Oxide Electrolysis Cells for CO2 reduction in an Active Carbon Recycling Energy System as applied to iron-making process", 1st International Conference on Energy and Material Efficiency and CO_2 Reduction in the Steel Industry (EMECR2017), 11-13 October, 2017, Kobe.

(5) Yukitaka Kato, [Invited lecture] "High-Temperature Solar Thermal Energy Recovery and Utilization System Development for Energy Carrier Productions", Plenary: Beyond Power, SolarPACES2017, 28(26-29) September, 2017, Santiago, Chile.

(6) Hiroki Takasu, Hitoshi Hoshino, Yoshiro Tamura, Yukitaka Kato, "Carbonation kinetic study of thermochemical energy storage material of Li_4SiO_4/CO_2", International Sorption Heat Pump Conference (ISHPC2017), 8 (7-10) August, 2017, Tokyo, Japan.

(7) Yukitaka Kato, Massimiliano Zamengo, Keiko Fujioka, "Thermal Conductivity Enhancement Of Thermochemical Energy Storage Material For Performance Improvement", International Sorption Heat Pump Conference (ISHPC2017), 8 (7-10) August, 2017, Tokyo, Japan.

(8) Yukitaka Kato, K. Fujioka, M. Zamengo, "Thermal Conductivity Enhancement of Thermochemical Energy Storage Materials for Efficient Waste Heat Utilization", The first Asian Conference on Thermal Sciences (ACTS), Jeju, Korea, 27(26-30) March, 2017.

(9) Massimiliano Zamengo, Yukitaka Kato, Junko Morikawa, Measurement of thermal conductivity for a magnesium hydroxide-expanded graphite enhanced composite for thermochemical energy storage, 37th Japan Symp. Thermophysical Properties, Okayama, 29 Nov., 2016.

(10) Y. Kato, "Thermal energy utilization technologies for low-carbon future society", China-Japan Heat Transfer Research Workshop, Tianjin Univ, Tianjin, Chaina, 2016/11/18.

(11) Y. Kato, M. Zamengo, "Thermochemical energy storage material developments for surplus heat recovery", ASCON2016-5th Asian Conference on Innovative Energy & Environmental Chemical Engineering - IEEChE 2016, Yokohama, Japan 16 (13-16) November, 2016.

(12) Y. Kato, [Keynote] "Evaluation of a Smart Iron-Making System based on Active Carbon Recycling Technology", 2nd International Conference on Smart Carbon Saving and Recycling for Ironmaking, ICSRI 2, Pusan, Korea, 27(27-28) October, 2016.

(13) F. Mingrone, Tatsuya Katabuchi (64th author), n_TOF Collaboration (151 authors). The CERN n_TOF facility: a unique tool for nuclear data measurement, CNR*15 - 5th International Workshop on Compound-Nuclear Reactions and Related Topics, EPJ Web of Conferences, Vol. **122**, 05001, (2016).

(14) Tatsuya Katabuchi, Tomohiro Okamiya, Shotaro Yanagida, Motoharu Mizumoto, Kazushi Terada, Atsushi Kimura, Nobuyuki Iwamoto, Masayuki Igashira. Neutron capture cross section and capture gamma-ray spectra of 89Y, CNR*15 - 5th International Workshop on Compound-Nuclear Reactions and Related Topics, EPJ Web of Conferences, Vol. **122**, (2016).

(15) Keisuke Tsukada, Shun Kimura, Tatsuya Kawaguchi, Hiroshige Kikura, Katsuhiko Sugita and Shuichi Umezawa, Ultrasonic Steam Flowrate Measurement by Focusing Sensor Array, *Asian Conference on Experimental Mechanics 2016* (ACEM2016), November 14-16, 2016, Jeju, Korea, Paper No.160160.

(16) Ari Hamdani and Hiroshige Kikura, Numerical Study of Vortex Core in Turbulent Swirling Flow, *ANS Winter Meeting and Expo, Transactions of the American Nuclear Society*, Vol. 115, November 6-10, 2016, Las Vegas, USA , pp. 1569-1572.

(17) Ari Hamdani, Hiroshige Kikura, Shun Kimura, Keisuke Tsukada, Daisuke Sasa and Shuichi OOmori, Development of Fuel Debris Inspection Methods Using Air Coupled Ultrasound, *ASTECHNOVA 2016 International Energy Conference*, November 2-3, 2016, Yogyakarta, Indonesia, pp. 140-146.

(18) Shun Kimura, Kazumi Kitayama, Kazushi Kimoto, Katsuyuki Kawamura and Hiroshige Kikura: A Fundamental Study on Measurement of Elastic Properties in Compacted Bentonite by Ultrasonic Velocity Measurement; *The 37th Symposium on Ultrasonic Electronics*, November 16-18, 2016, Busan, Korea, Proceedings of Symposium on Ultrasonic Electronics, Vol. 37 (2016), 3E1-1.

(19) Shun Kimura, Kazumi Kitayama, Kazushi Kimoto, Katsuyuki Kawamra and Hiroshige Kikura, Ultrasonic Measurement of Water Content Variation in Compacted Bentonite, *The 5th International Symposium on Innovative Nuclear Energy Systems* (INES-5), October 31-November 2, 2016, Tokyo, Japan, Paper No. B-21-4.

(20) Kensuke Tsukada and Hiroshige Kikura, Study on Velocity Profile Measurement of Saturated Steam Jet Flow by Air-coupled Ultrasound, *The 5th International Symposium on Innovative Nuclear Energy Systems* (INES-5), October 31-November 2, 2016, Tokyo, Japan, Paper No. B31-3.
(21) Antonin Povolny and Hiroshige Kikura, Recent Improvements of Ultrasound Reflector Recognition and Tracking Technique for Bubbly Flow Measurement, *The 11th International Topical Meeting on Nuclear Thermal-Hydraulics, Operation and Safety* (NUTHOS-11), GOctober 10-13, 2016, Gyeongju, Korea, pp.1-12, Paper No. N11A0200.
(22) Tat Thang Nguyen, Hideki Murakawa, Ngoc Hai Duong and Hiroshige Kikura, Development of a budget multiwave UVP system for two-phase flow measurement and some applications, *The 10th International Symposium on Ultrasonic Doppler Methods for Fluid Mechanics and Fluid Engineering* (ISUD10), September 28-29, 2016, Tokyo, Japan, pp. 33-36.
(23) Antonin Povolny, Tomonori Ihara and Hiroshige Kikura, The signal processing of Ultrasonic reflector recognition and tracking technique, *The 10th International Symposium on Ultrasonic Doppler Methods for Fluid Mechanics and Fluid Engineering* (ISUD10), September 28-29, 2016, Tokyo, Japan, pp. 53-56.
(24) Keisuke Tsukada and Hiroshige Kikura, Development of focused air-coupled ultrasound velocity profiler for steam jet flow velocity measurement, *The 10th International Symposium on Ultrasonic Doppler Methods for Fluid Mechanics and Fluid Engineering* (ISUD10), September 28-29, 2016, Tokyo, Japan, pp.73-76.
(25) Jiaju ZHOU, Tomonori Ihara and Hiroshige Kikura, Low Velocity Measurement on The Joule-Heating Flow by Ultrasound Velocity Profiler Method, *The 10th International Symposium on Ultrasonic Doppler Methods for Fluid Mechanics and Fluid Engineering* (ISUD10), September 28-29, 2016, Tokyo, Japan, pp. 89-92.
(26) Hiroshige Kikura, Tomonori Ihara and Ari Hamdani, Development of Two-dimensional Vector UVP with Phased Array Technique, *The 10th International Symposium on Ultrasonic Doppler Methods for Fluid Mechanics and Fluid Engineering* (ISUD10), September 28-29, 2016, Tokyo, Japan, pp. 93-96.
(27) Tomonori Ihara, Keisuke Tsukada, Hiroshige Kikura and Horst-Michael PRASSER, Bubbly Flow Measurement in High Temperature Molten Salt, The 10th International Symposium on Ultrasonic Doppler Methods for Fluid Mechanics and Fluid Engineering (ISUD10), September 28-29, 2016, Tokyo, Japan, pp.129-132.
(28) Jiaju ZHOU, Nobuyoshi Tsuzuki and Hiroshige Kikura, Numerical simulation of Joule-heating flow in a cuboid cavity by GSMAC Method, *11th International Conference on Advances in Fluid Mechanics* (AFM2016), September 5-7, 2016, Ancona, Italy, pp. 127-138.
(29) Keisuke Tsukada and Hiroshige Kikura, Flowrate measurement on metal pipes by air-coupled ultrasound, *11th International Conference on Advances in Fluid Mechanics* (AFM2016), September 5-7, 2016, Ancona, Italy, pp. 151-162.
(30) Antonin Povolny, Hiroshige Kikura, Ultrasound Reflector Recognition and Tracking Technique for Two-Phase Flow, *The 24rd International Conference on Nuclear Engineering* (ICONE24), June 26-30, 2016, Charlotte, USA, Paper No. ICONE24-60594.
(31) Keisuke Tsukada and Hiroshige Kikura, Study of Steam Flow Velocity Measurement using Focused Air-Coupled Ultrasonic Velocity Profiler, *The 17th International Symposium on Flow Visualization* (ISFV-17), June 19-22, 2016, Gatlinburg, USA, Paper No. 109-167-1-RV.
(32) Robert Malkin, Takuya Kawachi, Hiroshige Kikura and Bruce W. Drinkwater, Imaging and Characterizartion of Nuclear Fuel Debris using Acoustic Arrays, *The 8th European Review Meeting on Severe Accident Research* (ERMSAR 2017), May 16-18, 2016, Warsaw, Poland, Papeer No.516.
(33) Takuya Kawachi, Tomonori Ihara and Hiroshige Kikura, A Study on Ultrasonic Visualization Technique for Leakage and Fuel Debris Inspection, *International Conference on Advancing the Global Implementation of Decommissioning of Environmental Remediation Programmes* ; IAEA,May 23-27, 2016, Madrid, Spain (2016-5), Paper No. ID68.
(34) Antonin Povolny, Hiroshige Kikura and Tomonori Ihara, Ultrasound Reflector Recognition and Tracking Technique for Gas Bubbles in Liquid, *ICMF 2016 International Conference on Multiphase Flow*, May 22-27, 2016, Firenze, Italy, pp.1-5, Paper No. ICMF2016-628.
(35) Mikio Shimada, Fumio Matsuzaki, Tomohiro Matsumoto, Kenshi Komatsu: Influence of ionizing radiation induced DNA damage and centrosome overduplication in mouse embryonic neural development; *The 7th International Society of Radiation Neurobiology Conference*, Yuzawa, Japan, Feb. 2017.
(36) Naoya Kase, Mikio Shimada, Yoshihisa Matsumoto: The role of DNA repair factor Polynucleotide kinase/phosphatase (PNKP) in DNA replication; *The 7th International Society of Radiation Neurobiology Conference*, Yuzawa, Japan, Feb. 2017.
(37) Shunsuke Hosoda, Satoshi Kohno, Mari Aida, Ken Kakegawa, tomoko miyake, Takahiro Iwai, hidekadzu miyahara, Mikio Shimada, Yoshihisa Matsumoto, Akitoshi Okino: Single Cell Elemental Analysis of Human Cells Using Droplet Injection ICP-AES/MS; *SciX 2016*, Page 81, Sep. 2016.
(38) A. R. Amiri Moghani, R Wanotayan, M. K. Sharma, A. D. A. De Castro, M Shimada, Y Matsumoto: DNA damage-induced phosphorylation of XRCC4 and its

role in DNA double strand break repair; *The fifth international symposium on innovative nuclear energy systems*, Tokyo, Japan, Nov. 2016.

(39) M Shimada, H Tsuchiya, Y Matsumoto: Ionizing radiation induce genome instability through centrosome over duplication and ciliogenesis; *The fifth international symposium on innovative nuclear energy systems*, Tokyo, Japan, Nov. 2016.

(40) S. Chiba, K. Nishio, Y. Aritomo, H. Koura, O. Iwamoto. H. Makii, I. Nishinaka and K. Hirose: A comprehensive Approach to Determination of Nuclear Data of Unstable Nuclei; EPJ Web of Conferences **106**, 04004 (2016).

(41) Tadashi Yoshida, Takahiro Tachibana, Satoshi Chiba: Analysis of Electron and Antineutrino Energy Spectra from Fissile Samples under Irradiation based on Gross Theory of Beta-decay; *5th International Workshop on Compound-Nuclear Reactions and Related Topics (CNR*15)*, EPJ Web of Conferences **122**, 10002 (2016).

(42) Chikako Ishizuka, Satoshi Chiba, Alexander V. Karpov, Yoshihiro Aritomo: Isotopic distribution of ^{235}U+n➔^{236}U" at low E* using 4D-Langevin calculation; *The 2015 Symposium on Nuclear Data*, JAEA-Conf **2016-004**, 99 (2016).

(43) Chikako Ishizuka, Satoshi Chiba, Alexander V. Karpov, Yoshihiro Aritomo: Dynamical approach to isotopic-distribution of fission fragments from actinide nuclei; *5th International Workshop on Compound-Nuclear Reactions and Related Topics (CNR*15*, EPJ Web of Conferences **122**, 01003 (2016).

(44) Hiroshi Akatsuka, Yurina Honda, Alejandro Álvaro-González, Atsushi Nezu: Spectroscopic Examination of Fulcher-α Band of Microwave Discharge H_2-D_2 and H_2-He Plasmas, *PLASAS-8*, April 9 – 10, 2016, Xian, China, 5.

(45) Jun Takeda, Atsushi Nezu, Hiroshi Akatsuka: Effect of the Radial Electric Field on the Plasma Flow through a Magnetic Channel with Magnetized Electrons and Non-Magnetized Ions; *18th International Congress on Plasma Physics (ICPP2016)*, June 27 – July 1, 2016, Kaohsiung, Taiwan, PAM1-2.

(46) Hiroshi Akatsuka, Jun Takeda, Atsushi Nezu: Azimuthal ExB Drift of Electrons Induced by the Radial Electric Field Flowing through a Longitudinal Magnetic Channel with Non-Magnetized Ions; *69th Annual Gaseous Electronics Conference (GEC2016)*, October 10 – 14, 2016, Bochum, Germany, MW6.44.

(47) Hiroshi Akatsuka, Yoshinori Tanaka: Statistical Physics of Electron Temperature of Low-Pressure Discharge Nitrogen Plasma with Non-Maxwellian EEDF; *69th Annual Gaseous Electronics Conference (GEC2016)*, October 10 – 14, 2016, Bochum, Germany, MW6.45.

(48) Ampan Laosunthara, Hiroshi Akatsuka: Hybrid Simulation of Supersonic Flow of Weakly Ionized Plasma along Open Field Magnetic Line Effect of Background Pressure; *69th Annual Gaseous Electronics Conference (GEC2016)*, October 10 – 14, 2016, Bochum, Germany, QR4.3.

(49) Hiroshi Akatsuka, Yurina Honda, Alejandro Álvaro-González, Atsushi Nezu: Spectroscopic Examination of Fulcher-α Band of Microwave Discharge H_2-D_2 and H_2-He Plasmas; *5th International Symposium on Innovative Nuclear Energy Systems (INES-5)*, October 31 – November 2, 2016, Tokyo, Japan, B32-2.

(50) Hao Tan, Atsushi Nezu, Hiroshi Akatsuka: Spectroscopic Study on Chemical Kinetics of NO(A, B, C) States in Low-Pressure N_2-O_2 Microwave Discharge; *38th International Symposium on Dry Process (DPS2016)*, November 21 – 22, 2016, Sapporo, Japan, P-30.

(51) Masahiro Susa, Yuuta Kouno, Rie Endo, Yoshinao Kobayashi. Effects of CaF2 on the radiative heat transfer in mould fluxes for continuous steel casting, MOLTEN16, May. 2016.

(52) Min Wang, Rie Endo, Yoshinao Kobayashi, Dou Zuoyong, Masahiro Susa. Reduction of iron oxides in mould fluxes with additions of CaSi2, May. 2016.

(53) Hiroshi Sagara, Kazuki NAKAHARA, Chi Young HAN. Estimation technique of Cs retention fraction in irradiated nuclear fuel with intact/damaged form, Trans. Ame. Nucl. Soc., Vol. 115, pp. 913-914, Nov. 2016.

(54) Takeshi Aoki, Sunil S. Chirayath, Hiroshi Sagara. Material Balance Area Design for the Transuranic Fuel Cycle Employing High Temperature Gas Cooled Reactors, Trans. Ame. Nucl. Soc, Vol. 115, pp. 909-912, Nov. 2016.

(55) Rei Kimura, Hiroshi Sagara, Satoshi Chiba. Precision requirement of the photofission cross section for the nondestructive assay technique, ND2016, Sep. 2016.

(56) Takehiko Tsukahara, Kaname Saga, Kyojiro Morikawa, Ki Chul Park, DEVELOPMENT OF STIMUTI-RESPONSIVE GEL PHOTONIC-CRYSTAL MICROCHIP FOR METAL ION SENSING, *Proceedings of Micro-TAS 2016*, 1252-1254 (2016).

(57) Kyojiro Morikawa and Takehiko Tsukahara, EVALUATION OF LIQUID PROPERTIES OF TRIVALENT ION SOLUTION FOR ION SEPARATION USING EXTENDED NANOFLUIDIC CHANNELS, *Proceedings of Micro-TAS 2016*, 806-808 (2016).

(58) Kyojiro Morikawa, Yutaka Kazoe and Takehiko Tsukahara, DEVELOPMENT OF DIFFUSION OSMOTIC STREAMING CURRENT MEASUREMENT SYSTEM IN EXTENDED NANOSPACES FOR NON-PROBE ION MOBILITY MEASUREMENT, *Proceedings of Micro-TAS 2016*, 760-762 (2016).

(59) Kyojiro Morikawa, Sachiko Ishihara and Takehiko Tsukahara, DEVELOPMENT OF TiO2 NANOPILLAR PATTERNED CHIP FOR NANO-DROPLETS FORMATION USING

EXTENDED NANOCHANNELS, *Proceedings of Micro-TAS 2016*, 748-750 (2016).

(60) Yuki Maehara, Masatoshi KONDO, Minoru Takahashi. STUDY ON STABILITY OF LIQUID JET FOR LIQUID LITHIUM TARGET OF BORON NEUTRON CAPTURE THERAPY (BNCT), 2016 24th International Conference on Nuclear Engineering (ICONE24), Proceedings of the 2016 24th International Conference on Nuclear Engineering (ICONE24), The American Society of Mechanical Engineers, Jun. 2016.

(61) Sho Tanabe, Dan Tri Le, Masatoshi KONDO, Minoru Takahashi. EXPERIMENTAL STUDY ON CRITICAL HEAT FLUX IN THREE PIN BUNDLE WITH WIRE SPACER FOR BOILING WATER REACTOR, 2016 24th International Conference on Nuclear Engineering (ICONE24), Proceedings of 2016 24th International Conference on Nuclear Engineering (ICONE24), The American Society of Mechanical Engineers, Jun. 2016.

Oral Presentation in international or domestic conferences

(1) Odmaa Sambuu, Enkhbaatar Ganbold, Jamyansuren Terbish, Toru Obara, Norov Nanzad, Munkhbat Byambajav: Design Parameters in an Annular, Prismatic HTGR for Passive Decay Heat Removal; *Abstracts of the fifth International symposium on Innovative Nuclear Energy Systems (INES-5)*, A21-3, October 31 – November 2, 2016, Tokyo (2016).

(2) Irwan Liapto Simanullang, Toru Obara: Utilization of Burnable Poison Particles in UO_2 and ROX Fuels in Pebble Bed Reactor with Accumulative Fuel Loading Scheme; *Abstracts of the fifth International symposium on Innovative Nuclear Energy Systems (INES-5)*, A21-1, October 31 – November 2, 2016, Tokyo (2016).

(3) Toru Obara, Kazuki Kuwagaki, Jun Nishiyama: Concept of Burning Wave Reactor with Rotational Fuel Shuffling; *Abstracts of the fifth International symposium on Innovative Nuclear Energy Systems (INES-5)*, A13-5, October 31 – November 2, 2016, Tokyo (2016).

(4) Van Khanh Hoang, Toru Obara: Impact of Neutron Spectrum Shift on Breed and Burn Reactor Concept; *Abstracts of the fifth International symposium on Innovative Nuclear Energy Systems (INES-5)*, A12-5, October 31 – November 2, 2016, Tokyo (2016).

(5) Jun Nishiyama, Masato Tanaka, Toru Obara: Study on Optimization of Early Stage CANDLE Burnup Characteristics; *Abstracts of The fifth International symposium on Innovative Nuclear Energy Systems (INES-5)*, A11-4, October 31 – November 2, 2016, Tokyo (2016).

(6) Hiroki Osato, Jun Nishiyama, Toru Obara: Study on CANDLE Burning Reactor with Initial Core Using Plutonium from LWR Spent Fuel; *Abstracts of the fifth International symposium on Innovative Nuclear Energy Systems (INES-5)*, A11-2, October 31 – November 2, 2016, Tokyo (2016).

(7) T. Obara, J. Abdul Karim, V.K. Hoang, J. Nishiyama: CANDLE BURNING FAST REACTOR CONCEPT WITH MELT AND REFINING PROCESS; *Book of abstracts of International Scientific and Technical Conference, Innovative Designs and Technologies of Nuclear Power IV (IV ISTC NIKIET-2016)*, pp.75-76, September 27-30, 2016, Moscow, Russia (2016).

(8) Kazuki Kuwagaki, Jun Nishiyama, Toru Obara: Feasibility of Breed and Burn Reactor with Continuous Fuel Moving; *Proc. of 2017 annual meeting of Atomic Energy Society of Japan*, 3F16 (2017).

(9) Hiroki Osato, Jun Nishiyama, Toru Obara: Initial Core Design of CANDLE Burning Fast Reactor Using Plutonium from LWR Spent Fuel; *Proc. of 2017 annual meeting of Atomic Energy Society of Japan*, 3F15 (2017).

(10) Isamu Sato1, Toru Obara, Toyohiko Yano, Kenji Takeshita, Yukitaka Kato, Hiroshi Akatsuka, Hiroshige Kikura, Takehiko Tsukahara, Katsumi Yoshida, Gen Endo, Koichiro Takao, Masayuki Harada, Saishun Yamazaki, Nobuyuki Iwatsuki, Koichi Suzumori1, Noriko Asanuma, Tsuyoshi Arai, Kenji Kawashima, Naoyuki Takaki: The Center of World Intelligence Project for Nuclear S&T and Human Resource Development: Human Resource Development and Research Program for Decommissioning of Fukushima Daiichi NPS (Nuclear Power Station) (2)-Tokyo Institute of Technology "Advanced Research and Education Program for Nuclear Decommissioning" Implementation Status –; *Proc. of 2016 autumn meeting of Atomic Energy Society of Japan*, 3M02(2016).

(11) Toru Obara, Koji Okamoto, Nobuyoshi Hara, Yoshinari Anoda, Seichi Sato, Yoshitaka Takagai, Ikuo Towhata, Isamu Sato: The Center of World Intelligence Project for Nuclear S&T and Human Resource Development, Human Resource Development and Research Program for Decommissioning of Fukushima Daiichi NPS (Nuclear Power Station) (1)- Outline of Activity -; *Proc. of 2016 autumn meeting of Atomic Energy Society of Japan*, 3M01(2016).

(12) Tuya Delgersaikhan, Jun Nishiyama, Toru Obara: Supercritical transient analysis in light water moderated coupled small fuel debris regions using integral kinetic model and point kinetic model; *Proc. of 2016 autumn meeting of Atomic Energy Society of Japan*, 1H12(2016).

(13) Hiroki Osato, Jun Nishiyama, Toru Obara: Thermal Hydraulic Analysis on CANDLE Burning Reactor with Initial Core Using Plutonium from LWR Spent Fuel; *Proc. of 2016 autumn meeting of Atomic Energy Society of Japan*, 1L12(2016).

(14) Irwan Liapto Simanullang, Jun Nishiyama, Toru Obara: Introduction of rock-like oxide fuel in PBR

with accumulative fuel loading Scheme; *Proc. of 2016 autumn meeting of Atomic Energy Society of Japan*, 1L08(2016).

(15) T. Ohtaki, H. Iguchi. K. Fujioka, Y. Kato, "Reactivity evaluation of thermochemical energy storage materials using calcium chloride / water system in packed bed reactor", 54th Japan Heat Transfer Sympodium, 25 May, 2017, Ohmiya.

(16) K. Nishida, T. Yamamoto, M. Zamengo, Y. Kada, Y. Okano, "Understanding of Heat Transfer in a Packed Bed Reactor Using Thermochemical Heat Storage Material", 54th Japan Heat Transfer Sympodium, 25 May, 2017, Ohmiya.

(17) T. Ohtaki, H. Iguchi, K. Fujioka, Y. Kato, "Reactivity evaluation of thermochemical energy storage materials using calcium chloride / water system in packed bed reactor", JSME ICMS 2017 Summer Meeting, 12 June, 2017, Tokyo.

(18) S. Funayama, Y. Kato, "Evaluation of thermochemical energy storage and output performance of a packed bed of $Ca(OH)_2$ pellets", JSME ICMS 2017 Summer Meeting, 12 June, 2017, Tokyo.

(19) H. Takasu, Y. Kato, "Study on high temperature thermochemical energy storage system using lithium orthosilicate", Regular Meeting of 54th Committee on ironmaking of JSPS, Nagoya, 30 June, 2017.

(20) Y. Kato, "Subejects and Solutions for development of thermal energy storage", ISIJ Ecotechnology Forum, 14 July, 2017, Tokyo.

(21) K. Nishida, M. Zamengo, Y. Kato, Okano, "Packed bed heat transfer analysis of MgO/H2O thermochemical energy storage", SCEJ 49th Autumun Meeting, 21 September, 2017, Nagoya.

(22) J. Balibrea-Correa, Tatsuya Katabuchi (54th author), n_TOF Collaboration (120 authors). Measurement of the neutron capture cross section of the fissile isotope ^{235}U with the CERN n_TOF total absorption calorimeter and a fission tagging based on micromegas detectors, ND 2016: International Conference on Nuclear Data for Science and Technology, 11-16 Sep. 2016.

(23) F. Mingrone, Tatsuya Katabuchi (50th author), n_TOF Collaboration (117 authors). High-precision measurement of the radiative capture cross section of ^{238}U at the n_TOF CERN facility, ND 2016: International Conference on Nuclear Data for Science and Technology, 11-16 Sep. 2016.

(24) Taro Nakao, Kazushi Terada, Atsushi Kimura, Shoji Nakamura, Osamu Iwamoto, Hideo Harada, Tatsuya Katabuchi, M. Igashira, J. Hori. Developments of a new data acquisition system at ANNRI, ND 2016: International Conference on Nuclear Data for Science and Technology, 11-16 Sep. 2016.

(25) Seigo Umezawa, M. Igashira, Tatsuya Katabuchi, Dominic Moraru, S. Yanagida, T. Okamiya. Measurement of keV-neutron capture cross sections and capture gamma-ray spectra of Cs-133 and I-127, ND 2016: International Conference on Nuclear Data for Science and Technology, 11-16 Sep. 2016.

(26) E. Mendoza, Tatsuya Katabuchi (58th author), n_TOF Collaboration (124 authors). Measurement of the 241Am neutron capture cross section at the n_TOF facility at CERN, ND 2016: International Conference on Nuclear Data for Science and Technology, 11-16 Sep. 2016.

(27) Hideo Harada, Osamu Iwamoto, Nobuyuki Iwamoto, Atsushi Kimura, Kazushi Terada, Taro Nakao, Kazuhiro Mizuyama, M. Igashira, Tatsuya Katabuchi, Tadafumi Sano, Yuji Shibahara, Yoshiyuki Takahashi, Koichi Takamiya, Cheol Ho Pyeon, Satoshi Fukutani, Toshiyuki Fujii, J. Hori, Hiroshi Yashima. Research and development for accuracy improvement of neutron nuclear data on minor actinides, ND 2016: International Conference on Nuclear Data for Science and Technology, 11-16 Sep. 2016.

(28) Y.H. Chen, Tatsuya Katabuchi (47th author), n_TOF Collaboration (134 authors). Characterization of the n_TOF EAR-2 neutron beam, ND 2016: International Conference on Nuclear Data for Science and Technology, 11-16 Sep. 2016.

(29) M. Sabaté-Gilarte, Tatsuya Katabuchi (63rd author), n_TOF Collaboration (132 authors). The 33S(n,α)30Si cross section measurement at n_TOF-EAR2 (CERN): From 0.01 eV to the resonance region, ND 2016: International Conference on Nuclear Data for Science and Technology, 11-16 Sep. 2016.

(30) Emmeric Dupont, Tatsuya Katabuchi (101st author), n_TOF Collaboration (227 authors). Dissemination of data measured at the CERN n_TOF facility, ND 2016: International Conference on Nuclear Data for Science and Technology, 11-16 Sep. 2016.

(31) M. Barbagallo, Tatsuya Katabuchi (58th author), n_TOF Collaboration (134 authors). ^{7}Be(n,α) and ^{7}Be(n,p) cross section measurement for the cosmological lithium problem at the n_TOF facility at CERN, ND 2016: International Conference on Nuclear Data for Science and Technology, 11-16 Sep. 2016.

(32) F. Gunsing, Tatsuya Katabuchi (68th author), n_TOF Collaboration (152 authors). The measurement programme at the neutron time-of-flight facility n_TOF at CERN, ND 2016: International Conference on Nuclear Data for Science and Technology, 11-16 Sep. 2016.

(33) A. Stamatopoulos, Tatsuya Katabuchi (68th author), n_TOF Collaboration (133 authors). Measurement of the 240Pu(n,f) cross section at the CERN n_TOF facility: First results from experimental area II (EAR-2), ND 2016: International Conference on Nuclear Data for Science and Technology, 11-16 Sep. 2016.

(34) Nobuyuki Iwamoto, Tatsuya Katabuchi. Evaluation of neutron total and capture cross sections on ^{99}Tc in the unresolved resonance region, ND 2016: International Conference on Nuclear Data for Science and Technology, 11-16 Sep. 2016.

(35) Atsushi Kimura, Shoji Nakamura, M. Igashira, Motoharu Mizumoto, Hideo Harada, Yosuke Toh, Tatsuya Katabuchi, J. Hori. Neutron capture cross section measurements of ^{120}Sn, ^{122}Sn and ^{124}Sn with the array of Ge spectrometer at the J-PARC/MLF/ANNRI, ND 2016: International Conference on Nuclear Data for Science and Technology, 11-16 Sep. 2016.

(36) M. Mastromarco, Tatsuya Katabuchi (44th author), n_TOF Collaboration (111 authors). The ^{236}U neutron capture cross section measured at the n_TOF CERN facility, ND 2016: International Conference on Nuclear Data for Science and Technology, 11-16 Sep. 2016.

(37) Tatsuya Katabuchi, M. Igashira, Atsushi Kimura, Taro Nakao, Nobuyuki Iwamoto, Hideo Harada, Koichi Kino, Motoharu Mizumoto, Kazushi Terada, Shoji Nakamura, Osamu Iwamoto, Kazuhito Mizuyama, J. Hori. Measurement of the neutron capture cross section of 99Tc using ANNRI at J-PARC, ND 2016: International Conference on Nuclear Data for Science and Technology, 11-16 Sep. 2016.

(38) Tatsuya Katabuchi, Masayuki Igashira, Kazushi Terada, Atsushi Kimura, Shoji Nakamura, Taro Nakao, Osamu Iwamoto, Nobuyuki Iwamoto, Hideo Harada, Jun-Ichi Hori, Measurement of Neutron Capture Cross Section of Am-241 using ANNRI-NaI(Tl) Spectrometer at J-PARC, *2016 Fall Meeting of the Atomic Energy Society of Japan*, Sep. 7-9, 2016, O02.

(39) Hideo Harada, Osamu Iwamoto, Nobuyuki Iwamoto, Atsushi Kimura, Kazushi Terada, Taro Nakao, Shoji Nakamura, Kazuhito Mizuyama, Masayuki Igashira, Tatsuya Katabuchi, Tadafumi Sano, Yuji Shibahara, Yoshiyuki Takahashi, Koichi Takamiya, CheolHo Pyeon, Satoshi Fukutani, Toshiyuki Fujii, Jun-ichi Hori, Hiroshi Yashima, R&D for accuracy improvement of neutron nuclear data on minor actinides (1) A summary of progress in the AIMAC project, 2*017 Annual Meeting of the Atomic Energy Society of Japan*, Mar. 27-29, 2017, 3E01.

(40) Taro Nakao, Kazushi Terada, Atsushi Kimura, Shoji Nakamura, Osamu Iwamoto, Hideo Harada, Masayuki Igashira, Tatsuya Katabuchi, Jun-ichi Hori, R&D for accuracy improvement of neutron nuclear data on minor actinides (2) Technical developments for accurate determination of amount of radioactive samples using micro-calorimeter, 2*017 Annual Meeting of the Atomic Energy Society of Japan*, Mar. 27-29, 2017, 3E02.

(41) Atsushi Kimura, Shoji Nakamura, Kazushi Terada, Taro Nakao, Hideo Harada, Tatsuya Katabuchi, Masayuki Igashira, Satoshi Fukutani, Toshiyuki Fujii, Jun-ichi Hori, R&D for accuracy improvement of neutron nuclear data on minor actinides (4) Measurements of neutron capture and total cross sections of ^{243}Am with ANNRI at J-PARC, 2*017 Annual Meeting of the Atomic Energy Society of Japan*, Mar. 27-29, 2017, 3E04.

(42) Tatsuya Katabuchi, Masayuki Igashira, Kazushi Terada, Atsushi Kimura, Shoji Nakamura, Taro Nakao, Osamu Iwamoto, Nobuyuki Iwamoto, Hideo Harada, Jun-ichi Hori, R&D for accuracy improvement of neutron nuclear data on minor actinides (7) Measurements of neutron capture cross sections in fast neutron energy region with ANNRI at J–PARC, 2*017 Annual Meeting of the Atomic Energy Society of Japan*, Mar. 27-29, 2017, 3E07.

(43) Karin Takabe, Masayuki Igashira, Tatsuya Katabuchi, Chika Sekine, Seigo Umezawa, Ryo Fujioka, Measurement of the keV-Neutron Capture Cross Sections and Gamma-ray Spectra of Rhenium Isotope, 2*017 Annual Meeting of the Atomic Energy Society of Japan*, Mar. 27-29, 2017.

(44) Kaoru Hara, Nobuya Fujii, Takashi Kamiyama, Yuki Narita, Hirotaka Sato, Tatsuya Katabuchi, Shoji Nakamura, Yosuke Toh, Measurements of neutron capture cross section of 35Cl using NaI(Tl) spectrometer in ANNRI, 2*017 Annual Meeting of the Atomic Energy Society of Japan*, Mar. 27-29, 2017.

(45) San Shwin, Ari Hamdani, Shun Kimura Nobuyuki Fujisawa and Hiroshige Kikura, Velocity Measurement on Turbulent Swiring Flow by Ultrasonic Technique, *Young Researcher Exchange Forum at Thermal Hydrauric Division of Atomic Energy Society of Japan* (AESJ), March 29, 2017, Kanagawa, Japan, P42.

(46) Weichen Zhang, Xingguo Wang, Junjie Chang, Hideharu Takahashi, Yasuhiko Ougiya and Hiroshige Kikura, Estimation of Effect for Velocity Profile in Pipe Flow by Pipe Damage from Erosion-corrosion, *Young Researcher Exchange Forum at Thermal Hydrauric Division of Atomic Energy Society of Japan* (AESJ), March 29, 2017, Kanagawa, Japan, P44. (in Japanes).

(47) Weichen Zhang, Xingguo Wang, Junjie Chang, Hideharu Takahashi, Yasuhiko Ougiya and Hiroshige Kikura, Study of effect of Velocity Profile from Pipe Damage using Ultrasound, *Student poster workshop 2017 spring meeting of the Atomic Energy Society of Japan*, March 28, 2017, Kanagawa, Japan, P23. (in Japanese).

(48) Hidetoshi Okada, Shunsuke Uchida, Masanori Naitoh, Nobuyoshi Tsuduki and Hironari Kikura; Risk Based Strategies for Inspection and Maintenance of Nuclear Power Plants (1) Risk Based Inspection for Major Phenomena for the Level 4 of the “Defense in Depth”, *AESJ Spring meetings 2017*, March 27-29, Kanagawa, Japan, 3K-07. (in Japanese).

(49) Shunsuke Uchida, Hidetoshi Okada, Masanori Naitoh, Nobuyoshi Tsuduki and Hironari Kikura, Risk Based Strategies for Inspection and Maintenance of Nuclear Power Plants, (2) An Example for Risk Based Inspection for the Events Originating FAC Related Causes, *AESJ Spring meetings 2017*, March 27-29, Kanagawa, Japan,

3K-08. (in Japanese).
(50) Munkhbat Batsaikhan, Ari Hamdani, Hiroshige Kikura, Experiemntal Studay of Air-water Bubbly Column by using Ultrasonic Velocity Profiler (UVP) and Particle Image Velocimetry (PIV), *The 10th Student Research Workshop of the Atomic Energy Society of Japan Kanto-Koetsu Branch*, March 28, 2017, Kanagawa, Japan, B18.
(51) Gen Endo and Hiroshige Kikura, An Ultrasonic Measurement System and its Robotic Deployment into Vessels for the Combined Assessment of Debris Condition and Water Leakage, *England-Japan Reserch Showcase for International Collabolating Research Maching*, March 26, 2016.
(52) Hironobu Kiuchi, Shun Kimura, Hiroshige Kikura, Daisuke Sasa, Shuichi Omori: Fundamental study on shape measurement of specimens in imitation of debris by air-coupled ultrasound; *The 56th Student Research Workshop of the Japan Society of Mechanical Engineers Kanto Branch*, March 16, 2017, Tokyo, Japan, Paper No. 717. (in Japanese).
(53) Ryo Nishiwaki, Shun Kimura, Hideharu Takahashi, Hiroshige Kikura: Fundamental study of ultrasonic velocity profiler method for flow measurement and robot transport; *The 10th Students' Research Workshop of the Atomic Energy Society of Japan Kanto-Koetsu Branch*, March 10, 2017, Kanagawa, Japan, A22. (in Japanese)
(54) Shun Kimura and Hiroshige Kikura, Study of Evaluation on Measurement of Elastic Properties in Compacted Bentonite by Transverse and Longitudinal Wave of Ultrasound, *Depth (shallow) Geological Environment Workshop on Materials Science*, Okayama, March 10, 2017, Paper No. 5.
(55) Hironobu Kiuchi, Shun Kimura, Hiroshige Kikura, Daisuke Sasa, Shuichi Omori: Fundamental study on measurement of fuel debris' surface shape by air-coupled ultrasound; *Conference for R&D Initiative on Nuclear Decommissioning Technology by the Next Generation*, March 7, 2017, Tokyo, Japan, Paper No. D-8. (in Japanese)
(56) Hiroshige Kikura, Background and Objectives, *The 3rd workshop on UK-Japan Civil Nuclear Energy Collaboration (Ultrasonic-Robotics Integration for Determination of Leakage from Reactor Vessel and Debris Inspection)*, February 2, 2017, Bristol, England.
(57) Tomonori Ihara and Hiroshige Kikura, Method and Apparatus Development, *The 2nd workshop on UK-Japan Civil Nuclear Energy Collaboration (Ultrasonic-Robotics Integration for Determination of Leakage from Reactor Vessel and Debris Inspection)*, February 2, 2017, Bristol, England.
(58) Gen Endo, Hiroshige Kikura, Nobuyoshi Tsuzuki, Kazushi Kimoto, Ryo Yanase, Hirotaka Komura, Yoshihide Nakamura, Hiroyuki Nabae and Koichi Suzumori, Proposal of a Robot System Transporting an Ultrasonic Sensor for Measuring Flows of Contaminated Water in Reacter, *The 17th SICE System Integration Division Annual Conference* (SI2016 Sapporo), December 15-17, 2016, Sapporo, Japan, pp. 477-480. (in Japanese).
(59) Shun Kimura, Kazumi Kitayama, Kazushi Kimoto, Katsuyuki Kawamura and Hiroshige Kikura: A Study of the Effect of Degree of Saturation on Ultrasonic Velocity in Unsaturated Compacted Bentonite; *The Fifth International Education Forum on Environment and Energy Science*, December 15-19, 2016, California, USA, B211.
(60) Hiroshige Kikura, Academy for Global Nuclear Safety and Security Agent (3): Nuclear Safety and Security Courses, III Simulation of Severe Nuclear Accidents, *The 37th Annual Meeting of Institute of Nuclear Materials Management* (INMM) Japan Chapter, November 17-18, 2016, Toyko, Japan, #3724. (in Japanese).
(61) Tomonori Ihara, Hiroshige Kikura and Hideki Murakawa, Development of Ultrasonic Velocity Profiler for Measurement of Multiphase Flow, *JSME Fluid Engineering Devision Conference 2016*, November 12-13, 2016, Ube, Japan, Paper No.0507. (in Japanese)
(62) Shun Kimura, Kazumi Kitayama, Kazushi Kimoto, Katsuyuki Kawamura, and Hiroshige Kikura, A Fundamental Study on Measurement of Elastic Properties in Compacted Bentonite by Ultrasonic Velocity Measurement, *The 37th Symposium on Ultrasonic Electronics*, November 16-18, 2016, Busan, Korea, Paper No. 3E1-1.
(63) Hironobu Kiuchi, Shun Kimura, Hiroshige Kikura, Daisuke Sasa and Shuichi Omori, Fundamental study on three-dimensional measurement of object shape by air-coupled ultrasound, *The 15th Wakate-Kenkyusha-Happyou-Touronkai*, AESJ Kantoukouetsu-Branch, November 2, 2016, Tokyo, Japan, Paper No. A-11.
(64) Vien Tri Tran, Thang Tst Nguyen, Ari Hamdani, Keisuke Tsukada, Hiroshige Kikura, Measurement of Subcooled Boiling Flow by Using Ultrasonic Technique, The 15th Wakate-Kenkyusha-Happyou-Touronkai, *AESJ Kantoukouetsu-Branch*, November 2, 2016, Tokyo, Japan, Paper No. A-12.
(65) San Shwin, Ari Hamdani, Hiroshige Kikura, Flow Visualization on Downstream of the Double Bent Pipe by Phased Array Ultrasonic Velocity Profile Method, The 15th Wakate-Kenkyusha-Happyou-Touronkai, *AESJ Kantoukouetsu-Branch*, November 2, 2016, Tokyo, Japan, Paper No. A-13.
(66) Munkhbat Batsaikhan, Antonin Povolny, Ari Hamdani, Hiroshige Kikura, Development of Phased Array-Ultrasonic Velocity Profiler (PA-UVP) system, *The 15th Wakate-Kenkyusha-Happyou-Touronkai*, *AESJ Kantoukouetsu-Branch*, November 2, 2016, Tokyo, Japan, Paper No. A-14.
(67) Ryo Nishiwaki, Keisuke Tsukada, Shun Kimura, Hironobu Kiuchi, Hiroshige Kikura, Effects of

temperature gradient on ultrasonic velocity profile measurement, T*hermal engineering conference 2016 of the Japan Society of Mechanical Engineers*, October 22-23, 2016, Ehime, Japan, A233. (in Japanese).

(68) Hiroshige Kikura, Background and Objectives, *The 2nd workshop on UK-Japan Civil Nuclear Energy Collaboration (Ultrasonic-Robotics Integration for Determination of Leakage from Reactor Vessel and Debris Inspection)*, September 27, 2016, Tokyo, Japan.

(69) Tomonori Ihara and Hiroshige Kikura, Method and Apparatus Development, *The 2nd workshop on UK-Japan Civil Nuclear Energy Collaboration (Ultrasonic-Robotics Integration for Determination of Leakage from Reactor Vessel and Debris Inspection)*, September 27, 2016, Tokyo, Japan.

(70) Shun Kimura, Kazumi Kitayama, Kazushi Kimoto, Katsuyuki Kawamura and Hiroshige Kikura: Study of Estimation for Water Content Measurement by Ultrasound in Compacted Bentonite under Unsaturated Condition; *60th Annual Meeting of The Clay Science Society of Japan*, September 15-17, 2016, Fukuoka, Japan, A19. (in Japanese).

(71) Shun Kimura, Kazumi Kitayama, Kazushi Kimoto, Katsuyuki Kawamura and Hiroshige Kikura: A Study of Water Content Measurement by Ultrasound in Compacted Bentonite under Unsaturated Condition; *2016 Fall Meeting of the Atomic Energy Society of Japan*, September 7-9, 2016, Fukuoka, Japan, 2D12. (in Japanese).

(72) Hironobu Kiuchi, Shun Kimura, Keisuke Tsukada, Hiroshige Kikura, Daisuke Sasa and Shuichi Omori, Fundamental study on measurement of object shape and surface flow by air-coupled ultrasound, 2*016 JSEM Annual Conference on Experimental Mechanics*, September 1-3, 2016, Osaka, Japan, Paper No. A60. (in Japanese).

(73) Keisuke Tsukada and Hiroshige Kikura, Fundermental Study of Steam Jet Measurement by Air-Coupled Ultrasonic Velocity Profiler, *Multiphase Flow Symposium of Japanese Society for Multiphase Flow* (JSMF) 2016, August 8-10, 2016, Kyoto, Japan, P42-14. (in Japanese).

(74) Shun Kimura and Hiroshige Kikura, Development of Ultrasonic Measrement System for Leakage and Fuel Debris Inspection, *IRID Symposium 2016 in Tokyo: Develop the Future for Decommissioning*, August 4, 2016, Tokyo, Japan, P1-5. (in Japanese).

(75) Koki Aotsuka, Tatsuya Inagaki, Yoshihiko oishi, Hideki Kawai, Hideki Murakawa and Hiroshige Kikura, Spectrum analysis of chaotic state near end wall in Taylor-Couette flow with a small aspect ratio, Journal of the Visualization Society of Japan Vol. **36** Suppl. No. 1 (2016) , *The 44th Symposium on Visualization*, July 19-20, 2016, Tokyo, Japan, D113. (in Japanese).

(76) Hiroshige Kikura, Fundermental Study of Monitering System of Melted Glass Flow by using Puls Ultrasound, *1st Technical evoluation conference of New Glass Forum* (NGF), July 12, 2016, Tokyo, Japan. (in Japanese).

(77) Keisuke Tsukada, Taiki Aiba, Tatsuya Kawaguchi, Hiroshige Kikura, Katsuhiko Sugita and Shuichi Umezawa, Ultrasonic beam focusing for steam flowrate measurement in high temperature metal pipe, *JSME 21st National Symposium on Power and Energy Symposium*, June 16-17, 2016, Yokohama, Japan, pp.1-2. (in Japanese).

(78) Hiroshige Kikura, Study on Ultrasonic-Robotics Integration for Determination of Leakage from Reactor Vessel and Debris Inspection, *The 6th Vietnam/Japan Research/HRD Forum on Nuclear Technology*, May 19-20, 2016, Dalat, Vietnam.

(79) M.Nakase, T.Kobayashi, H.Shiwaku, S.Suzuki, T.Yaita: N,O-hybrid donor ligands for recognition and separation of f-series elements by solvent extraction; *EMN Orlando meeting on Actinide 2016*, Orland FL, USA, Dec. 11-15, 2016, A05.

(80) T. Onishi, K. Sekioka, M. Suto, K. Tanaka, S. Koyama, Y. Inaba, H. Takahashi, M. Harigai, K. Takeshita: Adsorption of Platinum-Group Metals and Molybdenum onto Aluminum Ferrocyanide in Spent Fuel Solution; *The Fifth International Symposium on Innovative Nuclear Energy systems (INES-5)*, Tokyo, Oct. 31- Nov. 2, 2016, B23-1.

(81) Michal Cibula, Yusuke Inaba, Kenji Takeshita, Hirokazu Narita: Recovery of Platinum Group Metals from Nitric Acid using Thiodiglycolamides and Tertiary Amines; *The Fifth International Symposium on Innovative Nuclear Energy systems (INES-5)*, Tokyo, Oct. 31- Nov. 2, 2016, B22-3.

(82) Xiangbiao Yin, Hideharu Takahashi, Yusuke Inaba, Kenji Takeshita: Desorption of Cesium Ions from Vermiculite with Sea Water by Hydrothermal Process; *The Fifth International Symposium on Innovative Nuclear Energy systems (INES-5)*, Tokyo, Oct. 31- Nov. 2, 2016, B21-1.

(83) Kenji Takeshita, Yusuke Inaba, Hideharu Takahashi, Jun Onoe, Hirokazu Narita: Development of Simultaneous Adsorption Process of PGMs and Mo from High-level Liquid Waste; *Asian Nuclear Prospects International Conference 2016 (ANUP2016)*, Miyagi. Oct. 24-26, 2016.

(84) Kenji Takeshita, Michal Cibula, Hirokazu Narita, Hideharu Takahashi, Yusuke Inaba: Mutual Separation System of PGMs and Mo recovered from HLLW by Aluminum Ferrocyanide; *Nineteenth Symposium on Separation Science and Technology for Energy Application*, Tennessee, USA, Oct. 10-12, 2016.

(85) Kenji Takeshita, Yusuke Inaba, Hideharu Takahashi, Jun Onoe, Hirokazu Narita: Establishment of Vitrification System with Simultaneous Adsorption Process of PGMs and Mo from High-Level Liquid Waste; *BIT's 6th Annual New Energy Forum (NEF-Qingdao 2016)*, Qingdao, China, Nov. 10-12, 2016.

(86) Kenji Takeshita: 6-Applied and Nuclear Physics; *3rd Tokyo Tech - Uppsala University Joint Symposium'Breakthroughs in Science & Technology for the 21st century'*, Sweden, Sep.12-13, 2016.

(87) Kenji Takeshita: Removal Process of Radioactive Cesium from Soil contaminated by Fukushima Daiichi Nuclear Accident; *Atalante2016*, Montpellier, France, June 5-10, 2016, ATAL2016-169.

(88) Travis S. Grimes, Masahiko Nakase, Nicholas C. Schmitt, Bruce J. Mincher: Further Studies on the Behavior of Higher Valence Americium in Acidic Solution; *40th Annual Actinide Separations Conference*, San Diego, USA, May 24-26, 2016.

(89) Yusuke Inaba, Hideharu Takahashi, Miki Harigai, Yalou Zou, Sho Hirohama, Keita Saito, Ria Mishima, Kenji Takeshita: Development of Recovery Process of Platinum-group Metals from HLLW for Stable Production and Volume Reduction of Homogeneous Vitrified Object (17) Platinum-group Metals and Mo adsorption characteristics to Aluminum-ferrocyanide and Metal ion Recovery from Combustion treated ferrocyanide; *2017 Annual meeting of Atomic Energy Society of Japan*, March 27-29, 2017, 2L11.

(90) Ippei Amamoto, Hidekazu Kobayashi, Yasuo Ayame, Yusuke Inaba, Kazuo Utsumi, Kenji Takeshita, Jun Onoe, Yui Kaneda, Akiko Koshizaka, Yoshio Hasegawa: Development of Recovery Process of Platinum-group Metals from HLLW for Stable Production and Volume Reduction of Homogeneous Vitrified Object (18) Synthesis of ceramics support materials to impregnate with ferrocyanide and their sorption characteristics; *2017 Annual meeting of Atomic Energy Society of Japan*, March 27-29, 2017, 2L12.

(91) Toshikazu Sato, Yuuki Sawada, Shinta Watanabe, Masato Nakaya, Masato Yoshino, Yusuke Inaba, Hideharu Takahashi, Kenji Takeshita, Tomoko Yoshida, Jun Onoe: Development of Recovery Process of Platinum-group Metals from HLLW for Stable Production and Volume Reduction of Homogeneous Vitrified Object (19) Chemical Form of Ruthenium ion in Nitric acid aqueous solution calculated by by utilizing UV-Vis/XAFS spectroscopy and first principle calculation; *2017 Annual meeting of Atomic Energy Society of Japan*, March 27-29, 2017, 2L13.

(92) Shinta Watanabe, Yuuki Sawada, Masato Nakaya, Masato Yoshino, Takanori Nagasaki, Hideharu Takahashi, Yusuke Inaba, Kenji Takeshita, Jun Onoe: Development of Recovery Process of Platinum-group Metals from HLLW for Stable Production and Volume Reduction of Homogeneous Vitrified Object (20) Analysis of PGMs and Mo adsorption characteristics to ferrocyanide utilizing first-principle calculation and spectroscopic experiments; *2017 Annual meeting of Atomic Energy Society of Japan*, March 27-29, 2017, 2L14.

(93) Yoshio Nakano, Makoto Nishikawa, Kota Kawai, Kenji Takeshita: Development of Recovery Process of Platinum-group Metals from HLLW for Stable Production and Volume Reduction of Homogeneous Vitrified Object (21) Analysis for Solubility and Diffusion Behavior of Main Componential Elements in Simulated HLLW into borosilicate glass phase; *2017 Annual meeting of Atomic Energy Society of Japan*, March 27-29, 2017, 2L15.

(94) Michal Cibula, Yusuke Inaba, Kenji Takeshita, Hirokazu Narita: Development of Recovery Process of Platinum-group Metals from HLLW for Stable Production and Volume Reduction of Homogeneous Vitrified Object (22) Extraction of Platinum Group Metals from Nitric Acid Solutions Using Thiodiglycolamides and Tertiary Amines" *2017 Annual meeting of Atomic Energy Society of Japan*, March 27-29, 2017, 2L16.

(95) Kenji Takeshita, Yoshio Nakano, Yusuke Inaba, Hideharu Takeshita, Miki Harigai, Jun Onoe, Shinta Watanabe, Yasuo Ayame, Ippei Amamoto, Takashi Onishi: Development of Recovery Process of Platinum-group Metals from HLLW for Stable Production and Volume Reduction of Homogeneous Vitrified Object (23) System Assessment; *2017 Annual meeting of Atomic Energy Society of Japan*, March 27-29, 2017, 2L17.

(96) Hao Wu, Yusuke Inaba, Kenji Takeshita: Selective Extraction of Soft Metal Ions in Nitric Acid Solution by a New Ionic Liquid including TPEN Structure; *2017 Annual meeting of Atomic Energy Society of Japan*, March 27-29, 2017, 3L10.

(97) Kenji Takeshita: The Strategic Nuclear Education Program by Japanese University Network for Global Nuclear Human Resource Development; *2017 Annual meeting of Atomic Energy Society of Japan*, March 27-29, 2017, 2F-PL01.

(98) Shun Kanagawa, Ryuji Sannnomiya, Kenji Takeshita: Tritium Recovery from Contaminated Water Generated by Fukushima Dai-ichi NPP Accident utilizing Trickle-bed Type H_2-H_2O isotope Exchange Process; *15th Workshop of isotope science*, Tokyo, March 10, 2017, S7.

(99) Kenji Takeshita, Shunsuke Kozono, Yusuke Inaba: Recovery of Tritium from Contaminated Water generated by Fukushima Dai-ich NPP Accident; *15th Workshop of isotope science*, Tokyo, March 10, 2017, Op7.

(100) Shun Kanagawa, Kenji Takeshita: Applicability of Trickle-bed Type H_2-H_2O Isotope Exchange Process for Tritium Recovery from Contaminated Water Generated by Fukushima Dai-ichi NPP Accident.; *NDEC-2*, Tokyo, March 7, 2017.

(101) Junpei Imoto, Genki Furuki, Asumi Ochiai, Shinya Yamasaki, Kenji Nanba, Toshihiko Ohnuki, Bernd Granbow, Rodney C. Ewing, Satoshi Utsunomiya, Cesium-rich micro-particles unveil the explosive events in the Fukushima Daiichi Nuclear Power Plant, *Goldschmidt Conference 2016*, Yokohama, Japan, June 26-Julay 1, 2016.

(102) Shinya Yamasaki, Naofumi Kozai, Kazuya

Tanaka, Toshihiko Ohnuki, Effect of Redoxactive Organic Compounds on Extraceller Uranium (VI) Reduction by Using Electrochemical Methods, *Goldschmidt Conference 2016*, Yokohama, Japan, June 26-Julay 1, 2016. (Invited)

(103) Tomoaki Kato, Toshihiko Ohnuki, Qianqian Yu, Sorption of Sr^{2+} into Mn Oxides Produced by MnO_4^- Reduction Using Biomass, *Goldschmidt Conference 2016*, Yokohama, Japan, June 26-Julay 1, 2016.

(104) Naofumi Kozai, Fuminori Sakamoto, Kazuya Tanaka, Toshihiko Ohnuki, T. Satoh, Tomihiro Kamiya, Pseudocolloid Formation of Uranium with Soluble Surface Glycoprotein of Paramecium, *Goldschmidt Conference 2016*, Yokohama, Japan, June 26-Julay 1, 2016.

(105) Kazuya Tanaka, Yukinori Tani, Toshihiko Ohnuki, Specific Sorption Processes of REEs and Actinides Induced by Biomolecules, *Goldschmidt Conference 2016*, Yokohama, Japan, June 26-Julay 1, 2016. (Invited)

(106) Toshihiko Ohnuki, Naofumi Kozai, Fuminori Sakamoto, Takumi Saito, Mitsuo Yamashita, Takumi Horiike, Satoshi Utsunomiya, Removal of Radioactive Strontium from Sea Water by Biogenic Calcium Carbonates, *Goldschmidt Conference 2016*, Yokohama, Japan, June 26-Julay 1, 2016. (Invited)

(107) Junpei Imoto, Genki Furuki, Asumi Ochiai, Shinya Yamasaki, Kenji Nanba, Toshihiko Ohnuki, Bernd Grambow, Rodney C. Ewing, Satoshi Utsunomiya, Unraveling the formation processes of Cs-rich microparticles in the Fukushima Daiichi Nuclear Power Plant, AESJ 2016 Fall meeting, Kurume, Japan, Sept. 7-9, 2016.

(108) Toshihiko Ohnuki, Tetsuya Ito, Takasuke Kakuta, Biological degradtion of oil in the contaminated waste water, AESJ 2016 Fall meeting, Kurume, Japan, Sept. 7-9, 2016.

(109) Genki Furuki, Junpei Imoto, Asumi Ochiai, Shinya Yamasaki, Kenji Nanba, Toshihiko Ohonuki, Bernd Grambow, Rodney C. Ewing, Satoshi Utsunomiya, Migration in environment and atomic scale properties of the particle containing high concentration of radioactive cesium present in Fukushima, AESJ 2016 Fall meeting, Kurume, Japan, Sept. 7-9, 2016.

(110) Satoshi Utsunomiya, Shota Masaki, Yuriko Nakano, Kenta Ichiyoshi, Toshihiko Ohnuki, Michael F. Hochella, Jr., Molecular Science for the role of microorgansims goveming migration of radionuclides (1) Interaction between microorganisms and environmental nanoparticles in subsurface, AESJ 2016 Fall meeting, Kurume, Japan, Sept. 7-9, 2016.

(111) Toshihiko Ohnuki, Transformation of radionuclides occurred at micron meter area to govern long-term migration in groundwater, 2016 The Geochemical Society of Japan Meeting, Osaka, Japan, Sept. 14-16, (2016).

(112) T. Horiike, Y. Dotsuta, M. Yamashita, Y. Nakano, S. Utsunomiya, N. Kozai, T. Ohnuki, Bioremediation of radioactive strontium contaminated sea water by biomineralization, 2016 The Geochemical Society of Japan Meeting, Osaka, Japan, Sept. 14-16, (2016).

(113) S. Utsunomiya, S. Masaki, Y. Nakano, K. Ichiyoshi, T. Ohnuki, Michael F. Hochella Jr., Molecular Science for the role of microorgansims on migration of radionuclides: Interaction between microorganisms and environmental nanoparticles in subsurface, 2016 The Geochemical Society of Japan Meeting, Osaka, Japan, Sept. 14-16, (2016).

(114) Junpei Imoto, Genki Furuki, Asumi Ochiai, Shinya Yamasaki, Kenji Nanba, Toshihiko Ohonuki, Bernd Grambow, Rodney C. Ewing, Satoshi Utsunomiya, Formation processes of radioactive Cs-rich micro-particles during melt-downs in the Fukushima Daiichi Nuclear Power Plant unraveled by atomic-resolution electron microscopy, 2016 The Geochemical Society of Japan Meeting, Osaka, Japan, Sept. 14-16, (2016).

(115) G. Furuki, J. Imoto, A. Ochiai, S. Yamasaki, K. Nanba, T. Ohnuki, B. Grambow, R. C. Ewing, S. Utsunomiya, Migration in environment and atomic scale properties of the particle containing high concentration of radioactive cesium present in Fukushima, 2016 The Geochemical Society of Japan Meeting, Osaka, Japan, Sept. 14-16, (2016).

(116) F. Sakamotoi, N. Kozai, K. Tanaka, T. Ohnuki, Study on accumulation of 137Cs in mushrooms released by Fukushima Daiichi Nuclear disaster and rediffusion of it to the environment, 2016 The Geochemical Society of Japan Meeting, Osaka, Japan, Sept. 14-16, (2016).

(117) , 2016 The Geochemical Society of Japan Meeting, Osaka, Japan, Sept. 14-16, (2016).

(118) Toru Tsunoura, Yosuke Okubo, Katsumi Yoshida, Toyohiko Yano, Takuya Aoki, Toshio Ogasawara: Wet Oxidation Behavior of Silicide and SiC-Fiber-Reinforced Composites Fabricated by Melt Infiltration Using Si-Hf and Si-Ti Alloy; 40th International Conference on Advanced Ceramics and Composites, Daytona Beach, Florida, USA, January 26, 2016, ICACC-GYIF-022-2016.

(119) Katsumi Yoshida, Naoki Mizuta, Toyohiko Yano, Masaki Kotani, Takuya Aoki, Toshio Ogasawara: Formation of Boron Nitride Interphase on SiC Fibers for SiC_f/SiC Composites by Electrophoretic Deposition Method and Their Mechanical Properties;" 40th International Conference on Advanced Ceramics and Composites, Daytona Beach, Florida, USA, January 28, 2016, ICACC-S1-053-2016.

(120) Toru Tsunoura, Yosuke Okubo, Katsumi Yoshida, Toyohiko Yano, Takuya Aoki, Toshio Ogasawara: Oxidation Behavior of SiC Fiber-Reinforced Composites Fabricated by Melt Infiltration Using Si-Hf and Si-Ti Alloys; 40th

International Conference on Advanced Ceramics and Composites, Daytona Beach, Florida, USA, January 29, 2016, ICACC-S1-070-2016.

(121) Katsumi Yoshida, Naoki Mizuta, Takashi Ajito, Toyohiko Yano, Masaki Kotani, Takuya Aoki, Toshio Ogasawara: Effect of Carbon and Boron Nitride Interphases Formed by Electrophoretic Deposition Process on Mechanical Properties of SiC_f/SiC Composites; International Symposium on the Science of Engineering Ceramics (EnCera 2016), Niigata, Japan, May 11, 2016.

(122) Toru Tsunoura, Katsumi Yoshida, Toyohiko Yano, Takuya Aoki, Toshio Ogasawara: High Temperature Wet Oxidation Behavior of SiC Fiber-Reinforced SiC-Based Composites Fabricated by Melt Infiltration Using Si Binary Alloys; 9th International Conference on High Temperature Ceramic Matrix Composites (HTCMC9), Global Forum on Advanced Materials and Technologies for Sustainable Development (GFMAT 2016), Toronto, Canada, June 28, 2016, H3-013-2016.

(123) Takuya Aoki, Toshio Ogasawara, Toru Tsunoura, Katsumi Yoshida, Toyohiko Yano: Processing of Tyranno ZMI Fiber/$TiSi_2$-Si Matrix Composites for High-Temperature Structural Application; 9th International Conference on High Temperature Ceramic Matrix Composites (HTCMC9), Global Forum on Advanced Materials and Technologies for Sustainable Development (GFMAT 2016), Toronto, Canada, June 28, 2016, H3-018-2016.

(124) Katsumi Yoshida, Tetsu Kikuhara, Naoki Mizuta, Takashi Ajito, Toyohiko Yano, Masaki Kotani, Takuya Aoki, Toshio Ogasawara: Application of Electrophoretic Deposition for Interphase Formation on Polycrystalline and Amorphous SiC Fibers in SiC_f/SiC Composites; 9th International Conference on High Temperature Ceramic Matrix Composites (HTCMC9), Global Forum on Advanced Materials and Technologies for Sustainable Development (GFMAT 2016), Toronto, Canada, June 28, 2016, H3-014-2016.

(125) Katsumi Yoshida, Toru Tsunoura, Toyohiko Yano: Sintering of YOF Ceramics and Their Properties; 9th International Conference on High Temperature Ceramic Matrix Composites (HTCMC9), Global Forum on Advanced Materials and Technologies for Sustainable Development (GFMAT 2016), Toronto, Canada, June 28, 2016, G8-011-2016.

(126) Katsumi Yoshida, Makoto Takahashi, Toyohiko Yano: Effects of Boron and Aluminum Additives on In-Situ Grain Growth of Porous SiC Ceramics; 9th International Conference on High Temperature Ceramic Matrix Composites (HTCMC9), Global Forum on Advanced Materials and Technologies for Sustainable Development (GFMAT 2016), Toronto, Canada, June 28, 2016, P022-2016.

(127) Toru Tsunoura, Katsumi Yoshida, Toyohiko Yano: Fabrication and Fluorine Plasma Irradiation Behavior of YOF Ceramics; The 38th International Symposium on Dry Process (DPS2016), Sapporo, Japan, November 22, 2016, P-18.

(128) Katsumi Yoshida, Tetsu Kikuhara, Toyohiko Yano, Masaki Kotani, Toshio Ogasawara: Carbon Interphase Formation on Low-Conductive Silicon Carbide Fibers by Electrophoretic Deposition Method; The 54th Symposium on Basic Science of Ceramics, Saga, Japan, January 8, 2016, 2B02.

(129) Yamato Sugitatsu, Toyohiko Yano, Katsumi Yoshida, Tadahiko Takada: Immobilization of Absorbed Elements in Porous Ceramics with Natural Minerals by Post-Firing; 9th Student Meeting of the Kanto-Koetsu Division of the Atomic Energy Society of Japan, Tokyo, March 11, 2016, A3.

(130) Makoto Takahashi, Katsumi Yoshida, Toyohiko Yano: Effects of Sintering Additives on Microstructure of Porous SiC Ceramics with In-Situ Grain Growth; Annual Meeting of The Ceramic Society of Japan, 2016, Tokyo, Japan, March 15, 2016, 2I20.

(131) Naoki Mizuta, Katsumi Yoshida, Toyohiko Yano, Masaki Kotani, Takuya Aoki, Toshio Ogasawara: Fabrication of SiC_f/SiC Composites with Boron Nitride Interphase Formed by EPD and Their Mechanical Properties; Annual Meeting of The Ceramic Society of Japan, 2016, Tokyo, Japan, March 16, 2016, 3I17.

(132) Toru Tsunoura, Katsumi Yoshida, Toyohiko Yano, Toshio Ogasawara, Takuya Aoki: High Temperature Wet Oxidation Behavior of SiC Fiber-Reinforced Composites Fabricated by Melt Infiltration Using Si-Ti Alloy; Annual Meeting of The Ceramic Society of Japan, 2016, Tokyo, Japan, March 16, 2016, 3I18.

(133) Toru Tsunoura, Katsumi Yoshida, Toyohiko Yano: Evaluation of Plasma Resistance of YOF Ceramics; The 63rd JSAP Spring Meeting, 2016, Tokyo, Japan, March 19, 2016, 19p-W621-8.

(134) Mohd Idzat Idris, Katsumi Yoshida, Toyohiko Yano: Radiation damage Analysis of High purity SiC by TEM; 2016 Annual Meeting of the Atomic Energy Society of Japan, Sendai, Japan, March 26, 2016, 1H13.

(135) Yamato Sugitatsu, Toyohiko Yano, Katsumi Yoshida, Tadahiko Takada: Cesium and Strontium Absorption Characteristics of Porous Ceramics for Absorbing Radioactive Nuclides using Natural Minerals; 2016 Annual Meeting of the Atomic Energy Society of Japan, Sendai, Japan, March 26, 2016, 1G18.

(136) Katsumi Yoshida: Development of Formation Process of Interphase in SiC_f/SiC Composites Based on Electrochemical Process; AIMS Workshop 2016, Sendai, Japan,. August 5, 2016.

(137) Toru Tsunoura, Katsumi Yoshida, Toyohiko Yano, Toshio Ogasawara, Takuya Aoki: Oxidation Behavior of Matrices of Composites Fabricated by Melt Infiltration using Si Binary Alloys; 29th Fall

Meeting of The Ceramic Society of Japan, Hiroshima, September 8, 2016, 2B07.

(138) Katsumi Yoshida, Hiroyuki Akimoto, Toyohiko Yano, Masaki Kotani, Takuya Aoki, Toshio Ogasawara: Effects of Fiber Orientation and Fiber Volume Fraction on Mechanical Properties of SiC_f/SiC Composites with Carbon Interphase Formed by EPD Process; 29th Fall Meeting of The Ceramic Society of Japan, Hiroshima, September 8, 2016, 2B25.

(139) Toru Tsunoura, Katsumi Yoshida, Toyohiko Yano: Oxidation Behavior of SiC Fiber-Reinforced Si-$TiSi_2$ Eutectic Matrix Composites and Monolithic $TiSi_2$ in Humid Air; M&P2016, Tokyo, November 26, 2016, 428.

(140) Shuichi Wakayama, Takenobu Sakai, Katsumi Yoshida: Characterization of Thermal Shock Fracture Behavior of Ceramics with Different Stress Ratio; M&P2016, Tokyo, November 26, 2016, 425.

(141) Jelena Maletaškić, Branko Matović, M. Prekajski Djordjević, Katsumi Yoshida, Toyohiko Yano : Phase Evolution, Sintering Behavior and Mechanical Properties of CaO-TiO_2-SiO_2 (Sphene) Based Ceramics; The Fifth International Symposium on Innovative Nuclear Energy Systems, Tokyo, October 31-November 2, 2016, B11-1.

(142) Katsumi Yoshida, Mohad Idzat Idris, Saishun Yamazaki, Toyohiko Yano : Recovery Behavior of SiC_f/SiC Composites By Post-Irradiation Annealing up to of 1673 K; The Fifth International Symposium on Innovative Nuclear Energy Systems, Tokyo, October 31-November 2, 2016, B11-2.

(143) Yan You, Toshihiko Inoue, M. Sekine, Katsumi Yoshida, Toyohiko Yano : Orientation of Helium Bubbles in Neutron Irradiated B_4C", Abst, The Fifth International Symposium on Innovative Nuclear Energy Systems, Tokyo, October 31-November 2, 2016, B12-1.

(144) Branko Matović, M. Prekajski Djordjević, Jelen Maletaškić, Katsumi Yoshida, Toyohiko Yano : Preparation and Properties of Hydroxyapatite Nanospheres for Immobilization of Sr Isotopes ; The Fifth International Symposium on Innovative Nuclear Energy Systems, Tokyo, October 31-November 2, 2016, B22-1.

(145) Thanataon Pornphatdetaudom, Saishun Yamazaki, Katsumi Yoshida, Toyohiko Yano : Effect of Neutron Irradiation on Macroscopic Length, Lattice Parameter, Microstructure and Recovery Behavior of Aluminum Nitride ; The Fifth International Symposium on Innovative Nuclear Energy Systems, Tokyo, October 31-November 2, 2016, P-30.

(146) Muhammed Fajar, Katsumi Yoshida, Toyohiko Yano, Tohru S. Suzuki : Effect of Alumina as Sintering Additives on Mechanical and Thermal Properties of Textured Boron Carbide Ceramics by Strong Magnetic Field ; The Fifth International Symposium on Innovative Nuclear Energy Systems, Tokyo, October 31-November 2, 2016, P-31.

(147) H. Wada, A.V. Gubarevich, O. Odawara: Phosphor nanoparticles prepared by laser ablation in liquid and their optical applications; *41st international Conference & Exposition on Advanced Ceramics &Composites*, Florida, US, January 25, 2017.

(148) A. Gubarevich, H. Wada, O. Odawara, Nanoparticles formation by combustion synthesis and related processes; *Nonisothermal Phenomena and Processes: from Thermal Explosion Theory to Structural Macrokinetics*, Chernogolovka, Russia, November 28, 2016.

(149) J. Habasaki, A. Gubarevich: Molecular Dynamics Simulations of Silica-Nanocolloid-Water-NaCl Systems - A Role of Solvent for Structure Formation of Gels; Annual World Congress of Advanced Materials-2016, Chongqing, China, June 6, 2016.

(150) K. Kobayashi, T. Matsuda, S. Enomoto, M. Eto, Y. Kebukawa, H. Mita, S. Yoshida, H. Fukuda, K. Kondo, Y. Oguri: Formation of Super-complex Amino Acid Precursors in Interstellar Ice Analogues by Particles Irradiation; *Japan Geoscience Union Meeting 2016*, May 22–26, 2016, Makuhari Messe, Chiba, Japan, BAO01-04.

(151) H. Abe, H. Fukuda, K. Kondo, Y. Oguri, H. Mita, K. Nanbu, T. Ouchi, Y. Muramatsu, Y. Kebukawa, K. Kobayashi: Laboratory Simulations of Titan Tholins Formed by Cosmic Rays; *Japan Geoscience Union Meeting 2016*, May 22–26, 2016, Makuhari Messe, Chiba, Japan, BAO01-P01.

(152) R. Aoki, J. Ise, H. Fukuda, K. Kondo, Y. Oguri, Y. Kebukawa, K. Kobayashi: Amino Acid Formation from Simulated Mildly-Reducing Primitive Atmospheres by Spark Discharges, UV Irradiation and Proton Irradiation; *Japan Geoscience Union Meeting 2016*, May 22–26, 2016, Makuhari Messe, Chiba, Japan, BAO01-P02.

(153) Y. Hu, H. Fukuda, Y. Oguri: Evaluation of the X-ray Distribution of a Syringe-Needle Type Proton-Induced X-ray Source by Geant4 Simulation; *European Conference on X-ray Spectrometry 2016*, June 19–24, 2016, Gothenburg, Sweden, Post 148.

(154) K. Kobayashi, H. Abe, R. Aoki, Y. Kebukawa, H. Shibata, S. Yoshida, H. Shibata, K. Kondo, Y. Oguri: Energetics of Amino Acid Formation in Slightly Reducing Atmospheres of Primitive Earth and Titan; *26th Goldschmidt Conference*, June 26–July 1, 2016, Pacifico Yokohama, Yokohama, Japan, #03h.

(155) Yoshihisa Matsumoto. Fukushima Daiichi Nuclear Power Plant Accident 2011 from the Aspect of Radiation Biology. *ISTC Project A-2089 Workshop*, Yerevan State University, 6 June 2016.

(156) Ali Reza Amiri Moghani, Rujira Wanotayan, Mukesh Kumar Sharma, Anie Day Asa De Castro, Mikio Shimada, Yoshihisa Matsumoto. DNA

damage-induced phosphorylation of XRCC4 and its role in DNA double-strand break repair. *The Fifth International Symposium on Innovative Nuclear Energy Systems*, Tokyo Institute of Technology (Tokyo), 31 October-2 November 2016, A24-7.

(157) Mukesh Kumar Sharma, Shoji Imamichi, Mikoto Fukuchi, Ali Reza Amiri Moghani, Rujira Wanotayan, Mikio Shimada, Yoshihisa Matsumoto. XRCC4: target of phosphorylation by DNA-PK in DNA double-strand break repair. *10th 3R International Symposium*, Hotel Ichibata (Matsue), 13-17 November 2016, P-120.

(158) Yoshihisa Matsumoto. DNA and protein repair to be explored by structural biology. *Hiroshima International Workshop on Circular Dichroism Spectroscopy 2017 – Application to Imaging Microscopy and Radiation Biology*, Hiroshima Synchrotron Radiation Center (Higashihiroshima, Hiroshima), 28 February 2017.

(159) Takahiro Iwai, Shunsuke Hosoda, Satoshi Kohno, Mari Aida, Ken Kakegawa, Tomoko Miyake, Hidekadzu Miyahara, Yoshihisa Matsumoto, Koichi Chiba, Akitoshi Okino. High-sensitive Elemental Analysis of Single Human Cell using Droplet Injection ICP-AES/MS. *European Winter Conference on Plasma Spectrochemistry 2017*, St. Anton Am Arlberg, 20 February 2017.

(160) Ali Reza Amiri Moghani, Rujira Wanotayan, Mukesh Kumar Sharma, Anie Day Asa De Castro, Mikio Shimada, Yoshihisa Matsumoto. DNA damage-induced phosphorylation of XRCC4 at multiple sites. *Japan Radiation Research Society 59th Annual Meeting*, JMS Aster Plaza (Hiroshima, 26-28 October 2016, O11-2.

(161) Masanori Tomita, Yoshihisa Matsumoto, Junya Kobayashi, Kensuke Ohtsuka, Yuki Fujimichi, Toshiyasu Iwasaki. Unsolved problems on the biological effects of low dose/ low dose rate radiation. *Japan Radiation Research Society 59th Annual Meeting*, JMS Aster Plaza (Hiroshima, 26-28 October 2016, S4-1.

(162) Yoshihisa Matsumoto. Toward the future research on the biological effects of low dose (rate) radiation. *Japan Radiation Research Society 59th Annual Meeting*, JMS Aster Plaza (Hiroshima, 26-28 October 2016, S4-7.

(163) Yoshihisa Matsumoto. Mechanisms of DNA double-strand break repair through non-homologous end joining and its possible application to cancer therapy. 19th Symposium of International Association for Sensitization of Cancer Treatment, Nara Prefecture Culture Hall (Nara), 3-4 February 2017.

(164) Mikio Shimada, Fumio Matsuzaki, Tomohiro Matsumoto, Kenshi Komatsu: Effect of centrosome amplification in ionizing radiation induced microcephaly; 59th annual meeting of the Japanese Radiation Research Society, Hiroshima, Oct. 2016.

(165) Ali Reza Amiri Moghani, Rujira Wanotayan, Sharma Mukesh Kumar, Anie Day De Castro ASA, Mikio Shimada, Yoshihisa Matsumoto: DNA damage induced phosphorylation of XRCC4 at multiple sites; 59th annual meeting of the Japanese Radiation Research Society, Hiroshima, Oct. 2016.

(166) Hisayo Tsuchiya, Mikio Shimada, Junya Kobayashi, Yoshihisa Matsumoto: The role of DNA double strand breaks repair proteins in low dose rate ionizing radiation response; 59th annual meeting of the Japanese Radiation Research Society, Hiroshima, Oct. 2016.

(167) Motoki Yamaguchi, Yoshihisa Matsumoto, Mikio Shimada: Analyze of DNA damage response in combination treatment of ionizing radiation and hyperthermia; 59th annual meeting of the Japanese Radiation Research Society, Hiroshima, Oct. 2016.

(168) Asa Anie Day, Yoshihisa Matsumoto, Mikio Shimada. DNA double strand break repair function of XRCC4 mutants associated with microcephaly and growth defect, 59th annual meeting of the Japanese Radiation Research Society, Hiroshima, Oct. 2016.

(169) Masanori Matsumiya, Yoshihisa Matsumoto, Mikio Shimada: Generation of DNA double strand breaks repair gene knock out cells using genome editing; 59th annual meeting of the Japanese Radiation Research Society, Hiroshima, Oct. 2016.

(170) Mikio Shimada, Peter J McKinnon: DNA repair machinery in neural development; 59th annual meeting of the Japanese Radiation Research Society, Hiroshima, Oct. 2016.

(171) Mikio Shimada, Yoshihisa Matsumoto: the role of DNA repair factor PNKP in genome maintenance; 89th annual meeting of the Japanese Biochemical Society, Sendai. Japan, Sep. 2016.

(172) Mikio Shimada, Fumio Matsuzaki, Tomohiro Matsumoto, Kenshi Komatsu: Cell death and centrosome amplification dependent mitotic catastrophe in ionizing radiation induced microcephaly; Young biological imaging conference, Tokyo, Dec. 2016.

(173) Mikio Shimada: Potential investigation of micro device for cancer therapy: Fusion science project, Tokyo, Japan, Dec. 2016.

(174) Atsunori Terashima, Mikael Nilsson, Masaki Ozawa, Satoshi Chiba: Basic Research on the Element Transmutation of All the Fission Products Using Nuclear Reactors, (4) Verification of Nuclear Data on Neutron Capture Cross Section of Stable Isotopes of Ruthenium by Neutron Activation Analysis and Burnup Calculation; *2016 Fall Meeting of the Atomic Energy Society of Japan*, Fukuoka, September 7-9, 2016, 1N05.

(175) Chikako Ishizuka, Hiroki Joujima, Mark Usang, Satoshi Chiba, Nicolae Carjan: Charge polarization and its influence on prompt neutrons; *2016 Fall Meeting of the Atomic Energy Society of Japan*, Fukuoka, September 7-9, 20161N10.

(176) Yoritaka Iwata, Satoshi Chiba: Dynamic calculation of 236U fission using TDDFT; *2016 Fall Meeting of the Atomic Energy Society of Japan*,

Fukuoka, September 7-9, 2016, 2PL05.

(177) Tadashi Yoshida, Takahiro Tachibana, Satoshi Chiba: Analysis of Reactor-neutrino Spectra Fully based on Gross Theory of Beta-decay Emphasizing the Special Role of Odd-Odd FP Nuclides; *International Conference on Nuclear Data for Science and Technology (ND2016)*, September 11-16, 2016, Bruges, Belgium.

(178) M. Usang, F. Ivanyuk, C. Ishizuka, and S. Chiba, Effects of microscopic transport coefficients on fission observables calculated by Langevin equation and its systematics; *International Conference on Nuclear Data for Science and Technology (ND2016)*, September 11-16, 2016, Bruges, Belgium.

(179) Atsunori Terashima, Mikael Nilsson, Masaki Ozawa, Satoshi Chiba: Reliability Assessment of MVP-BURN Code and JENDL-4.0 Library Related to the Nuclear Transmutation of Light Platinum-Group Elements; *ND 2016 International Conference on Nuclear Data for Science and Technology*, Bruges, Belgium, September 11-16, 2016, R320.

(180) Atsunori Terashima, Toshitaka Kaneshiki, Masao Nomura, Masaki Ozawa: Separation and Recovery of Palladium from Nitric Acid Solution by Silica Based Benzo-15-crown-5 Ether Resin; *The Fifth International Symposium on Innovative Nuclear Energy Systems (INES-5)*, Tokyo, Japan, October 31 - November 2, 2016, B234.

(181) M. D. Usang, C. Ishizuka, F. Ivanyuk, and S. Chiba, Systematic Analysis of Fission Fragment Mass Distribution and TKE for Actinides by Langevin Equation; *The Fifth International Symposium on Innovative Nuclear Energy Systems (INES-5)*, Tokyo, Japan, October 31 - November 2, 2016, A32-2.

(182) C. Ishizuka, S. Chiba, N. Carjan: The Charge Polarization and Its Impact on Prompt Fission Neutron Spectra of Actinides; *The Fifth International Symposium on Innovative Nuclear Energy Systems (INES-5)*, Tokyo, Japan, October 31 - November 2, 2016, A32-1.

(183) R. Kimura, H. Sagara, S. Chiba: Applicability Study of the Photofission Based on Nuclear Material Isotopic Composition Measurement Method on the Thorium Uranium System; *The Fifth International Symposium on Innovative Nuclear Energy Systems (INES-5)*, Tokyo, Japan, October 31 - November 2, 2016, B14-2.

(184) Atsunori Terashima, Mikael Nilsson, Masaki Ozawa, Satoshi Chiba: Verification Methods of Thermal Neutron Capture Cross Sections by Combination of Neutron Activation Analysis and Burnup Calculation; *The Fifth International Education Forum on Environment and Energy Science*, San Diego, California, USA, December 15-19, 2016, D112.

(185) Shin Okumura, Toshihiko Kawano, Satoshi Chiba: Studies on Calculations of Prompt Neutron Multiplicities Fission Product Yields and Isomeric Yields by Hauser-Feshbach Statistical Decay Theory; *2017 Symposium on Nuclear Data*, Tokai, November 16-17, 2017, B9.

(186) T.Nishikawa Y.Iwata S.Chiba:Nucleus-Nucleus potential derived from microscopic theory; *Diversity of nuclear structure and the dynamics of it in terms of clustering and mean field*, Osaka, January,2017.

(187) Atsunori Terashima, Satoshi Chiba: Basic Research on the Element Transmutation of All the Fission Products Using Nuclear Reactors, (5) Effects of Changing Data of Thermal Neutron Capture Cross Section of ^{102}Ru on Production Amounts and Transmutation Characteristics of FP; *2017 Annual Meeting of the Atomic Energy Society of Japan*, Kanagawa, March 27-29, 2017, 2F13.

(188) Atsuhiko Etori, Akira Ono, Chikako Ishizuka, Satoshi Chiba: Study of fission and nuclear collisions by Antisymmetrized Molecular Dynamics; *2017 Annual Meeting of Atomic Energy Society of Japan*, Kanagawa, March 27-29, 2017, 2E20.

(189) Tadashi Yoshida, Takahiro Tachibana, Satoshi Chiba: Systematic Systematic Study on Fisson Yields, fission product nuclear data and fission mechnisms (11) Analysis of Antineutrino Energy Spectra from Aggregate FP Decay Based on the Gross Theory; *2017 Annual Meeting of Atomic Energy Society of Japan*, Kanagawa, March 27-29, 2017, 2E22.

(190) Shin Okumura, Mark Dennis Usang, Toshihiko Kawano, Satoshi Chiba: Calculations of prompt neutron multiplicities and isomer production ratios by the statistical model; *2017 Annual Meeting of Atomic Energy Society of Japan*, Kanagawa, March 27-29, 2017, 2M08.

(191) Chikako Ishizuka, Satoshi Chiba, Fedir Ivanyuk, Joachim Maruhn: Systematic Study on Fisson Yields, fission product nuclear data and fission mechnisms (7) n-induced ^{235}U fission based on four-dimensional Langevin model; *2017 Annual Meeting of Atomic Energy Society of Japan*, Kanagawa, March 27-29, 2017, 2E18.

(192) Kohsuke Tsubakihara, Shin Okumura, Tadashi Yoshida, Satoshi Chiba: Systematic study on fission yields, fission product nuclear data and fission mechanisms, (2) Development of the retrieval system of fission yields from EXFOR database; *2017 Annual Meeting of Atomic Energy Society of Japan*, Kanagawa, March 27-29, 2017, 2E13.

(193) Takashi Nishikawa, Yoritaka Iwata, Satoshi Chiba: The study of nucleus-nucleus potential and friction coefficient from TDHF; *2017 Annual Meeting of Atomic Energy Society of Japan*, Kanagawa, March 27-29, 2017, 2E19.

(194) Riku Nakamura Kenichi Tanaka Satoshi Chiba: Study on concrete permeation calculation using PHITS code for decommissioning; *2017 Annual Meeting of Atomic Energy Society of Japan*, Kanagawa, March 27-29, 2017, 2H10.

(195) Kohsuke Tsubakihara, Akira Ohnishi, Toru

Harada: Dense matter EOS with RMF model including multi-body couplings; *2017 Annual Meeting of Japan Physics Society*, Osaka, March 17-20, 2017, 20aK22-6.

(196) Shin Okumura, Kean Kun Ratha, Kousuke Tsubakihara Toshihiko Kawano, Satoshi Chiba: Systematic study on fission yields, fission product nuclear data and fission mechanisms (3) Comparison of experimental and theoretical fission product yield; *2017 Annual Meeting of Atomic Energy Society of Japan*, Kanagawa, March 27-29, 2017, 2E14.

(197) Riku Nakamura, Kenichi Tanaka, Satoshi Chiba: Study on concrete permeation calculation using PHITS code for decommissioning; Conference for R&D Initiative on Nuclear Decommissioning Technology by the Next Generation-2,Tokyo,March,2017.

(198) Jun Takeda, Atsushi Nezu, Hiroshi Akatsuka: Experimental Study on Plasma Flow along E_rB_z Configuration with Magnetized Electron and Non-Magnetized Ion; *Technical Meeting on Plasma Science and Technology, IEE Japan*, Osaka, August 8 – 9, 2016, PST-16-074.

(199) Hiroshi Akatsuka: Issues of Optical Emission Spectroscopic Measurement of Atmospheric-Pressure Plasmas; *The 77th JSAP Autumn Meeting*, Niigata, September 13 – 16, 2016, 14p-A22-2.

(200) Keisuke Tajima, Atsushi Nezu, Hiroshi Akatsuka: Steady-State Plasma Flow Injected into Curved Magnetic Field; *The 33th Annual Meeting of Japan Society of Plasma Science and Nuclear Fusion Research*, Sendai, November 29 – December 2, 2016, 30aP04.

(201) Masao Kinoshita, Takayuki Fuyuto, Hiroshi Akatsuka: Measurement of Vibrational and Rotational Temperature in Spark Discharge Plasma by Optical Emission Spectroscopy (Effects of Air Flow Rate and Atmospheric Pressure); *The 27th Internal Combustion Engine Symposium*, Tokyo, December 5 – 7, 2016, 44.

(202) Hiroshi Akatsuka: Optical Emission Spectroscopy Measurement of Atmospheric-Pressure Non-Equilibrium Argon Plasmas — Measurement of Electron Temperature and Density; *2018 Seminar of Atomic and Molecular Data Forum*, Toki, December 20 – 22, 2016, Session 2–3.

(203) Hiroshi Akatsuka, Toshifumi Yuji, Reda A. A. El-Koramy: OES Measurements of Electron Temperature of Atmospheric-Pressure Microwave Discharge Argon Plasma — CR Model-Assisted Line-Intensity Measurement and Continuum Measurement; *34th Symposium on Plasma Processing/ 29th Symposium on Plasma Science for Materials*, Sapporo, January 16 – 18, 2017, P2-2.

(204) Yuya Matsuoka, Daisuke Hirotani, Ryujirou Suzuki, Atsushi Nezu, Shinsuke Mori, Hiroshi Akatsuka: Evaluation of Various Properties of Argon Arc Discharge Plasma Generated in Water; *2nd Conference for R&D Initiative on Nuclear Decommissioning Technology by the Next generation (NDEC2)*, Tokyo, March 7, 2016, P(a)-07.

(205) Yasuka Onishi, Atsushi Nezu, R. A. A. El-Koramy, Hiroshi Akatsuka: Plasma Spectroscopy Study of H_2 - He Mixture Microwave Discharge; *2017 National Convention IEE Japan*, Toyama, March 15 – 17, 2017, 1-080.

(206) Daisuke Hirotani, Yuya Matsuoka, Ryujirou Suzuki, Atsushi Nezu, Shinsuke Mori, Reda A. A. El-Koramy, Hiroshi Akatsuka: Characteristics Arc-Discharge Plasma with their Electrodes Immersed in Water; *2017 National Convention IEE Japan*, Toyama, March 15 – 17, 2017, 1-083.

(207) Senna Fukukawa, Atsushi Nezu, Reda A. A. El-Koramy, Hiroshi Akatsuka: Experimental Study on Nitrogen Excited States by N_2 Puff onto Argon Arc-Jet Plasma; *2017 National Convention IEE Japan*, Toyama, March 15 – 17, 2017, 1-164.

(208) H. Akatsuka: Basic Experiments in an Expanding Arc-Jet and its Hybrid Simulation; *2017 Annual (72nd) Meeting of the Physical Society of Japan*, Osaka, March 17 – 20, 2017, 18pC34-4.

(209) Jiang LIU, Yuya Morita, Kentaro Urata, Takehiro Sumita, Yoshinao Kobayashi. Dissolution behavior of SUS304 stainless steel into Fe-Cr-Ni-B-C alloy, 5th International Symposium on Innovative Nuclear Energy Systems, INES-5, Oct. 2016.

(210) Liu Jiazhan, Kobayashi Yoshinao. Sulfide capacity of CaO-CaCl2-CaF2 slags saturated with CaO, 10th International Conference on Molten Slags, Fluxes and Salts, Proceedings of The 10th International Conference on Molten Slags, Fluxes and Salts (MOLTEN16), May. 2016.

(211) Kentaro Urata, Yoshinao Kobayashi. FORMATION OF COPPER SULFIDE PRECIPITATE IN SOLID IRON, The 10th International Conference on Molten Slags, Fluxes and Salts, Proceedings of The 10th International Conference on Molten Slags, Fluxes and Salts (MOLTEN16), TMS (The Minerals, Metals & Materials Society), p. 1229-1236, May. 2016.

(212) Peryoga Yoga, Hiroshi Sagara, Tomooki Shiba. PHITS Benchmarking for HPGe Detector Efficiency, The 5th International Symposium on Innovative Nuclear Energy Systems, Oct. 2016.

(213) Masatoshi Kawashima, Hiroshi Sagara. Consideration of Enhanced Safety Based on CMR-concept for Large Fast Reactor", The 5th International Symposium on Innovative Nuclear Energy Systems, Oct. 2016.

(214) T. Shiba, H. Tomikawa, H. Sagara, A. Ishimi. Simple Method to Create Gamma Ray Source Spectrum for Passive Gamma Technique, The 5th International Symposium on Innovative Nuclear Energy Systems, Oct. 2016.

(215) T. Nagatani, M. Komeda, T. Shiba, M. Maeda, Y. Nauchi, M. Kureta, H. Tomikawa, K. Okumura, H. Sagara, C. Heinberg, K. Hori. Characterization Study

of Four Candidate Technologies for Nuclear Material Quantification in Fuel Debris at Fukushima Daiichi Nuclear Power Station, The 5th International Symposium on Innovative Nuclear Energy Systems, Oct. 2016.

(216) Rei Kimura, Hiroshi Sagara, Satoshi Chiba. Applicability Study of the Photofission Based Nuclear Material Isotopic Composition Measurement Method on the Thorium Uranium System, The 5th International Symposium on Innovative Nuclear Energy Systems, Oct. 2016.

(217) Tomooki SHIBA, Hirofumi TOMIKAWA, Hiroshi SAGARA, Akihiro ISHIMI. Applicability Evaluation of Candidate Technologies for Nuclear Material Quantification in Fuel Debris at Fukushima Daiichi Nuclear Power Station - Passive Gamma Technique -, INMM Ann. Mtg, Jul. 2016.

(218) Hiroshi SAGARA. Characterization Study of Four Candidate Technologies for Nuclear Material Quantification in Fuel Debris at Fukushima Daiichi Nuclear Power Station (Interim Report), INMM Ann. Mtg., Jul. 2016.

(219) Takeshi Aoki, Hiroshi Sagara, Chi Young Han. Feasibility study on TRISO fuel particles for efficient Pu incineration and 3S features enhancement in HTGR, INMM Ann. Mtg., Jul. 2016.

(220) Hiroshi SAGARA. Nuclear Non-proliferation Nuclear Security, Nuclear Engineering Intensive Course in cooperation with Kaunas University of Technology 6th Term, Mar. 2016.

(221) Hiroshi SAGARA. Nuclear Non-proliferation Safeguards, Nuclear Engineering Intensive Course in cooperation with Kaunas University of Technology 6th Term, Mar. 2016.

(222) Pribadi adhi, Nariaki Okubo, Atushi Komatsu, Masatoshi Kondo, Minoru Takahashi. Electrochemical impedance analysis on solid electrolyte oxygen sensor with gas and liquid reference electrodes for liquid LBE, The Fifth International Symposium on Innovative Nuclear Energy Systems INES-5, Book of Abstracts, The Fifth International Symposium on Innovative Nuclear Energy Systems INES-5, INES-5 Administration Office, c/o Lane, Oct. 2016.

(223) Masatoshi KONDO, Nariaki Okubo, Eriko Irisawa, Atushi Komatsu, Norito Ishikawa, Teruya Tanaka. Oxidation characteristics of lead alloys in air ingress accident, The Fifth International Symposium on Innovative Nuclear Energy Systems INES-5, Book of Abstract, The Fifth International Symposium on Innovative Nuclear Energy Systems INES-5, INES-5 Administration Office, c/o Lane, Oct. 2016.

(224) Masatoshi Kondo, Masaomi Ishi, Yoshimitsu Hishimuma, Teruya Tanaka, Takashi Nozawa, Takeo Muroga. [Invited presentation] Metallurgical study on corrosion of RAFM steel in Pb-Li alloys at various Li concentrations, 13th China-Japan Symposium on Materials for Advanced Energy Systems and Fission & Fusion Engineering, Book of Abstract, Sep. 2016.

(225) Masatoshi KONDO, Masaomi ISHI, Takayoshi Norimatsu, Takeo MUROGA. [Keynote speech] Experimental study on corrosion and mass transfer in flowing Pb-17Li with temperature gradient for development of liquid breeder type fusion blanket system, International Conference on Energy Sciences (ICES 2016), Book of Abstract, Institute Teknologi Bandung, p. 3-4, Jul. 2016.

(226) Min Seok Kim, Takehiko Tsukahara, Selective Extraction of Strontium Ions by Using Diaza-crown Ether-Based Extractant in Supercritical Carbon Dioxide, The 12th Reprocessing and Recycling Division Seminar, 2016/12/26.

(227) Sonomi KAWANAMI, Takehiko TSUKAHARA, Creation of Organic/Inorganic Hybrid Nanostructures For Uranium Ion Sensing, The 7th Vietnam-Japan Research/HRD Forum on Nuclear Technology, 2016/11/24-25,

(228) Yuta FUKATSU, Luc R. VAN LOON, Amir SHAFIZADEH, Daniel GROLIMUND, Yasuhisa IKEDA, Takehiko TSUKAHARA, Effect of celestite precipitation in compacted illite on the diffusion of HTO, 36Cl- and 22Na+, The 5th International Symposium on Innovative Nuclear Energy Systems(INES-5), 2016/10/31-11/2.

(229) Nutthon Yokachuksuse, Takehiko Tsukahara, Studies on Separation of Lanthanides using Thermoresponsive Polymer Brushes, The 5th International Symposium on Innovative Nuclear Energy Systems(INES-5), 2016/10/31-11/2.

(230) Rongwei SUN, Takehiko Tsukahara, Effects of Cations on Water Motions in Bentonite Clays using NMR Relaxation Measurements, The 5th International Symposium on Innovative Nuclear Energy Systems(INES-5), 2016/10/31-11/2.

(231) Sonomi KAWANAMI, Takehiko TSUKAHARA, Development of Uranium Ion Sensor Using Surface Plasmon Resonance of Polymer-Immobilized Gold Nanostructures, The 5th International Symposium on Innovative Nuclear Energy Systems(INES-5), 2016/10/31-11/2.

(232) Min seok Kim, Takehiko TSUKAHARA, Selective Extraction of Strontium Ions by Using Diaza-crown Ether-Based Extractant in Supercritical Carbon Dioxide, The 5th International Symposium on Innovative Nuclear Energy Systems(INES-5), 2016/10/31-11/2.

(233) Aileen Brandt, Takehiko Tsukahara, Development of Microfluidic-Based Selenium Ion Separation and Detection System, The 5th International Symposium on Innovative Nuclear Energy Systems (INES-5), 2016/10/31-11/2.

(234) Kazuki Matsushita, Kyojiro Morikawa, Naoki Sasaki, Takehiko Tsukahara, Fabrication of Deep Quartz Microchannels by Dry-Ething for Radioactive Waste Analysis, The 5th International Symposium on Innovative Nuclear Energy Systems(INES-5),

2016/10/31-11/2.

(235) Yuta FUKATSU, Luc R. VAN LOON, Amir SHAFIZADEH, Daniel GROLIMUND, Yasuhisa IKEDA, Takehiko TSUKAHARA, Celestite Precipitation-Induced Diffusion Behavior of 36Cl-, 22Na+, and HTO in Compacted Illite, Asian Nuclear Prospects 2016 (ANUP2016), 2016/10/24-27.

(236) Aileen Brandt, Takehiko TSUKAHARA, Highly-effective separation and detection of selenium ion using microfluidic device, Asian Nuclear Prospects 2016 (ANUP2016), 2016/10/24-27.

(237) Kyojiro Morikawa, Sachiko Ishihara and Takehiko Tsukahara, DEVELOPMENT OF TiO2 NANOPILLAR PATTERNED CHIP FOR NANO-DROPLETS FORMATION USING EXTENDED NANOCHANNELS, The 20th International Conference on Miniaturized Systems for Chemistry and Life Sciences (MicroTAS 2016), 2016/10/9-13.

(238) Kyojiro Morikawa, Yutaka Kazoe and Takehiko Tsukahara, DEVELOPMENT OF DIFFUSION OSMOTIC STREAMING CURRENT MEASUREMENT SYSTEM IN EXTENDED NANOSPACES FOR NON-PROBE ION MOBILITY MEASUREMENT, The 20th International Conference on Miniaturized Systems for Chemistry and Life Sciences (MicroTAS 2016), 2016/10/9-13.

(239) Kyojiro Morikawa and Takehiko Tsukahara, EVALUATION OF LIQUID PROPERTIES OF TRIVALENT ION SOLUTION FOR ION SEPARATION USING EXTENDED NANOFLUIDIC CHANNELS, The 20th International Conference on Miniaturized Systems for Chemistry and Life Sciences (MicroTAS 2016), 2016/10/9-13.

(240) Takehiko Tsukahara, Kaname Saga, Kyojiro Morikawa, Ki Chul Park, DEVELOPMENT OF STIMUTI-RESPONSIVE GEL PHOTONIC-CRYSTAL MICROCHIP FOR METAL ION SENSING, The 20th International Conference on Miniaturized Systems for Chemistry and Life Sciences (MicroTAS 2016), 2016/10/9-13.

BULLETIN OF THE
LABORATORY FOR ADVANCED NUCLEAR ENERGY

Vol.2 2017

平成30年2月　印刷

編集兼
発行者　東京工業大学科学技術創成
研究院先導原子力研究所
責任者　矢野豊彦
〒152-8550 東京都目黒区大岡山2丁目12-1
電話　03－5734－3052
FAX　03－5734－2959

印刷所　昭和情報プロセス㈱
東京都港区三田5－14－9

Printed by
SHOWA JOHO PROCESS
Minato-ku, Tokyo, Japan